DISSERTATION

HIGH-PRESSURE, LOW-TEMPERATURE OPTICAL AND X-RAY DIFFRACTION STUDIES OF SEMICONDUCTING AND INCOMMENSURATE MATERIALS

Submitted by

Jennifer L. Burris

Department of Physics

In partial fulfillment of the requirements

for the Degree of Doctor of Philosophy

Colorado State University

Fort Collins, Colorado

Fall 2003

COLORADO STATE UNIVERSITY

August 21, 2003

WE HEREBY RECOMMEND THE DISSERTATION UNDER OUR SUPERVISION BY JENNIFER L. BURRIS ENTITLED HIGH-PRESSURE, LOW-TEMPERATURE OPTICAL AND X-RAY DIFFRACTION STUDIES OF SEMICONDUCTING AND INCOMMENSURATE MATERIALS BE ACCEPTED AS FULFILLING IN PART REQUIREMENTS FOR THE DEGREE OF DOCTOR OF PHILOSOPHY.

Committee on Graduate Work

Advisor

Department Head

ABSTRACT OF DISSERTATION

HIGH-PRESSURE, LOW-TEMPERATURE OPTICAL AND X-RAY DIFFRACTION STUDIES OF SEMICONDUCTING AND INCOMMENSURATE MATERIALS

In order to investigate the effects of both high-pressure and low-temperature on materials, a new diamond anvil cell and gasket system has been developed which has increased stability over the previous design. In addition, a system has been designed to perform optical absorption measurements at high-pressure and low-temperature in a diamond anvil cell. Successful high-pressure, low-temperature Raman measurements have been performed on both Cs_2MoS_4 and $KTbP_2Se_6$ using the newly designed cell. Two pressure induced phase transitions have been observed at 77 K in Cs_2MoS_4 and a single pressure induced phase transition has been observed at 77 K in $KTbP_2Se_6$. High pressure, energy dispersive X-ray diffraction measurements of $(NH_4)_2\,ZnCl_4$ have also been performed at constant temperatures up to 150^oC. Values of the calulated adiabatic bulk modulus and experimentally determined isothermal bulk modulus for $(NH_4)_2\,ZnCl_4$ and other materials in the A_2BX_4 have been compiled and discussed.

Jennifer L. Burris
Physics Department
Colorado State University
Fort Collins, CO 80523
Fall 2003

Acknowledgments

I would like to acknowledge Dr. Hans D. Hochhiemer's supervision during my time at Colorado State University, for his hours spent reading my thesis, and for the many opportunities given to me to travel and work in different laboratories all over the world. I would also like to acknowledge my committee and other faculty in the Physics department for their input.

I would like to thank Caleb Blissett and Ana Kanevce for their support and humor in the lab over the last several years. And I would like to thank my family and friends for their belief in my abilities. In particular, thanks to Pam and Max who kept me smiling at work and to Hunter and Grace who kept me smiling at life.

Contents

Abstract iii

1 Introduction 1

2 High-Pressure Techniques 4

2.1 Gasketed Diamond Anvil Cell 5

2.1.1 Backing Plates 7

2.1.2 Gasket 10

2.2 Pressure Medium 13

2.2.1 Hydrostatic Conditions 13

2.2.2 Loading Techniques 15

2.3 High-Pressure Measurement 18

2.3.1 X-ray Pressure Gauges: NaCl and Au 19

2.3.2 Optical Pressure Gauge: Ruby 20

2.4 DAC Loading 24

3 Additions and Improvements to High Pressure Equipment 25

3.1 Early Contributions by the Author 25

3.1.1 Problems Encountered 25
3.1.2 Improvements in Diamond Alignment 26
3.1.3 Improvements in Pre-indentation and Chamber Creation 28
3.1.4 Moissanite Anvil Experiments 29
3.2 DAC Modification by the Author for Low Temperature Application 31
3.3 New Gasket Design 32
3.4 Future Direction 33

4 Interaction of Light with Matter **34**
4.1 Optical Measurements 34
4.2 Luminescence 36
4.2.1 Luminescence Theory 36
4.2.2 Experiment 39
4.3 Raman Scattering 40
4.3.1 Raman Scattering Theory 41
4.3.2 Experiment 51
4.4 Energy Dispersive X-ray Diffraction Measurements 51
4.4.1 X-ray Diffraction Theory 53
4.4.2 Experimental 56

5 Additions and Improvements to Optical System and X-ray Analysis **65**
5.1 Early Contributions by the Author 65
5.1.1 Problems Encountered 65
5.1.2 Improved Accuracy of X-ray Diffraction Measurements 67
5.1.3 Enhancements to Optical System 68

5.2 Additions by the Author to the Optical System 70
5.3 Calibration Improvements by the Author 71
5.4 Future Direction 74

6 High Pressure Survey of $(NH_4)_2ZnCl_4$ **77**
6.1 Incommensurate Materials 77
6.1.1 $(NH_4)_2ZnCl_4$ 78
6.2 Determination of the Isothermal Equation of State 81
6.2.1 Experimental Details 81
6.2.2 Lattice Constant Determination 81
6.2.3 Murnaghan Equation of State 84
6.2.4 Pressure Dependence of Density and Index of Refraction 86
6.3 Calculations of Adiabatic Bulk Moduli 86
6.3.1 Elastic Constant Data 86
6.3.2 Calculation Details 89
6.4 Discussion 90

7 High-Pressure Survey of Cs_2MoS_4 **92**
7.1 Transition Metal Chalcogenides 92
7.1.1 Cs_2MoS_4 94
7.2 Room Temperature Raman Measurements 103
7.3 Low Temperature Measurements 103
7.3.1 Experimental Details 106
7.3.2 Raman and Luminescence 106
7.4 Discussion and Future Work 106

8 High-Pressure Survey of $KTbP_2Se_6$ **110**

8.1 Rare-Earth Metal Chalcogenides 110

8.1.1 $KTbP_2Se_6$ 111

8.2 Room Temperature Raman Measurements 115

8.3 Low Temperature Measurements 115

8.3.1 Experimental Details 117

8.3.2 Raman 117

8.4 Discussion 117

9 Summary **119**

Appendices **121**

A Absorption System Calculations **121**

A.1 Single Lens 122

A.2 Two Lenses 124

A.3 Three Lenses 126

A.4 Experimental Setup 128

B Variable-Temperature Equipment **130**

B.1 High-Temperature Apparatus 130

B.2 Low-Temperature Apparatus 131

B.2.1 Cryostat 131

B.3 Future 134

Chapter 1

Introduction

High pressure is a powerful tool for materials research. It is used in combination with a variety of experimental techniques (optical, X-ray diffraction, transport, neutron, EPR, and NMR measurements) to study pressure induced changes. The majority of high-pressure work reported in this thesis consists of high-pressure optical and X-ray diffraction studies used to determine electronic and vibrational properties as well as structural changes of materials. The diamond anvil cell, used to generate the pressures of up to 15 GPa needed for research reported in this thesis, is a table top device in which a sample is placed between the flat parallel faces of two opposed diamonds.

There were several initial goals of this thesis. The material, $(NH_4)_2 ZnCl_4$, undergoes a series of structural phase transitions including a transition to an incommensurate phase. Extensive measurements of this material have been performed at ambient pressure, but no high pressure measurements of this material had been reported in the literature. Materials with incommensurate phases have a two-dimentional order parameter which leads to amplitudon and phason modes in the incommensurate phase. It has been suggested by theory [1] that the phason mode could be measured using Brillouin scattering. Such a study has

been undertaken as a thesis project in the high pressure group at Colorado State University in various A_2BX_4 materials with incommensurate phases. In order to analyze the high pressure Brillouin data, the equation of state for these materials is needed. Unfortunately, the equations of state for these materials were not available. Therefore, one of the goals of this thesis was to determine the equation of state of $(NH_4)_2 ZnCl_4$. Values for the isothermal bulk modulus, B_0, and its derivative, $B_0^{'}$ have been experimentally determined at 80^oC, 100^oC and 150^oC. Values of the calculated adiabatic bulk modulus are also presented.

Two other materials of interest were the materials Cs_2MoS_4 and $KTbP_2Se_6$. Both materials are of interest because of possible applications. Molybdinum sulfides are important in bioorganic chemistry and heterogeneous catalysis [2, 3] and rare earth cahlcogenides are an emerging class of new optical materials [4, 5, 6, 7]. Dicaesium tetrathimolybdate, Cs_2MoS_4, had been studied previously. High-pressure, room-temperature measurements by Lorenz et al. [8, 9] revealed a series of structural pressure induced phase transitions and a possible direct to indirect band crossing with increasing pressure. Potassium terbium selenodiphosphate, $KTbP_2Se_6$, had also been previously studied and a pressure induced electronic transition had been observed at room-temperature [10, 11, 12]. In order to better understand the possible direct to indirect band crossing in Cs_2MoS_4 and the observed electronic transition in $KTbP_2Se_6$, low-temperature, high-pressure measurements are necessary.

The primary goal of this thesis stems from the need to observe pressure induced effects in any materials at low temperatures. In order to achieve this goal, modifications to the high-pressure apparatus were designed and implemented, and a new absorption system was designed in order to perform optical absorption measurements at low temperatures, a system uncommon in the high-pressure field. Section 3.1 and Section 3.2 detail the new

modifications to the high-pressure apparatus. In particular, the previous equipment design was acceptable for high-pressure, ambient-temperature experiments; however, this design became unstable when used in conjunction with a cryostat. The enhancements to the high-pressure equipments allow for increased stabilization for low-temperature, high-pressure experiments. Section 5.2 and Appendix A detail the design of the low-temperature, high-pressure absorption system. Other specific improvements and additions to the laboratory are highlighted in Chapter 5. These include improvements to analysis procedures and improved calibration techniques and alignment procedures which increased accuracy and intensity readout of the optical system.

High-pressure and low-temperature Raman measurements have been successful for both both Cs_2MoS_4 and $KTbP_2Se_6$. Measurements reported in Chapter 7 indicate two phase transitions in Cs_2MoS_4 at 8.1 GPa and 9.1 GPa. High-pressure, low-temperature measurements reported in Chapter 8 indicate a single phase transition in $KTbP_2Se_6$ at 7.6 GPa.

Chapter 2

High-Pressure Techniques

Depending on the scientific field, various pressure units have been used. For technical applications pressure has units of atm (atmosphere) and psi (pound per square inch). In atmospheric science torr (mmHg) and mbar (dynes/cm^2) are common. Historically, the unit of choice in the field of high pressure research was the bar, kbar, or Mbar. Recently the SI unit of pressure, the Pascal (Pa=N/m^2), has been generally adapted and the GPa is used for scientific publications in all fields. This convention will be used throughout this thesis. Some reference pressures are listed in table 2.1.

The cornerstone of modern, experimental, high-pressure physics was developed by Percy Williams Bridgman of Harvard University in the early 20$^{\text{th}}$ century [13]. Pressure equals force per unit area. In order to increase the pressure either the force must increase or the unit area must decrease. Bridgman made use of the former concept with the invention of the piston-cylinder device. This was a large volume device ($> 1\text{mm}^3$) which could generate pressures up to 5 GPa. Bridgman developed another large volume system which utilized two opposed anvils of tungsten carbide. He introduced the principle of achieving a seal by using a gasket that was always under a higher pressure than the sample.

Pressure	[GPa]
Atmospheric Pressure at Sea Level	.0001
Tire Pressure	.0003
Freezing Point of Helium at 2K	.003
Pressure at Greatest Ocean Depth (Mariana Trench, 11km)	0.1
Average Max Pressure in Our Laboratory	15
Center of Earth	360
Highest Static Pressure Reached in a Diamond Anvil Cell	550
Center of Sun	$\sim 10^7$
Core of Neutron Star	$\sim 10^{29}$

Table 2.1: Some Reference Pressures.
1GPa=10kbar $\approx$ 10,000atm

In 1958 high-pressure research was revolutionized by the development of the diamond anvil cell. Invented concurrently at the University of Chicago by Jamieson, Lawson and Nachtrieb [14] and at the National Bureau of Standards in Washington, D.C. by Weir, Lippincott, Van Valkenburg, Jr., and Bunting [15], the researchers employed the diamond anvil cell to reduce sample area thus increasing pressure.

2.1 Gasketed Diamond Anvil Cell

The diamond anvil cell (DAC) has significant advantages over previous technologies. The DAC uses a sample volume less than .005 mm^3. This is significantly smaller than the more than 1 mm^3 sample volume in a large volume cell. Because of this small volume, the force required to create large pressures is less than 1% of the force required for the same pressures in a large volume cell. The small forces used in a diamond anvil cell ensure complete safety of the researcher in the event of experimental failure. A relatively small force of about 4 kN, equivalent to a 400 kg weight, is enough to create pressures in excess of 500 GPa

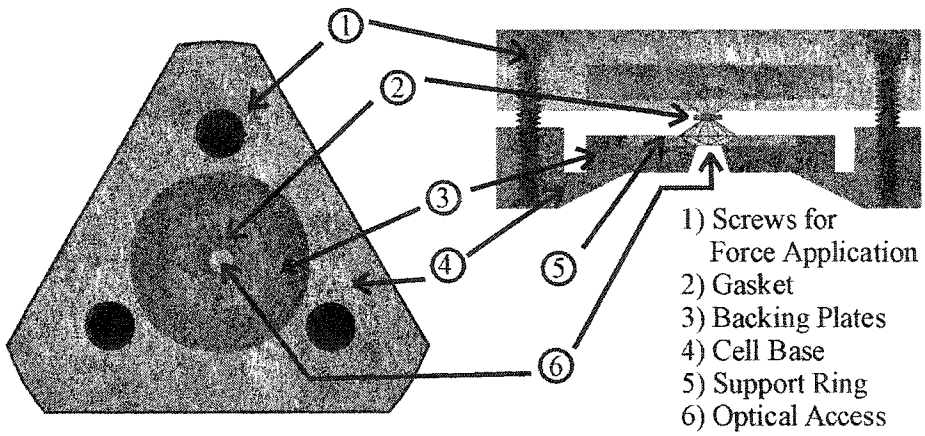

Figure 2.1: Our Merrill-Bassett type DAC.

[16]. Another advantage of the DAC is the exceptional yield strength and hardness of diamond. These properties of diamond allow for great forces to be applied before failure. Diamonds are also transparent to a wide frequency range of electromagnetic radiation. The development of this technology thus allowed, for the first time, visual observation of pressure effects and access to new experimental techniques, notably X-ray diffraction and optical spectroscopies.

Any anvil pressure system must have a method of forcing the anvils together, as well as sufficient support for and alignment of the anvils themselves. Another important aspect concerns the ability to access the sample for measurements. It is quite clear from the DAC design that experiments such as optical and X-ray diffraction measurements, which do not involve a direct contact with the sample, are favored over measurements which require contact with the sample. These types of contact measurements include electrical [17], thermopower [18], and specific heat measurements [19].

The original DACs were hand-held devices in which a spring-loaded lever arm assembly provided the necessary force. Similar devices are still in use today. We use a Merrill-

Bassett type DAC cell shown schematically in Figure 2.1. Designed in 1973 [20], this cell is one of the smallest of the diamond anvil cells and is ideal for X-ray diffraction and low-temperature studies.

The main body of the Merrill-Bassett type DAC consists of two triangular plates that apply the force necessary to generate the pressure. These two plates are forced together by hand tightening the three screws at the corners of the DAC, as displayed in Figure 2.1. As the anvils come closer together, they press on the gasket creating pressure in the pressure chamber as described in Section 2.1.2. Support for the anvils, their alignment, and optical access to the sample are provided by metal backing plates.

2.1.1 Backing Plates

The backing plates are designed to balance the following two competing requirements: sufficient support at the base of the diamond is needed so that force can be transmitted to the diamond tip; and an optical window to allow for access of electromagnetic radiation needed for probing the sample. The entrance angle and window diameter are chosen based upon experimental requirements and specifications of the material used to machine the backing plate. For example, a typical diamond used in our laboratory has a 0.3 mm diamond tip and the back flat of the diamond, supported by the backing plate, has a diameter of 2.5 mm. With an optical window of 1 mm and a pressure of 20 GPa at the tip of the diamond, about .5 GPa is transmitted to the backing plate.

2.1.1.1 Diamond Mounting

Properly securing the diamonds into the backing plate is essential for equipment stability. One way to attach the diamonds is by using an epoxy resin to glue the diamonds in place.

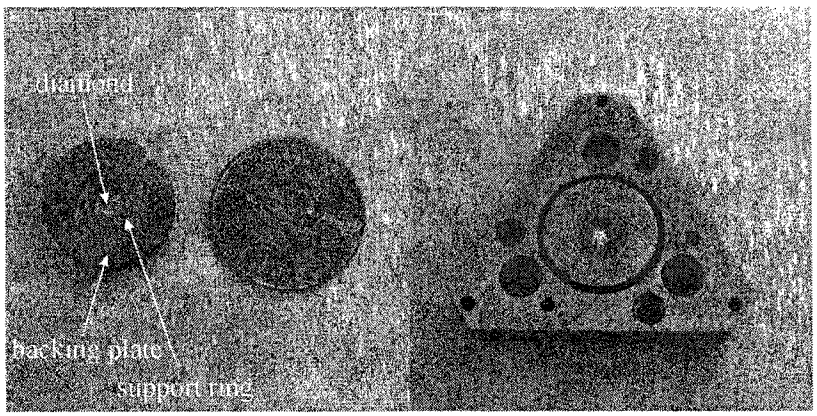

Figure 2.2: Diamond mounted into backing plate and then into DAC.

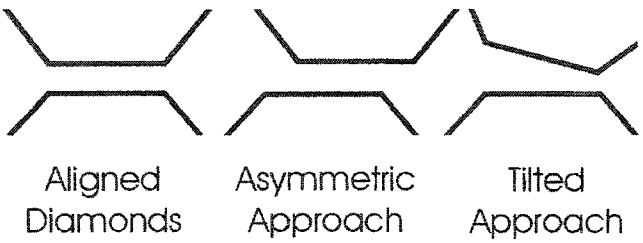

Figure 2.3: Unaligned and non-parallel diamond anvils.

Another way is to press-fit a metal ring between the diamonds and the backing plate. The former method is much simpler but not appropriate for variable temperatures. That method also requires re-attachment after only a few pressure runs. The latter method, though initially much more time consuming, provides, in principle, for the diamonds to remain in place indefinitely. This is the method utilized in our laboratory. Once the diamonds have been secured into the backing plates, the entire assembly is placed into the main triangular body of the diamond anvil cell.

2.1.1.2 Alignment

Before pressure can be generated it is essential that the opposing diamonds are both aligned with, and parallel to, each other. If this is not the case serious problems can occur as the pressure is increased. This can include gasket or diamond failure. The alignment process can be tedious and time consuming, but it is crucial for experimental success. The diamonds can shatter if they approach one another asymmetrically during a pressure run. Although diamonds are very strong under pure compression, they shatter under small shear stresses due to their brittle nature. Diamond also has both a fairly high concentration of microscopic flaws and a well-defined (111) cleavage plane. To ensure that the diamonds do not break, it is therefore necessary that the diamonds are aligned within microns.

For pressure above about 20 GPa, the opposed diamond flats must be parallel to each other within a couple of fringes of visible light. This procedure requires moving the diamonds to within nanometers of one another. In doing so, the chance that the diamonds touch each other and cause damage is increased. For the pressure range reported on in this thesis the need to have the diamonds exactly parallel to each other is not as crucial. It should be sufficient that the DAC itself is machined well and stable and that the base and tip of the diamond are parallel [21].

In addition to the requirement that the diamonds be parallel, they must also be aligned to one another as seen in Figure 2.3. In order to ensure proper alignment, the diamonds need to be within about 10 microns of one another and one diamond must be moved slightly until it appears even with the other.

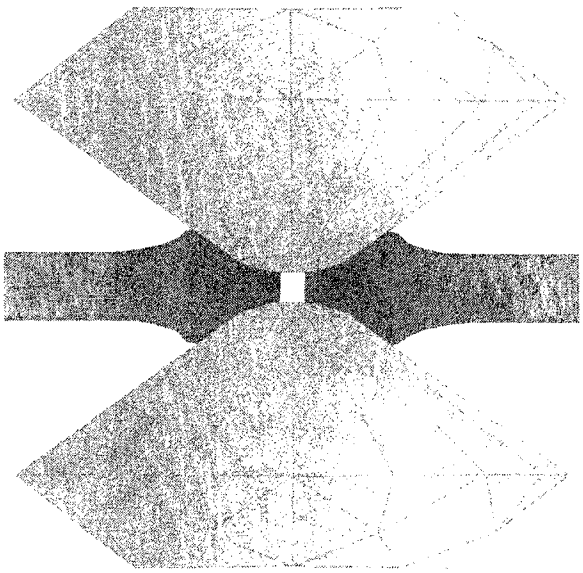

Figure 2.4: Gasketed, opposed diamond anvils.

2.1.2 Gasket

Early high pressure experiments were carried out by squeezing powdered samples between two diamonds with nothing surrounding the samples. Therefore, it was not possible to contain the samples within the area of the anvils. As a result, the samples would be squeezed out on the sides, possibly causing experimental failure. Even in successful experiments, a very large pressure gradient existed throughout the sample, from ambient pressure near the edges of the diamonds to a maximum pressure at the center. This approximate parabolic distribution of pressure created large shear stresses [22]. In order to overcome this disadvantage a technique was developed by A. Van Valkenburg [23] to surround the sample with a metal gasket as shown in Figure 2.4. The purpose of the gasket is two-fold: to create a pressure chamber that contains the sample and to provide lateral support to the diamond anvils.

The choice of gasket material used depends upon many factors. These include the size

of the diamond anvils, the desired final pressure, the machining quality of the diamond anvil apparatus, the type of tool used to drill the pressure chamber in the gasket, and the price of the gasket material. Materials such as brass and copper are used commonly for diamond anvils with 1 mm size tips. These materials are relatively inexpensive and easy to drill. With smaller tip diamonds, a harder material such as Inconel is necessary, but such materials are more expensive and more difficult to machine. The selected material must always be able to deform sufficiently to seal the pressure chamber. To ensure pressure chamber stability, optimal thickness and hole diameter must be used. The requirements depend upon the maximum desired pressure [24].

2.1.2.1 Pre-Indentation

Typically, the gasket has an initial thickness of 100-250 μ and is pre-indented. This indentation depth is determined by placing a pressure sensor directly on the gasket with no pressure chamber and indenting until a pressure of 50% the desired maximum pressure is reached. This is the depth to which the pre-indentation should occur. A harder material indicates a smaller indentation depth for the same pressure.

This pre-indentation process work-hardens the gasket material and creates more lateral support for the diamonds. In order to pre-indent the gasket, a systematic decrease of the distance between diamonds is required. This is achieved by small incremental turns of each of the three screws in steps of 5-10 μ until the desired pre-indentation depth is reached. It is important that the gasket is pre-indented to at least 50% of the intended final pressure. As the intended maximum pressures increases, a higher pre-indentation pressure is necessary. If the diamonds are properly aligned, a symmetrical indentation will be observed after pre-indentation by visual inspection of both sides of the gasket.

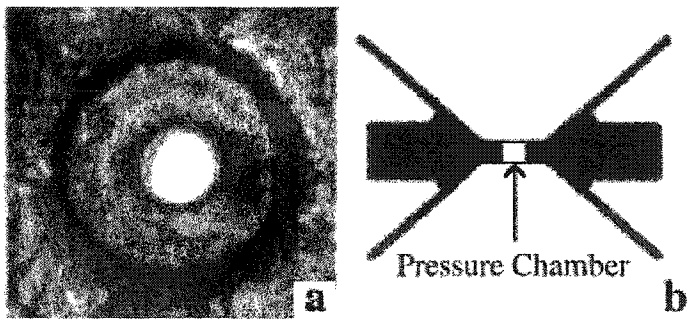

Figure 2.5: (a) Pre-indentation with centered hole; (b) Side view of pressure chamber.

2.1.2.2 Creation of Pressure Chamber

After the above procedure, the pressure chamber is created. A hole is machined into the gasket at the center of the diamond indentation. The hole diameter is $\leq 1/3$ the diameter of the diamond tip. The higher the intended maximum pressure, the smaller the hole diameter. The hole should be centered in the indentation to within 5-10% of its diameter as shown in Figure 2.5 (a). This hole, along with the two diamond anvils, creates the pressure chamber as seen in Figure 2.5 (b). As mentioned in Section 2.1.1.2, the alignment of the two anvils is crucial for the success of the experiment. The final check on the alignment is to affirm the location of the hole on both sides of the gasket. If the diamonds are aligned the hole should be located in the same place on both sides.

2.1.2.3 Initial Conditioning

When the diamonds are first mounted into the backing plate, described in Section 2.1.1.1, a rather lengthy process is undertaken to condition the cell. This is an exacting process of gradually indenting the gasket, aligning the diamonds, and repeating the entire procedure several times. Repetition of this process with successively higher force is necessary until the desired final indentation depth is reached. Initially the gasket is indented by only about

10-20% of its initial thickness. The alignment is again adjusted and the gasket is again indented to the same depth until the diamonds settle and the alignment is stable. During the first few pressure runs, the cell is taken to only about 5 or 6 GPa. If, after the first pressure run, the alignment is still accurate, then the cell is taken to about 10 GPa. If the diamonds are misaligned after the first pressure run, the cell must be reconditioned. This process is repeated until the desired maximum pressure is reached with no drastic realignment. At this point the cell is conditioned and should function optimally.

2.2 Pressure Medium

As force is applied to the DAC, the diamonds move closer to one another, creating pressure on the gasket and causing gasket deformation. As the gasket deforms by getting thinner, the walls of the pressure chamber are forced toward each other. In the simple case of an empty pressure chamber the hole will get smaller and smaller with increasing pressure and eventually disappear altogether as the gasket material flows into the empty space. This occurs at much less than one gigapascal depending slightly on the hardness of the gasket material. If only the sample is placed in the pressure chamber, a large pressure gradient can occur from one side of the sample to the center, similar to the case of no gasket mentioned in the precious section. It is necessary to eliminate these non-hydrostatic conditions.

2.2.1 Hydrostatic Conditions

Hydrostatic conditions exist when uniform pressure is applied to all sample surfaces and no shear stress is present. For most experiments, hydrostatic conditions can best be obtained by introducing into the pressure chamber a pressure-transmitting medium. This pressure

medium surrounds the sample and allows a homogeneous pressure distribution to all sample surfaces. Gases and liquids tend to provide the best hydrostatic conditions; however, both turn to solids at sufficiently high pressure. Therefore, one has to choose the pressure medium carefully to ensure hydrostatic conditions in the pressure and temperature range of the measurement.

In general the noble gases produce the best hydrostatic conditions when solidified, [25] especially at low temperatures. Due to high compressibility gases must be loaded into the hole as liquids or at densities above the critical point. This avoids massive volume decrease of the pressure chamber with increasing pressure. It requires, however, the loading of the DAC in either cryogenic or pressurized environments. For example, solid helium provides a nearly hydrostatic environment[1] to > 60 GPa, but is very difficult to load into the pressure chamber. The entire diamond anvil cell must be placed in a cryostat which is evacuated to remove moisture. In order to ensure that the helium completely fills the pressure chamber, the superfluid helium transition must be reached (~2.2 K).

2.2.1.1 Ambient Temperatures

Pressure transmitting media that are liquid at room temperature can be quickly and directly loaded into the pressure chamber at ambient conditions. Whenever appropriate, therefore, room temperature liquids are used as the pressure transmitting medium. For the range of pressure reported on in this thesis, up to ~15 GPa, the most common medium used at room temperature is a 4:1 methanol:ethanol (CH_3OH: C_2H_5OH) mixture. This mixture freezes at 10.4 GPa at room temperature [27], but is nearly hydrostatic to ~20 GPa. For samples that might chemically react with the alcohol mixture, a 1:1 pentane:isopentane mixture is

[1]Defined as the standard deviation of the pressure measured at five points within the sample chamber being less than 0.6% of the nominal pressure [26].

less reactive, but only hydrostatic to ~7 GPa.

2.2.1.2 Low Temperatures

At liquid nitrogen and liquid helium temperatures the 4:1 methanol:ethanol mixture is no longer appropriate because it freezes at ambient pressure. When this occurs, the solid that forms causes the pressure to be of a nonhydrostatic nature. Again, helium is the best choice at low temperatures. However, due to the difficult loading process another noble gas is commonly used. One of those choices is argon. Solid argon provides a nearly hydrostatic environment at the temperatures and pressures necessary for this thesis.

2.2.2 Loading Techniques

The pressure medium must be loaded into the pressure chamber to ensure hydrostatic conditions. Depending on the desired temperature range, either argon or a 4:1 methanol:ethanol mixture is used. The loading techniques are very different for the two pressure transmitting media.

The 4:1 methanol:ethanol mixture is a liquid at ambient conditions and can be loaded with a syringe into the pressure chamber. This technique is the more difficult to master. The volume of the pressure chamber is less than .005 mm^3, much smaller than a drop of the pressure medium (see Figure 2.6). Care must be taken during the loading process to avoid flushing the sample and pressure sensor from the hole. It is also of crucial importance that the entire DAC be clamped shut as quickly as possible in order to avoid media evaporation.

Argon is a gas at ambient conditions and must be condensed into the pressure chamber. After loading the cell with the sample and the pressure sensor, the cell must be clamped to a position where the diamonds are just touching the gasket. Care must be taken not to

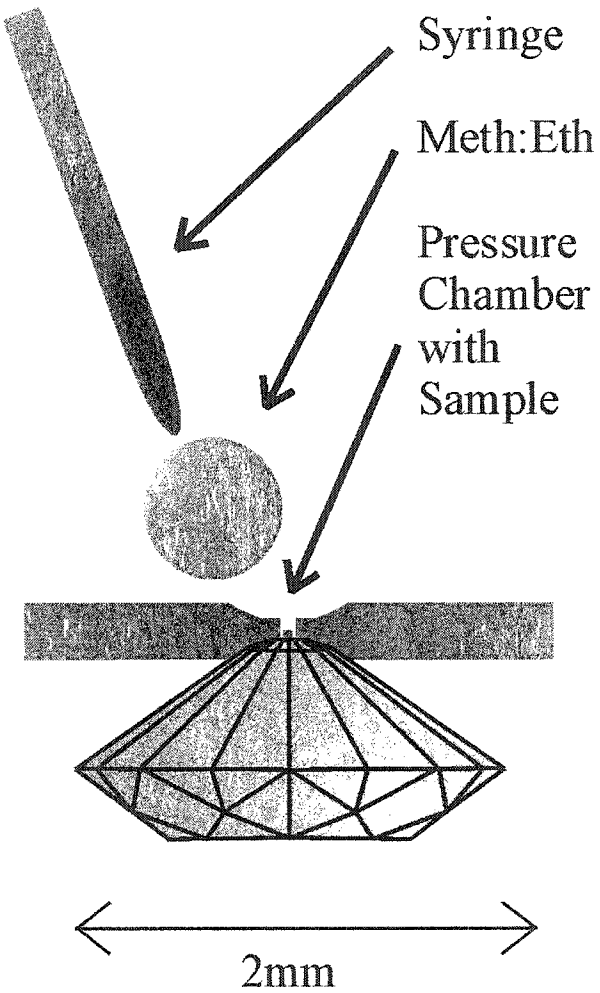

Figure 2.6: Loading liquid pressure medium [21].

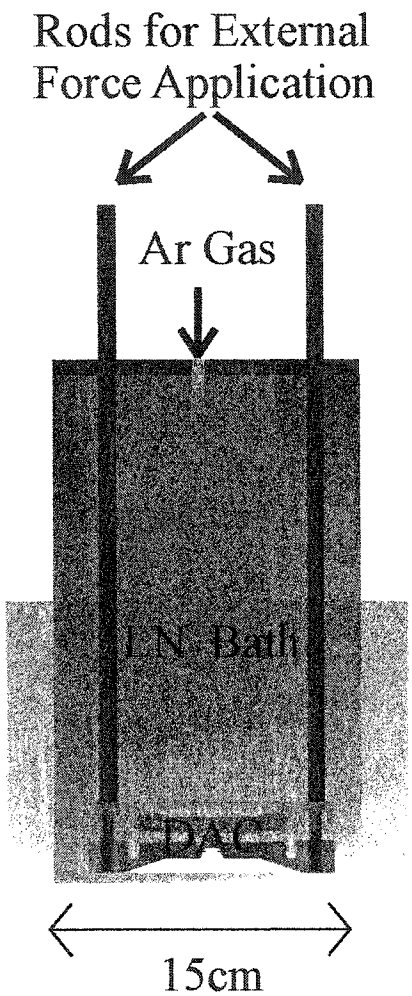

Figure 2.7: Argon loading system.

put any pressure on the gasket or the pressure chamber will close. Following this step, the entire cell is placed in a cryogenic environment and flooded with argon gas. Next, the cell is opened slightly to allow argon gas to flow into the pressure chamber (see Figure 2.7). The system is then cooled in a liquid nitrogen bath. At ambient pressure the argon will liquefy at 84 K and solidify at 81 K. Once solid argon is present, the cell is clamped shut and returned to ambient conditions.

Although it is much more difficult to master the process of loading by syringe, the 4:1 methanol:ethanol mixture is preferable and is more cost effective than argon since only a single drop of the mixture is used in the process. The loading process requires less time; an experienced person can load the mixture in about 30 seconds whereas it takes about one hour to load the cell with argon. Still, at low temperatures, argon is a better hydrostatic pressure medium.

After loading the chamber and sealing the cell pressure must be applied before it is possible to determine that the hole is filled with pressure medium. If there is no medium, the hole will close up when pressure is applied. If there is too little of the medium, an air bubble will become trapped inside. That bubble will disappear under pressure, but the hole will be significantly smaller and most likely the entire gasket indentation and loading process must be repeated.

2.3 High-Pressure Measurement

Both force and area can be measured with high accuracy. However, experimental errors do not allow pressure to be determined to the same accuracy [28]. This is due to systematic errors such as force losses between the point of measurement and the sample, as well as error in determining the sample area due to gasket deformation. These errors do not allow

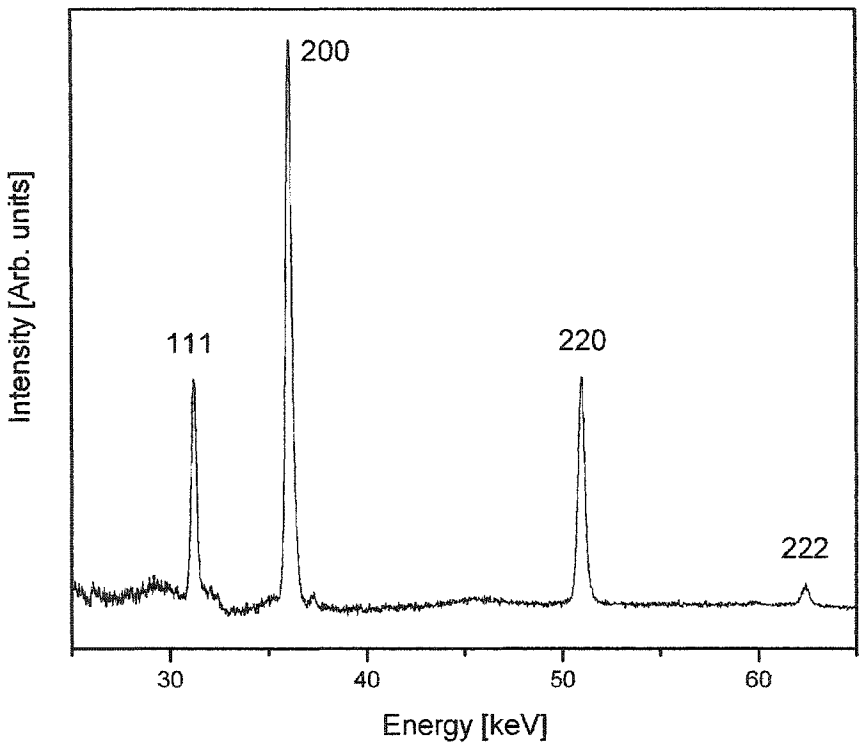

Figure 2.8: NaCl EDXD graph with specific reflections labeled.

accurate pressure determination by calculating force per unit area. Other pressure gauges must therefore be used.

2.3.1 X-ray Pressure Gauges: NaCl and Au

A primary pressure gauge is any material for which the calculated equation of state agrees very well with experimental data obtained from static and dynamic (shock wave) high pressure experiments. Two such primary pressure gauges are sodium chloride and gold. Sodium Chloride is the most widely used equation of state calibrant. Introduced by Decker

[29, 30], it is still used for large volume cells and for X-ray diffraction experiments using diamond anvil cells. Gold is also a widely used primary calibrant [31]. The choice of pressure calibrant depends on the position of the calibration peaks with respect to the sample peaks and also on any reaction that might take place between the sample and calibrant.

For diffraction measurements NaCl has been used as the pressure sensor. Powder X-ray diffraction (see Chapter 4 for details) requires the sample to be ground into a very fine, concentrated powder. For this reason it difficult to acquire data when a liquid pressure medium is used. Instead the NaCl acts as both the pressure sensor and pressure medium. The sample and NaCl are crushed together into a powder, until individual crystal sizes are less than 1 μm, then packed into the diamond anvil cell.

Because of this technique each sample spectrum includes NaCl reflections as well as sample reflections. The energy of the both the (200) and (220) reflections of NaCl are measured. The d-spacings of the NaCl crystal lattice can then be calculated as detailed in Chapter 4. Knowing that NaCl is a cubic lattice and using the planar spacing equation (Equation 4.19, Chapter 4) the lattice constant can be calculated. The pressure can then be determined since the X-ray diffraction peaks of NaCl have been well calibrated to pressure by D.L. Decker [29, 30]. An energy dispersive X-ray diffraction graph of NaCl is shown in Figure 2.8 with the main reflections labeled.

2.3.2 Optical Pressure Gauge: Ruby

Since diamond is transparent in a wide wavelength range of electromagnetic radiation, spectroscopic wavelength or frequency changes of a material can be calibrated with increasing pressure. The fluorescence spectrum of ruby, Al_2O_3:Cr^{3+}(about 0.3% Chromium), is pressure dependent as shown in Figure 2.9. Unlike NaCl and Au, the use of ruby as a

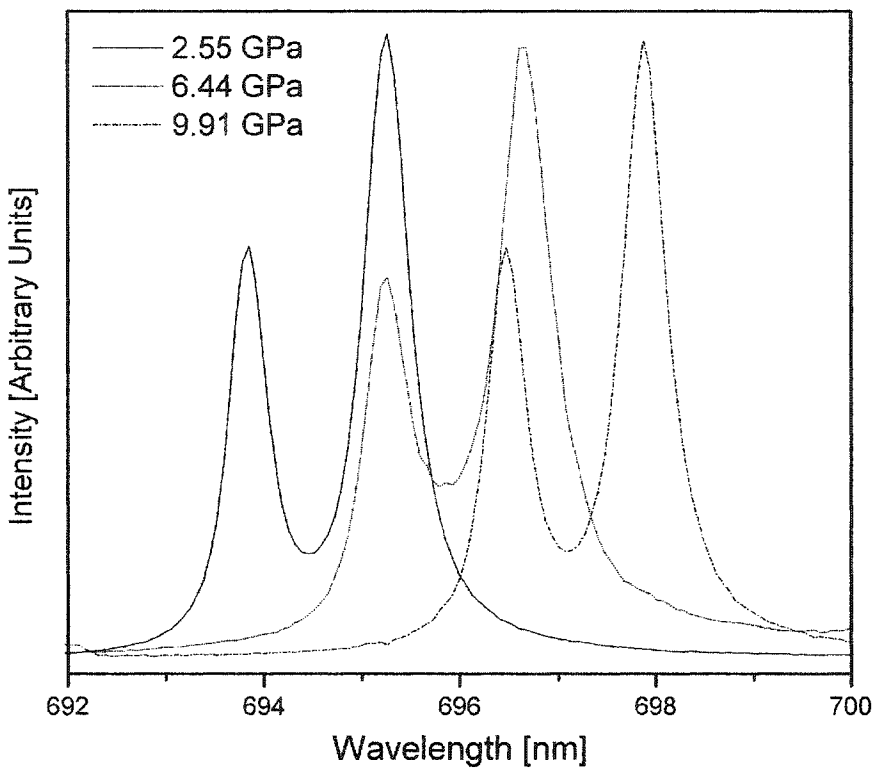

Figure 2.9: Ruby fluorescence shift with pressure.

high-pressure calibrant requires no information about its equation of state. First used as a secondary high-pressure gauge (any material with a property that changes systematically with pressure) at the National Bureau of Standards [32, 33], the group showed that the ruby lines shifted linearly with pressure up to 19.5 GPa by calibrating the shift against the NaCl pressure gauge. They proposed $P = 2.746\Delta\lambda\,\mathrm{GPa/\AA}$. It was also observed that the ruby lines broaden as the pressure medium becomes less hydrostatic. As experiments increased the calibration range to higher pressures, a slight deviation from linearity was observed [34]. The following relationship was proposed

$$P = 380.8\left(\left[v_0\left(T\right)/v_P\left(T\right)\right]^5 - 1\right) \tag{2.1}$$

where P is the pressure in GPa, $v_P\left(T\right)$ is the frequency of the ruby R_1 line at pressure P and temperature T, and $v_0\left(T\right)$ is the corresponding frequency at the same temperature and ambient pressure. The zero-pressure frequency is determined by [35]

$$v_0\left(T\right) = 14423\,\mathrm{cm^{-1}} + 4.49\times10^{-2}T\,\mathrm{cm^{-1}/K} \tag{2.2}$$

$$-4.81\times10^{-4}T^2\,\mathrm{cm^{-1}/K^2} + 3.71\times10^{-7}T^3\,\mathrm{cm^{-1}/K^3}$$

Other fluorescent pressure sensors have been proposed such as Sm:SrFCl [36], Eu:YAG ($Y_3Al_5O_{12}$)[37], and Sm:YAG [38], but ruby remains the most widely used optical pressure sensor due to its long, well documented history. Pressure calibrants are chosen by considering the fluorescence peak positions compared to the sample peak position and desired intensities at different temperatures.

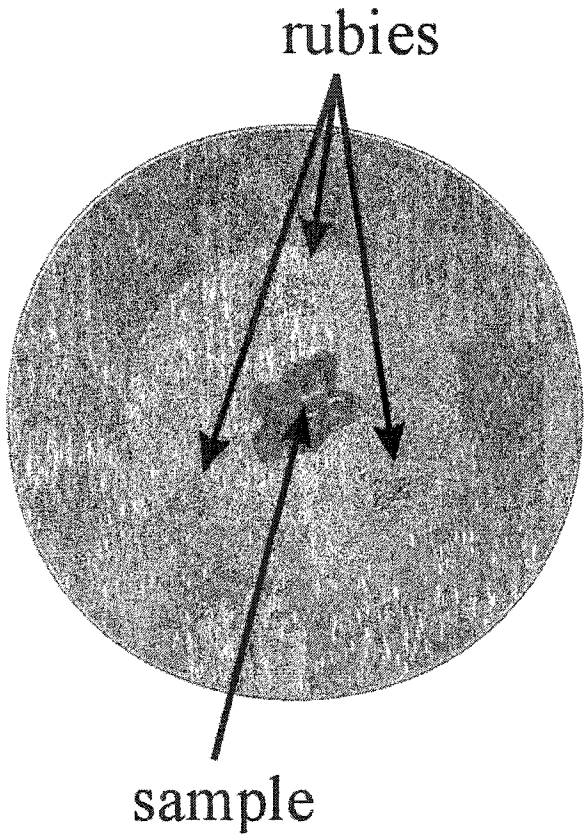

Figure 2.10: Diamond anvil cell loaded with sample and ruby pressure sensors.

2.4 DAC Loading

After alignment of the cell and preparation of the pressure chamber, the sample, pressure sensor and pressure-transmitting medium must be loaded into the pressure chamber. Since the dimensions are so small, all work must be done using a microscope. For single crystal experiments, the ideally loaded cell has three pressure sensors near three separate edges of the hole and in the middle the sample. The sample should be no larger than about 2/3 the diameter of the hole with a typical size of 0.05 mm. Neither the sample nor the pressure sensors should be touching the edge of the hole. Ideally, the thickness of the sample and the sensor should be such that they never touch the diamond culets.

For some experimental techniques, notably powder X-ray diffraction, the same material is used as the pressure sensor and the pressure transmitting medium as mentioned in Section 2.3.1. In this situation, the sample and sensor/medium must be mixed together and ground into a very fine powder. Care must be taken to pack in to the chamber as much of the mixture as possible in order to minimize the amount of hole deformation that will occur under pressure.

Chapter 3

Additions and Improvements to High Pressure Equipment

3.1 Early Contributions by the Author

During the first three years of experiments, stability issues occurred with the diamond anvil cells. All experiments reported on in this thesis required pressures in excess of 12 GPa. During the original set of experiments, pressures in excess of 6 GPa were unusual at low temperatures. The general failure of these experiments, and the specific problems encountered led to drastic improvements in laboratory procedures and experimental apparatus.

3.1.1 Problems Encountered

The main problem during these initial experiments was migration of the pressure chamber at low temperatures. As the pressure was increased, the chamber would drift in the gasket, eventually reaching the edge of the diamonds and causing premature pressure loss.

At ambient temperatures, it is easy to control the force which is applied to different edges of the DAC and this migration does not occur. For low temperature experiments the controlling of this force is impossible because the DAC is placed inside of a cryostat. Details of this cryostat are discussed in Appendix B. Uneven force application inevitably occurs at low temperatures and, in early experiments, consistent hole migration under 6 GPa was observed. It was necessary, therefore, to improve the stability of the DAC so that uneven application of force would not result in the drifting of the pressure chamber.

The following subsections summarize improvements that were added one by one. With each modification came added stability to the DAC and an increase in the maximum pressure obtained. As discussed in Section 3.2, the final improvements were made in 2002 with new designs of both the diamond anvil cell and gasket.

3.1.2 Improvements in Diamond Alignment

As detailed in Section 2.1.1.2, by increasing the accuracy of diamond alignment, the odds of experimental success dramatically improve. The procedure for diamond alignment once consisted of placing a clear piece of plastic in between the two diamonds. The diamonds were then carefully brought toward each other until they first contacted the plastic. The two sides of the DAC were not screwed together for fear of creating too much force, breaching the plastic, and cracking the diamonds as they came into contact. This procedure allowed for the diamonds to be very close to each other. Unfortunately, during alignment the lateral motion of the entire system was highly unstable since the two halves of the DAC were not connected (see Figure 3.1). Because the lateral motion was not stable during the alignment process, the alignment itself was inaccurate.

The initial solution to this problem consisted of placing a slightly malleable material

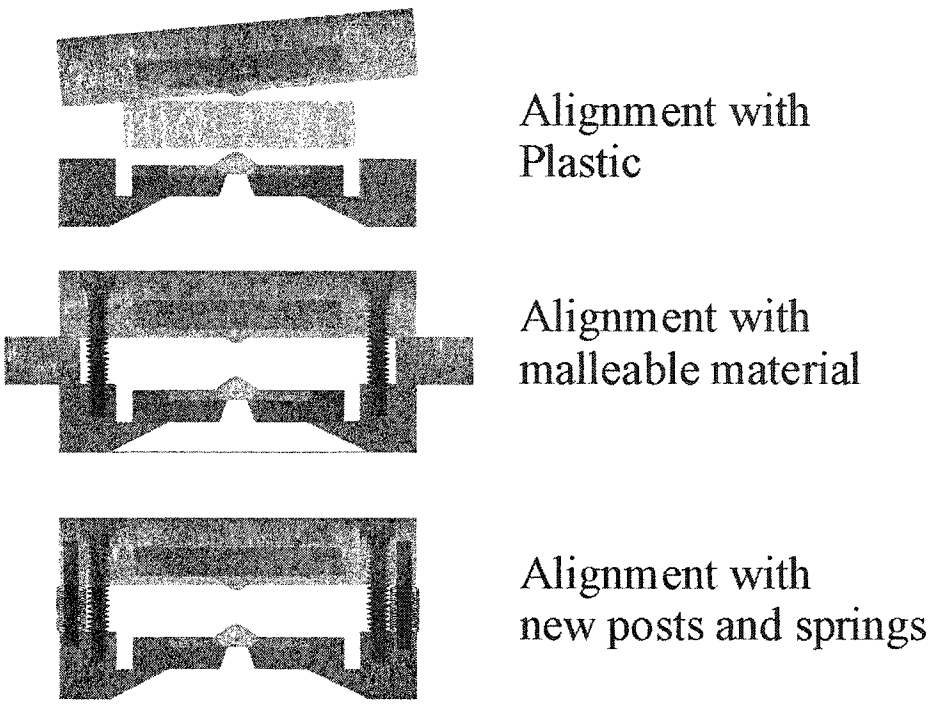

Figure 3.1: Alignment Procedures.

between the two halves of the DAC at each of the three sides of the device. This allowed the two halves of the DAC to be attached by the three force providing screws without fear of the diamonds touching. Unlike the previous procedure, this one maintained lateral stability during the alignment process while still allowing the diamonds to be brought close together. An even more convenient solution was implemented with the improved DAC design discussed in Section 3.2 which allows for springs to be placed at the three corners of the DAC. These springs allow for the diamonds to be advanced toward each other in a more controlled manner, while maintaining all of the benefits associated with the malleable material.

3.1.3 Improvements in Pre-indentation and Chamber Creation

The initial laboratory protocol was to pre-indent the gasket to 120 μm. By running a battery of experiments to determine the pressure at different indentation depths, better mapping occurred of the correct indentation depth needed to achieve the maximum desired pressure. The 120 μm indentation corresponded to a pre-indentation pressure of only about 3.5 GPa for the inconel gasket. The results of these experiments indicated that a pre-indentation of 60-80 μm, giving a pre-indentation pressure of about 8 GPa, was appropriate for the reported experiments.

Prior to 2001, the pressure chamber was created using a micro drill. This is a drill press miniaturized to employ bits less than .5 mm. There were several problems associated with this process. First, as with any mechanical drilling process, the hole formed by the micro drill bit is not completely smooth. Some of the displaced material created a ridge around the edge of the pressure chamber. This material had to be cleaned off. Inevitably, an asymmetrical pressure chamber resulted. This asymmetry caused uneven forces to be exerted

on different sides of the pressure chamber resulting in hole migration. The second main problem encountered with the micro drill was the limitation of hole size with decreasing diameter. As the size of the hole decreases, the chance that the hole will migrate all the way to the edge of the gasket decreases. Unfortunately, at some small bit size, the bits themselves are not strong enough to withstand the drilling process.

In 2001 the laboratory purchased a micro electronic discharge machine (EDM). This operates by setting up a voltage difference between the workpiece and the EDM tool. When the two pieces are brought within close proximity to one another, a spark occurs across the gap. The discharge is then terminated. This is repeated on the order of microseconds. Each discharge erodes a part of the workpiece.

Because of the way the EDM creates holes, the problem of extra material around the pressure chamber no longer exists. The symmetry of the pressure chamber now depends only on the symmetry of the EDM tip. The EDM is most useful for drilling a pressure chamber as small as needed to limit hole migration. Since any copper magnet wire can be used as the EDM tip, the size of the hole is limited not to tip's strength, but to the tip diameter. EDM tips as small as 10 μm can be used, and the size of the pressure chamber is limited only by the skill of the experimentalist in loading the sample, sensor and pressure medium into the chamber.

3.1.4 Moissanite Anvil Experiments

Nearly six months were spent attempting to use moissanite anvils instead of diamond anvils. Hexagonal silicon carbide (SiC), or moissanite, is a synthetic gem stone shown to be an effective high-pressure anvil to 52 GPa [39]. Moissanite is of interest for several reasons. A typical optical quality diamond anvil costs around $2,500, whereas a moissanite

anvil of the same size costs about $200. As well as having many of the optical properties of diamond, moissanite can be used to study materials which have peaks in the same spectral range as diamond. Moissanite can also be used to study diamond itself at high pressures.

As discussed in Section 2.1.1.2 diamonds are brittle, shattering under shear stress. Small diamonds are used in high pressure experiments due to cost and because the force required to shatter brittle particles increases as the particles get smaller[21]. This is due to the increase in probability that a flaw will exist in larger particles. A typical diamond anvil is less than half a carat. Moissanite anvils are less brittle and can be manufactured to sizes equivalent to a 300 carat diamond. With anvils this size, large volume samples can be taken to much higher pressures than are now possible. Unlike diamond, moissanite can be manufactured with no facets. The rotational symmetry of this simple cone shape minimizes radial stresses.

We did not have the same success with moissanite that Xu and Mao have reported [39]. It is concluded that this is due to the instability of the DAC used at the time of the moissanite experiments. After destroying six separate moissanite anvils in various experiments, the effort was ended. The moissanite anvils did seem to consistently perform well below about 4.5 GPa. It is suggested that moissanite anvils can be a good substitute for the 1mm tip diamond anvils used at CSU for experiment below 5 GPa. Also, with the DAC modifications discussed in the next section, another attempt to use moissanite may prove fruitful.

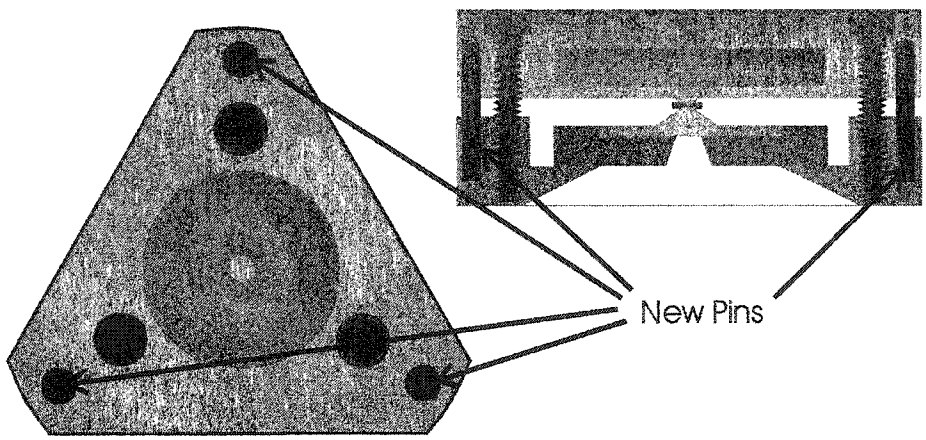

Figure 3.2: New DAC Design.

3.2 DAC Modification by the Author for Low Temperature Application

Due to the uneven force application inevitable for low temperature experiments (see Section 3.1.1), the main goal was to create a DAC design which had improved stability over the previous apparatus. When placing the two halves of the old DAC together, it was easy to cause torque on the system, rotating the halves in opposite directions, and bringing the diamonds out of alignment. As discussed in Section 2.1.1.2 displacement no greater than a few microns can cause major problems. The second problem with the old diamond anvil cell was that when increasing the force with one of the three screws, the two halves of the DAC would not remain parallel to each other. This created additional alignment problems.

Improved stability was created by adding three 1 mm posts to each of the three corners of the diamond anvil cell. The observed rotation of the old diamond anvil cells is non-existent with the new design. This lack of rotation also increases the ability for the two halves of the DAC to remain more parallel. This design has proved highly functional and

was used to take all data reported in Chapters 7 and 8.

3.3 New Gasket Design

Inconel was used as the gasket material for all of the previously discussed experiments. After much research of this problem [40], the determination was to employ a harder gasket material. Rhenium was a good candidate. Though it is harder than Inconel, it is also much more expensive. The original gasket design has an approximate area of 2.5 cm^2. This is a cost of about $2/gasket. In order to have a comparable price, the rhenium gaskets would have to be 8x smaller than the inconel gaskets.

Other laboratories which use rhenium have a totally different gasket design than in this laboratory. Their design accommodates the smaller size necessary to use rhenium; however, after pre-indentation it is very difficult to place the gasket back in its original position. The gasket utilized in this laboratory is designed such that the original position is easily reproducible. Unfortunately, the gaskets are too large to use rhenium.

The goal became to design a gasket that would use less rhenium, but still allow for accurate repositioning of the gasket onto the diamonds. With the insight of Caleb Blissett, a graduate student in the high pressure laboratory at Colorado State University, such a product was designed. By taking a larger gasket, one made of less expensive material, and punching out a small circle, one could then press into that hole in a slightly larger circle of rhenium. In this manner, the larger size gasket is functional and only a small amount of rhenium is necessary.

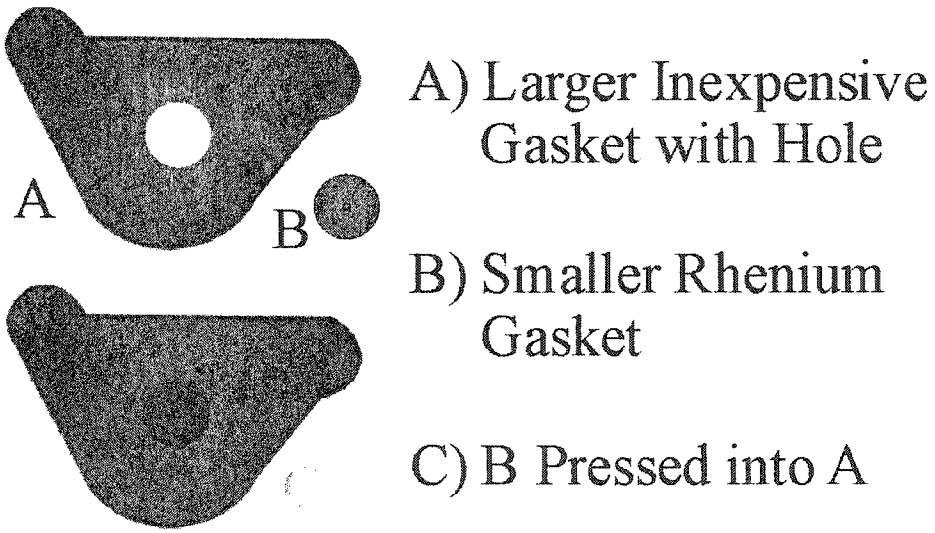

Figure 3.3: New Gasket Design.

3.4 Future Direction

Although many changes have been implemented over the past several years, other enhancements to the high-pressure equipment could decrease the cost of operation and increase performance. With the added stability of the new design, another attempt at using moissanite anvils would be of interest. As mentioned in Section 3.1.4, compared to the cost of diamond anvils, there is great appeal to the moissanite anvils.

The current method to keep the diamonds parallel to one another could also be improved. As mentioned in Section 2.1.1.2, the preferred method of determining where the anvils are parallel is to bring the diamonds to within nanometers of one another allowing for visual observation of the fringes of visible light between the optically flat diamond tips.

Chapter 4

Interaction of Light with Matter

When electromagnetic radiation is incident on a material it will be either transmitted, specularly reflected, or absorbed with possible reemission. Transmission is the process by which only a decrease in propagation speed is observed dependent on the index of refraction, $v = c/n$. Specular reflection occurs when radiation bounces off a smooth surface. Of primary interest to this thesis is the interaction of light with matter via luminescence, scattering or diffraction.

4.1 Optical Measurements

Optical measurements reported in this thesis were performed using the system depicted in Figure 4.1. For all optical measurements a single crystal sample with a typical size of 0.05 mm was used. The sample (designated as the diamond anvil cell in Figure 4.1) was mounted on a glass slide for ambient condition measurements. For high pressure measurements the sample was loaded into a diamond anvil cell and additionally into a cryostat for high-pressure, low-temperature measurements. As detailed in Chapter 2, a pressure sensor and

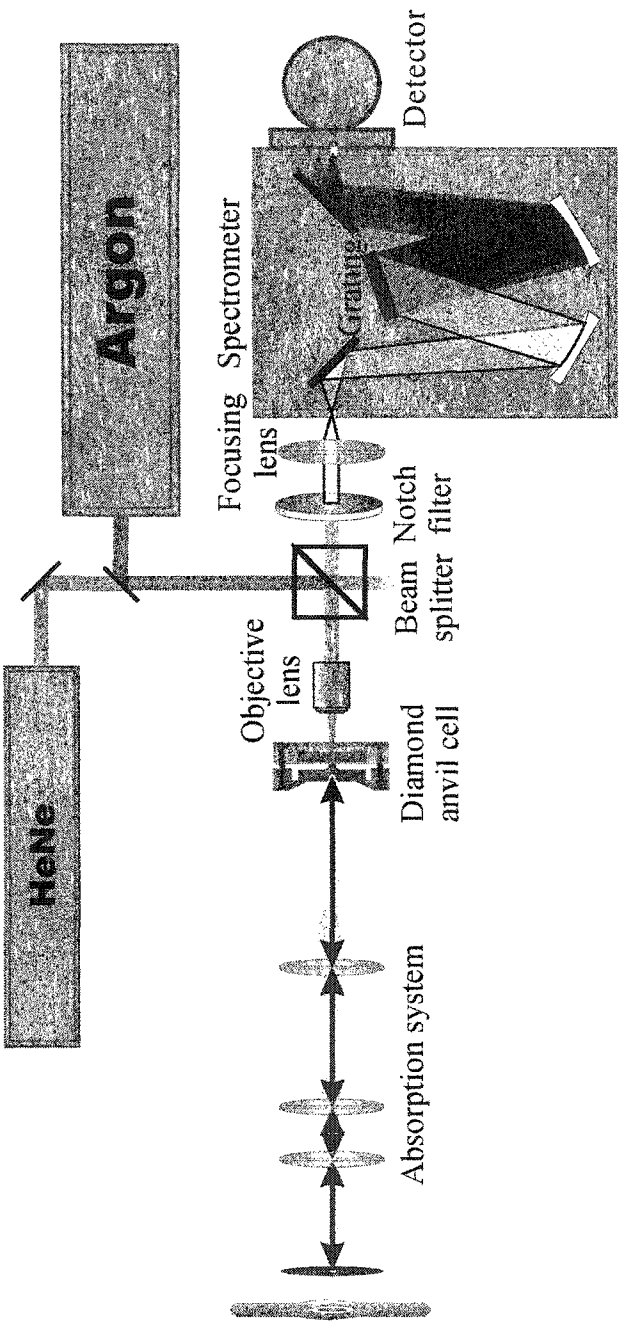

Figure 4.1: Optical system schematic (not to scale).

the pressure medium were loaded along with the sample into the diamond anvil cell.

The spectra were all recorded with a 0.275 m Czerny-Turner spectrograph, SpectraPro 275 (Acton Research Corporation) and a nitrogen cooled CCD detector with a resolution of less than 2 cm^{-1}. The system is designed to toggle between a He-Ne laser, 632.8 nm (1.96 eV), and a 514.5 nm (2.41 eV) argon laser. Peak devolution of all data was performed using the program *Grams* [41]. In subsequent sections, further detail of the experimental setup for specific measurements is discussed.

4.2 Luminescence

Following absorption and excitation, various competing processes occur within a molecule that unpopulate the excited states. These processes are depicted in Figure 4.2, some of which result in emission. If an molecule is in an excited vibrational state, vibrational relaxation occurs (~10^{-12}s). This is the process whereby a molecule loses energy to reach the lowest vibrational energy state of a given energy level. The energy dissipates non-radiatively. Once the electron is in the lowest vibrational level, several competing processes occur to return the energy to the electronic ground level. Some non-radiative relaxations include: internal conversion (~10^{-13}s) to a state with the same spin multiplicity; external conversion through energy transfer with neighboring molecules; and intersystem crossing (~10^{-7}s) to a state of different spin multiplicity.

4.2.1 Luminescence Theory

Luminescence is a spontaneous, radiative relaxation process with a measurable time delay between absorption and reemission. Luminescence can occur via light absorption (photo-

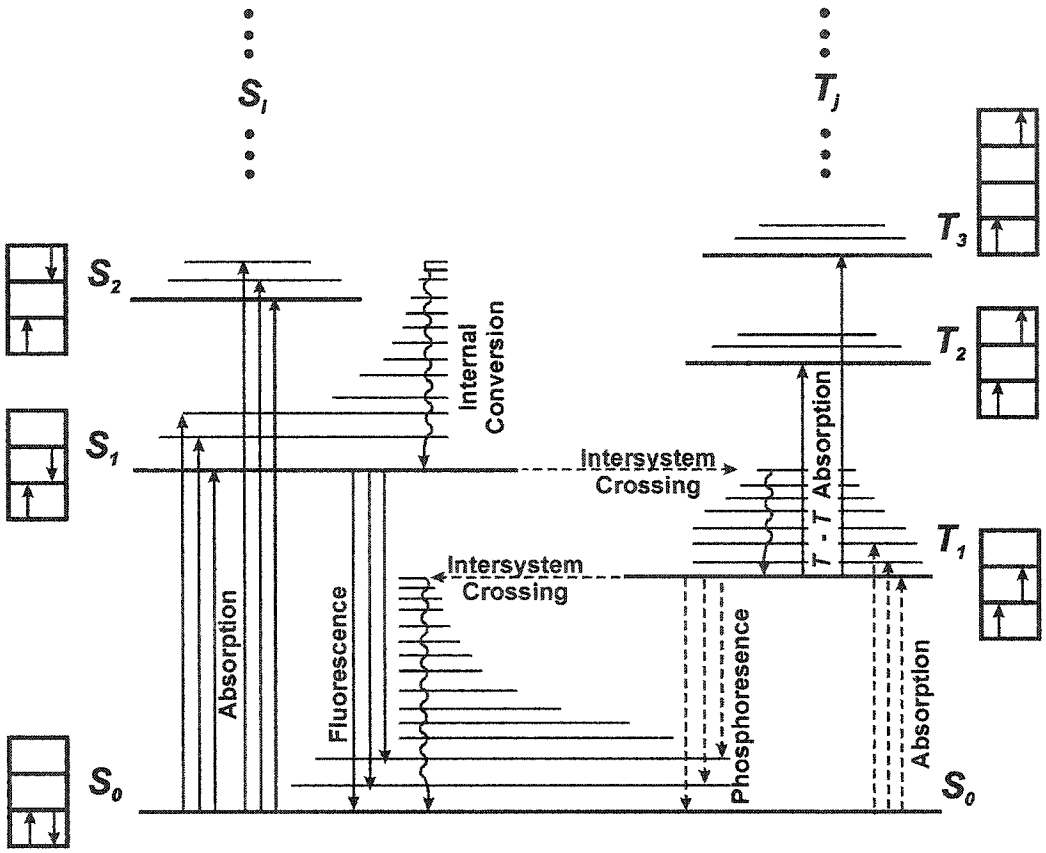

Figure 4.2: Jablonski Diagram [42]

luminescence), chemical reactions in living organisms (bioluminescence), other chemical reactions (chemiluminescence), electrical current (electroluminescence), etc. Experiments discussed in this thesis are nonresonant photoluminescence experiments. Luminescence peaks are independent of excitation wavelength because they are a measure of the energy difference between the excited and equilibrium states. Nonresonant luminescence occurs when the energy of the absorbed radiation is greater than the energy of the emitted radiation. Depending on the time delay between absorption and emission, luminescence is further classified into either phosphorescence or fluorescence. Phosphorescence is a very rare emission with a long lifetime of ~10^{-2} to 100s and is due to a quantum mechanically forbidden transition from a triplet excited to a singlet ground state. Phosphorescence is not the process of interest to this thesis and further detail will be omitted. Experiments reported herein are measuring fluorescence due to an allowed transition from a singlet excited to a singlet equilibrium state. This process has a relatively short lifetime of ~10^{-9} to 10^{-5} s.

4.2.1.1 Luminescence in Semiconductors

Luminescence is used in the study of semiconductors to help illuminate band gap characteristics. The most common observable luminescence in semiconductors is between states in the conduction band and valence band. This is more commonly called recombination. When the highest valence band energy and the lowest conduction band energy exist at the same place in the Brillouin zone the material is a direct gap semiconductor. An indirect semiconductor is defined as having the highest valence band energy and the lowest conduction band energy exist at different places in the Brillouin zone. The intensity of luminescence for a direct gap material will be much higher than that for an indirect gap material due to the fact that the direct process is first-order while the indirect process is

second-order. The dominant recombination mechanism for direct gap semiconductors is luminescence, whereas for indirect gap semiconductors nonradiative processes are dominant.

4.2.1.2 Limitations

The limitations of luminescence spectroscopy are related to those of absorption spectroscopy since the amount of emission is directly related to the amount of absorption. The main advantage of luminescence over absorption is that luminescence intensity is proportional to incident power such that a more intense light source provides a more intense luminescence. When compared to absorption, the main disadvantages of luminescence are that processes such as phosphorescence, external conversion and intersystem conversion can compete with luminescence.

4.2.2 Experiment

To obtain luminescence spectra a laser beam was directed through a 50:50 beam splitter to an objective lens that focuses the beam to a spot size of about 5-10 μm onto the sample as shown in Figure 4.1. The emitted light loses 50% of the signal strength when passing back through the objective lens and the beam splitter. The signal then passes through a holographic notch filter to filter out Raleigh scattering and any stray laser reflections. The signal then passes into the spectrometer and detector. Luminescence emissions independent of excitation wavelength and emission peaks can occur relatively far from the wavelength of the laser. The diffraction grating must be rotated accordingly.

4.3 Raman Scattering

Another way that light interacts with matter is through scattering. Scattering can be described as the instantaneous redirection of light due to its interaction with matter which may or may not occur with a transfer of energy. Developments in light scattering began in 1869 with John Tyndall's colloidal investigations. Tyndall studied the intensity of scattered light from aerosols. This causes scattering at intensities high enough to be visible with the human eye. In 1899 Lord (John William Strutt) Rayleigh developed a theory which successfully explained that the blue sky and red sunsets are due to the scattering of electromagnetic radiation by independent particles whose size is much smaller than the wavelength of the incident radiation. In this situation the intensity of the scattered light is $I_{\text{Rayleigh}} \propto 1/\lambda^4$ so that blue scatters more intensely than red. Both Tyndall and Raleigh were studying scattering intensities in which the relative index of refraction is approximately equal to one. In 1908, Gustav Mie developed a theory to explain scattering intensities for particle size on the order of the incident wavelength. This type of scattering is called Mie scattering and, unlike Rayleigh scattering, is not strongly wavelength dependent. Others also contributed to scattering intensity theories in the early 20^{th} century including P. Debye, R. Gans, F. Zernike, T.H. Prins, M.V. Smoluchowski and A. Einstein [43].

Parallel to the developments of light scattering intensity theory detailed above, there was also experimental and theoretical progress in the frequency distribution of scattering. In 1914 Leon Brillouin predicted the inelastic scattering of light from acoustical phonons. In 1930 E.F. Gross experimentally observed inelastic scattering in liquids. In 1923 Adolf G. Smekal predicted inelastic scattering by optical phonons. Theoretical descriptions by Kramers and Heisenberg, Schrödinger, and Dirac soon followed. In 1928 Sir Chandrasekhera Venkata Raman observed this inelastic scattering by optical phonons. With

the development of lasers in the early 1960s measurements of both frequency changes and other types of scattering became more accessible. Tyndall, Mie, and Rayleigh scattering are all examples of elastic scattering. Brillouin scattering. on the other hand, is an example of inelastic scattering by acoustic phonons with a shift of 0.1 to 1 cm^{-1}. Inelastic scattering of light by optical phonons, with shifts up to 4000 cm^{-1}, is called Raman scattering and is the type of scattering focused on in this thesis.

4.3.1 Raman Scattering Theory

The Raman effect occurs when light is inelastically scattered at optical frequencies and can occur with a change in vibrational or rotational energy of a molecule. Only a small fraction of the incident light is scattered in this way, approximately 1 in 10^7 photons. Work herein is primarily concerned with the vibrational Raman effect.

4.3.1.1 Vibrational Modes

The assumption of a static lattice does not explain the Raman effect. A dynamic latice theory of lattice vibrations is required instead. Raman spectroscopy is sensitive to both molecular (internal) vibrations and lattice (external) vibrations. Each atom in a molecule vibrates about its equilibrium position. This motion creates distortions of the molecule's symmetry which fall into two main categories, stretching and bending. Stretch modes involve a change in interatomic distances along chemical bonds and bending involves the change in the angle between two bonds. Lattice vibrations occur due to interactions of many molecules or, in the case of an atomic material, many atoms. Lattice vibrations are found at lower frequencies than molecular vibrations.

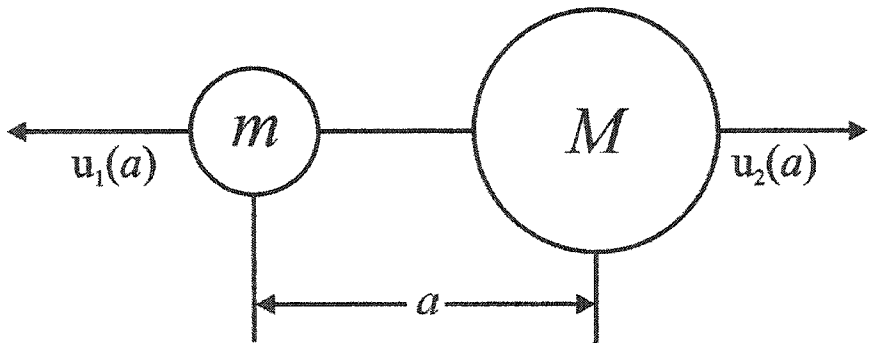

Figure 4.3: Diatomic Molecule.

Classical Treatment Following the treatment by Ferraro et al. [44], in order to illuminate the mechanism of molecular vibrations the normal modes for a diatomic molecule are derived by comparing the molecule to a simple harmonic oscillator with potential energy

$$U^{\text{harm}} = \frac{K}{2}\left[u_1(a) - u_2(a)\right]^2 \tag{4.1}$$

As seen in Figure 4.3, the displacement from equilibrium for the ions of mass m and M is $u_1(a)$ and $u_2(a)$, respectively, with equilibrium positions na. K is a measure of the force between the ions. Solving the equations of motion with $u_1(a) = A_1 e^{i(ka-\omega t)}$ and $u_2(a) = A_2 e^{i(ka-\omega t)}$ yields a single vibrational mode with frequency

$$\omega = \sqrt{\frac{K(m+M)}{mM}} \tag{4.2}$$

This vibrational mode is in addition to the three translational and two rotational modes of the system. Solving for frequencies of a polyatomic molecule is more complicated and beyond the scope of this thesis. Qualitatively it can be seen that an isolated molecule of n atoms has 3n degrees of freedom which can be classified as translational, rotational, or

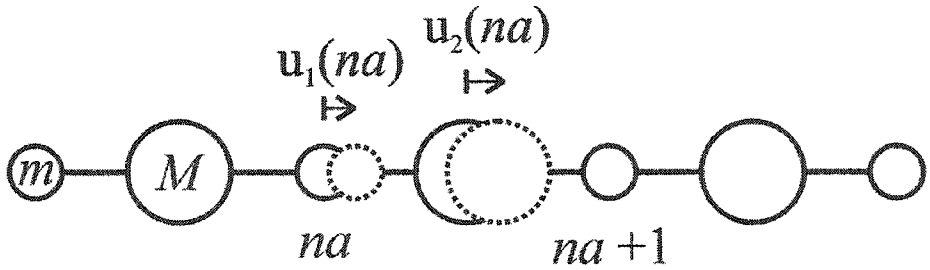

Figure 4.4: Diatomic Linear Chain.

vibrational motion. Three of these degrees of freedom are translational modes along each of the three axis. A linear molecule has two rotational modes and a non-linear molecule has three. This leaves 3n-5 and 3n-6 vibrational modes for a linear and non-linear molecule, respectively.

Vibrational modes are not limited to only intramolecular vibrations, but also include intermolecular or lattice vibrations. Following the treatment by Ashcroft and Mermin [45], the origin of the vibrational modes for a three dimensional lattice can be illuminated by studying the diatomic linear chain. Consider a harmonic approximation for the motion of both atoms in the unit cell. This approximation assumes that each atom will not significantly diverge from its equilibrium position. For a one-dimensional diatomic linear chain, the potential energy between nearest neighbors can be written as

$$U^{\text{harm}} = \frac{K}{2} \sum_{n} \left[u_1\left(na\right) - u_2\left(na\right)\right]^2 + \left[u_2\left(na\right) - u_1\left(\left[n+1\right]a\right)\right]^2 \tag{4.3}$$

As seen in Figure 4.4, the displacement from equilibrium for the ions of mass m and M is $u_1\left(na\right), u_1\left(na+1\right), u_1\left(na+2\right), \cdots$ and $u_2\left(na\right), u_2\left(na+1\right), u_2\left(na+2\right), \cdots$ respectively with equilibrium positions na, $na+1, \cdots$. K is a measure of the force between the ions. Solving the equations of motion with $u_1\left(na\right) = \epsilon_1 A e^{i(kna-\omega t)}$ and $u_2\left(na\right) = \epsilon_2 e^{i(kna-\omega t)}$

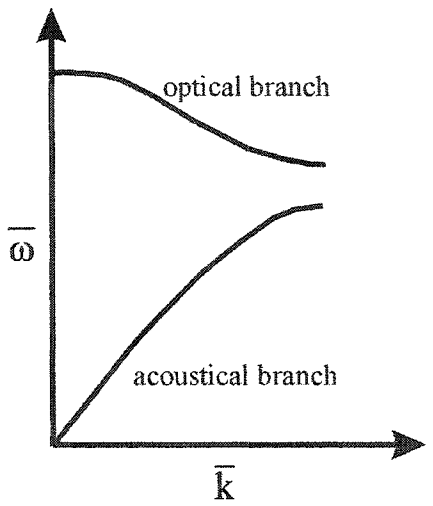

Figure 4.5: Dispersion Relationship

yields the following frequency values:

$$\omega^2 = \frac{K}{Mm}\left(M + m \pm \sqrt{M^2 + m^2 + 2Mm\cos kna}\right) \tag{4.4}$$

This solution tells us that for a chain with two atoms in each of P primitive cells, there exist two solutions of allowed frequencies for each of the P values of k for a total of $2P$ normal modes. Figure 4.5 is a plot of ω versus k, the dispersion relation. The allowed frequencies are split into two different branches, the lower branch shows allowed frequencies for acoustical phonons and the upper branch for optical phonons. Acoustical phonons have a shift of 0.1 to 1 cm^{-1} and are detected with Brillouin scattering. Raman scattering detects optical phonons with shifts up to 4000 cm^{-1}. The vibrational frequencies which exist for any given sample are based on the specific chemical groups.

The frequency derivation for a three dimensional system is complicated and beyond the scope of this thesis. However, it can be seen that there exist $3N$ normal modes for a three dimensional system where N is the total number of atoms in the solid. These $3N$ modes are

divided into 3 acoustical modes, corresponding to the translational modes of the system, and $3N-3$ optical modes. If there exist M molecules in the system, the optical modes can be further classified into $3N-6M$ molecular and $6M-3$ lattice modes. Since $N \gg M$, the vast majority of vibrations are molecular and will be the bulk of discussion to follow.

It must be noted that, unlike a classical harmonic oscillator, vibrations have discrete energy values [46] of

$$E_n = \left(n + \frac{1}{2}\right)\hbar\omega_n \tag{4.5}$$

where n is the excitation number of the normal mode and is restricted to values of 0, 1, 2, ... and ω_n is the corresponding frequency of that mode. The separation between levels is typically a fraction of an eV and all excitations are designated as either fundamental modes, overtones, or combination modes. Fundamental modes consist of all vibrations excited from the ground state to the first excited state. Vibrations excited from the ground state to any excited state except the first are called overtones and a combination mode is a two or more phonon event.

Because the maximum Brillouin zone k-vector is typically ~10^8 cm^{-1}, phonons excited by the scattering of visible light, ~10^5 cm^{-1}, are in the immediate vicinity of $k = 0$. This type of scattering is called Brillouin scattering if the acoustical phonons are detected and Raman scattering if optical phonons are detected. As mentioned previously, measurements discussed in this thesis are based on Raman spectroscopy and any further discussion of Brillouin spectroscopy will be omitted.

4.3.1.2 Pressure Effects on Vibrational Modes

As the pressure is increased the phonon modes change. The normal behavior of phonon modes is an increase in the frequency of vibration with increasing pressure. This is due

to the increased interaction between molecules and atoms as they get closer to one another with increasing pressure. Soft phonons behave in the opposite manner; as pressure increases the frequency of vibration of soft phonons decreases. This is an indication of the force between molecules or atoms decreasing with increasing pressure and is indicative of lattice softening with increasing pressure. This behavior is an indication of lattice instability and often leads to a phase transition [47].

4.3.1.3 Vibrational Raman Effect

As mentioned above, the vast majority of scattering is elastic Rayleigh scattering. A small number of photons, about 1 in 10^7 , are inelastically scattered by optical phonons. This is the Raman effect and occurs in 10^{-14} seconds or less. Classically, the interaction can be thought of as a perturbation of the electric field of the molecule by the incident radiation. Quantum mechanically, the interaction is viewed as an excitation from an initial vibrational level to a virtual state with almost immediate deexcitation to a different vibrational level.

Classical Treatment Following the treatment by Ferraro et al. [44], the main features of Raman scattering can be explained classically. When a photon is incident on a molecule, the electric field, $\mathbf{E} = \mathbf{E}_0 \cos \omega_0 t$, of the photon induces electric and magnetic multipole moments in the molecule. The contribution from magnetic multipoles and electric quadrupoles and higher are typically several orders of magnitude smaller than that of the oscillating electric dipole moment. Thus the contribution of the electric dipole moment, $\mathbf{P}$, will be the only concern in this thesis. The induced electric dipole moment is

$$P = E\alpha + \frac{1}{2}\beta E^2 + \frac{1}{6}\gamma E^3 + \cdots \tag{4.6}$$

and depends on the polarizability, α, the hyperpolarizability, β, the second hyperpolarizability, γ, etc. Only for nonlinear Raman scattering do the second and higher terms contribute significantly. For experiments of interest herein the dipole moment of the molecule can be simplified to

$$\mathbf{P} = \alpha\mathbf{E} = \alpha\mathbf{E}_0 \cos\omega_0 t \tag{4.7}$$

The polarizability is a measure of the ease with which the electron cloud around a molecule can be distorted and is unique for every molecule. Due to the coupling between electron and phonon, the polarizability can be expanded in a Taylor series as

$$\alpha = \alpha_0 + \left(\frac{\partial\alpha}{\partial q}\right)_0 q + \frac{1}{2}\left(\frac{\partial^2\alpha}{\partial q^2}\right)_0 q^2 + \cdots \tag{4.8}$$

where

$$q = q_0 \cos\omega_n t \tag{4.9}$$

is the generalized phonon coordinate where q_0 is the vibrational amplitude, and ω_n is the frequency of vibration. For small vibrational amplitudes, α is a linear function of q and, using the only the first two terms in equation 4.8,

$$\mathbf{P} = \alpha_0\mathbf{E}_0 \cos\omega_0 t + \frac{1}{2}\left(\frac{\partial\alpha}{\partial q}\right)_0 q_0\mathbf{E}_0 \left[\cos\left(\omega_0 - \omega_n\right)t + \cos\left(\omega_0 + \omega_n\right)t\right] \tag{4.10}$$

The first term represents an oscillating dipole scattering light elastically in all directions at the same frequency, ω_0, as the incident wave (Rayleigh scattering). The last two terms represent the inelastic scattering of light (Raman scattering) shifted from the incident frequency to frequencies $\omega_0 - \omega_n$ (Stokes shift) and $\omega_0 + \omega_n$ (anti-Stokes shift) respectively. This shift in frequency is a direct measure of the frequency of induced vibration and is thus

independent of incident wavelength.

4.3.1.4 Selection Rules and Polarizability Ellipsoid

Not all vibrational modes are Raman active. As can be seen from equation 4.10, the second term vanishes if $(\partial\alpha/\partial q)_0 = 0$ and only Rayleigh scattering occurs. This indicates that in order for a particular vibrational mode to be Raman active, the polarizability must change with the vibration. The second-rank polarizability tensor is

$$\alpha = \begin{pmatrix} \alpha_{xx} & \alpha_{xy} & \alpha_{xz} \\ \alpha_{yx} & \alpha_{yy} & \alpha_{yz} \\ \alpha_{zx} & \alpha_{zy} & \alpha_{zz} \end{pmatrix} \tag{4.11}$$

For small molecules, a graphical interpretation of the polarizability tensor is sometimes helpful as a tool for determining Raman activity. This graphical interpretation is called the polarizability ellipsoid and has the form [48]

$$\alpha_{xx}x^2 + \alpha_{yy}y^2 + \alpha_{zz}z^2 = 1 \tag{4.12}$$

if the ellipsoid has its center at the origin of the coordinate system where x, y, and z are the directions of the axis of the ellipsoid. A line drawn to the surface of the ellipsoid in the i-direction has a length $1/\sqrt{\alpha_i}$. If the size, shape, or orientation of the ellipsoid changes during a vibration then that vibration is Raman active.

Quantum Mechanical Treatment As discussed previously, the incident photon can scatter elastically or inelastically at a frequency greater than or less than that of the incident photon. The difference between these three scattering processes is depicted visually in

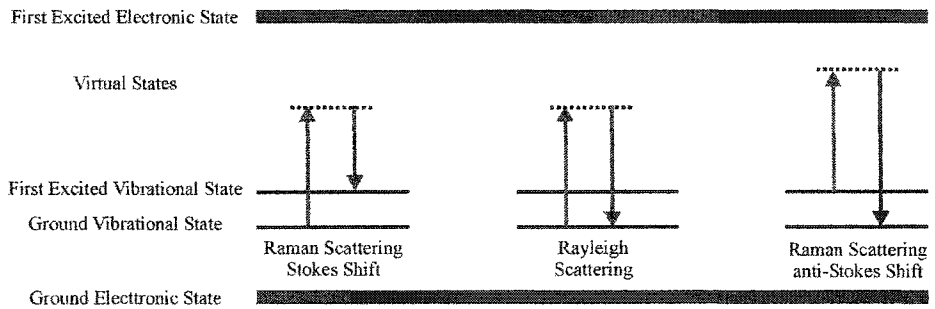

Figure 4.6: Raman and Rayleigh Energy Level Diagram [49].

Figure 4.6.

Although Stokes and anti-Stokes frequencies are both shifted from the Rayleigh line by the same frequency, ω_n, the intensity of the two lines is markedly different. As seen in Figure 4.6, Stokes excitations occur from the ground state to an excited state. Conversely, anti-Stokes excitations occur from an excited state to the ground state. At ambient temperature, the excited state is much less populated than the ground state as determined by the Bose-Einstein distribution. The anti-Stokes intensity is therefore much less than the Stokes intensity. Since population is temperature dependent so are Stokes and anti-Stokes emission intensities. The ratio of intensities is [48]

$$\frac{I_S}{I_A} = \left(\frac{\nu_0 - \nu_n}{\nu_0 + \nu_n}\right)^4 e^{\frac{h\nu_n}{kT}} \tag{4.13}$$

where I_S and I_A are the Stokes and anti-Stokes intensities, respectively.

The scattering process can be described as an excitation from one energy level to a virtual state, and an emission to another energy level (Raman scattering) or the same energy level (Rayleigh scattering). The difference in energy between the virtual state and the initial vibrational energy level of the molecule is equal in energy to the energy of the incident photon. A true vibrational level most likely does not exist at this energy. This indicates the

existence of a virtual state between energy levels that does not necessarily correspond to a true state.

For a transition to be Raman active, the polarizability must change from the initial state, ψ_v, to the final state, $\psi_{v'}$. According to quantum mechanics, the selection rules are determined by

$$[\alpha_{ij}]_{v,v'} = \int \psi_v^* (q)\, \alpha_{ij} \psi_{v'} (q)\, dq \tag{4.14}$$

where $i, j = x, y, z$, v and v' are the initial and final states of the system respectively, and q is the nuclear displacement defined by equation 4.9. If any one of these integrals is non-zero the vibration is Raman active. This can be seen by substituting equation 4.8 into equation 4.15 such that

$$[\alpha_{ij}]_{v,v'} = (\alpha_{ij})_0 \int \psi_v^* (q)\, \psi_{v'} (q)\, dq + \left(\frac{\partial \alpha_{ij}}{\partial q}\right) \int \psi_v^* (q)\, q \psi_{v'} (q)\, dq + \cdots \tag{4.15}$$

Since ψ_v and $\psi_{v'}$ are eigenfunctions of the same Hamiltonian, the first term of equation 4.15 is zero for all $v \neq v'$. The second term of equation 4.15 is non-zero only when $\Delta v = \pm 1$. This follows from the quantum mechanical properties of the harmonic oscillator in which

$$\langle v' | \, q \, | v \rangle \sim \sqrt{v} \delta_{v',v-1} + \sqrt{v+1} \delta_{v',v+1} \tag{4.16}$$

4.3.1.5 Raman Scattering vs. Infrared Absorption

No discussion of Raman spectroscopy is complete without at least a brief comparison to infrared absorption. As with Raman scattering, infrared absorption can measure the vibrational energies of molecules. The mechanism which excites these vibrational modes is fundamentally different. Raman scattering is due to a change in polarizability due to the

electric field of the incident photon. In order for a vibrational mode to be IR active the dipole moment of the molecule must change from the initial state to the final state.

There are several advantages of Raman over IR [44]: air sensitive compounds can be placed in glass tubing which is not possible with IR because the glass absorbs IR radiation; similarly, water is a strong IR absorber so Raman scattering is ideal for samples in aqueous solution; no backgruond subtrattion has to take place with Raman spectroscopy; and a larger wavelength region can be covered by a single spectra in Raman versus IR.

4.3.2 Experiment

Raman spectra are obtained using the procedures and optical setup described in Section 4.2.2. The only difference between the optical setup for the two types of measurements is the position of the diffraction grating. Compared to luminescence, Raman scattering peaks are relatively close to the excitation wavelength of the laser and the diffraction grating must be rotated accordingly.

4.4 Energy Dispersive X-ray Diffraction Measurements

Since the discovery of X-rays in 1895 by W.C. Röntgen, the ways in which X-rays interact with matter have been studied extensively. Two such interactions are the photoelectric effect and Compton scattering. Photoelectric absorption is the process by which an incident X-ray gives all of its energy toward the ionization of an atom. The ejected electron has a kinetic energy equal to the energy of the incident X-ray less the binding energy of the electron. This process is the dominant absorption process for X-rays below 50 keV. The inelastic scattering of X-rays from an atom's electron density is called Compton scattering

and is the primary method of absorption of photons between 100 keV to 10 MeV. If the incident X-ray is of high enough energy, an electron will be ejected from the atom and a lower energy X-ray will be scattered. This work is primarily concerned with diffraction of X-rays in the energy range from about 1 to 100 keV. Diffraction describes the elastic scattering and subsequent interference of high energy photons (X-rays) or high energy particles such as neutrons. Unlike neutrons which diffract from the nucleus of an atom, X-rays diffract from the electron density. This work specifically concentrates on the crystal X-ray diffraction.

Developments in X-ray diffraction [50] began in 1912 when Max von Laue first observed the phenomenon. A year later W. L. and W. H. Bragg [51] reported intense peaks of diffracted radiation occurring at specific incident wavelengths and directions. The analytical method they developed from this observation is still used today and discussed in more detail in the next section. Other early 20^{th} century developments in X-ray science include: the discovery of characteristic X-ray radiation by Barkla and Sadleri; the development of quantitative X-ray spectroscopy by Moseley; Meitner's discovery of Auger electrons [1]; and the development of more energetic particle accelerators. The desire to study the composition of the atom led to the development of particle accelerators. In order to accelerate particles to higher speeds, researches used magnets to create a circular path for the particle to travel. This circular path allowed for the particle to pass through the same accelerating components over and over again, increasing its speed with each pass. Once these accelerators were energetic enough to cause the charged particles to travel at relativistic speeds, synchrotron radiation was observed.

The first synchrotron was constructed in 1947 [50] at the GE Research Laboratory in

[1]Lise Meitner reported this discovery in 1923[52], two years before the independent discovery by Pierre Auger.

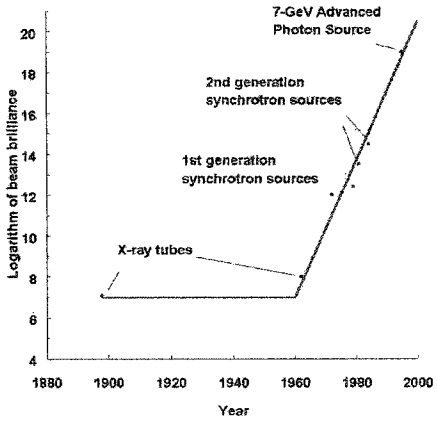

Figure 4.7: X-ray source history

Schenectady, NY, where synchrotron radiation was first observed. The first-generation of synchrotrons had the primary purpose of causing high energy particle collisions. Synchrotron radiation experiments performed at these facilities spurred the construction of second-generation synchrotrons dedicated to the production of synchrotron radiation. Development of synchrotron sources is now in the third-generation of development with emphasis on brightness. These synchrotrons provide X-ray intensities more than one trillion times higher than non-synchrotron X-rays. Figure 4.7 [53] displays a time line of the development of X-ray sources versus the corresponding beam brilliance. Diffraction of synchrotron X-rays is of interest in this thesis and described in more detail in Section 4.4.2.3.

4.4.1 X-ray Diffraction Theory

Typical interatomic distances are on the order of Ångstroms. An electromagnetic probe of the atomic structure of a solid must therefore have a wavelength at least this short. The energies of hard X-rays range from about 1 keV to 120 keV. These energies correspond to the order of interatomic spacings, 12.4 Å to 0.1 Å respectively, and interact primarily with

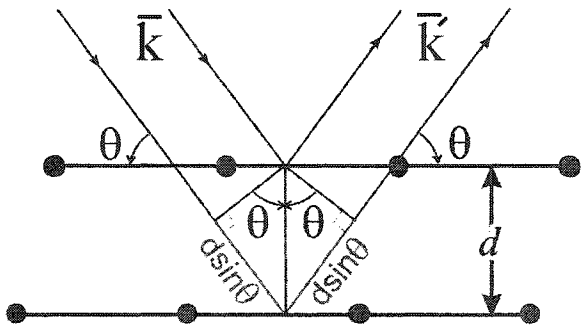

Figure 4.8: Bragg Reflection.

the electron density of the sample. X-ray diffraction can be used to analyze and characterize bulk properties of the solid.

4.4.1.1 Bragg Equation

In order to observe a sharp peak during diffraction the following conditions must be met: X-rays should be specularly reflected (incident angle = reflected angle) by the ions in any plane and reflected X-rays from successive planes should interfere constructively. The path difference for any two X-rays is $2d\sin\theta$ (see Figure 4.8). For constructive interference $n\lambda = 2d\sin\theta$ where n is the order of reflection from a given set of lattice planes, θ is the quarter-angle of the cone of the diffracted beam, λ is the incident X-ray wavelength, and d is the spacing between lattice planes. There are many ways to section the crystal into planes and, dependent upon crystal structure, some or all of these planes produce a reflection. Each plane is designated by the Miller indices h, k, and l. The distance between planes is thus d_{hkl}. Bragg's equation, for primary reflections, can be rewritten as

$$Ed_{hkl} = \frac{6.1993}{\sin\theta} \tag{4.17}$$

where energy is measures in keV and lattice spacing in Angstrom.

Limitations of Bragg's Law The derivation of Bragg's law assumes [45] that the atoms form parallel planes. If the translational symmetry of the sample is lost so also will the sharp diffraction peaks described above. The X-rays are assumed to be elastically scattered and the incident and reflected X-rays are represented as plane waves. Bragg's law also assumes kinematic diffraction in which the reflected wave has negligible interactions with the sample. This is a single scattering process resulting from the weak interaction of X-rays with matter. Kinematic diffraction accurately predicts the scattering intensities for the vast majority of samples and is mentioned in subsequent subsections.

4.4.1.2 Interplanar Spacing Formula

Depending on the diffraction method used the data collected is either intensity vs. energy at fixed θ or intensity vs. 2θ at fixed energy. For experiments of concern in this work all data are collected as intensity vs. energy (See Figure 4.10). For every energy peak displayed on a collected spectrum, a corresponding interplanar spacing, d_{hkl}, can be calculated using equation 4.17. The values of interest are not the interplanar spacing values, but the values of the lattice constants of the crystal. The interplanar spacing formula relates the Miller indices of a peak (*hkl*), the lattice constants (*abc*) and the interplanar d-spacing (d_{hkl}):

$$\frac{1}{d_{hkl}^2} = \frac{1}{V^2}\left[h^2b^2c^2\sin^2\alpha + a^2k^2c^2\sin^2\beta + a^2b^2l^2\sin^2\gamma + 2a^2bkcl\left(\cos\beta\cos\gamma - \cos\alpha\right)\right.$$

$$\left. +2ahb^2cl\left(\cos\alpha\cos\gamma - \cos\beta\right) + 2ahbkc^2\left(\cos\alpha\cos\beta - \cos\gamma\right)\right] \qquad (4.18)$$

where

$$V = abc\left(1 - \cos^2\alpha - \cos^2\beta - \cos^2\gamma + 2\cos\alpha\cos\beta\cos\gamma\right)^{1/2}$$

This is the most general case and simplifies for all crystal structures that are not triclinic. For example, the most simple case is that of the cubic lattice which has $a = b = c$ and $\alpha = \beta = \gamma = 90^{\circ}$. The interplanar spacing formula simplifies to

$$\frac{1}{d_{hkl}^2} = \frac{h^2 + k^2 + l^2}{a^2} \tag{4.19}$$

4.4.2 Experimental

Diffraction methods have been developed to ascertain information about the structure of a sample. Combinations of different methods allow researchers to determine a range of information such as lattice constant values, crystal structure and, in conjunction with pressure and temperature measurements, the equation of state of a crystal. As discussed below, for research reported herein, high-pressure, X-ray diffraction is undertaken using energy dispersive powder X-ray diffraction with a synchrotron source.

4.4.2.1 Single Crystal and Powder X-ray Diffraction

Both single crystal and powder X-ray diffraction measurements are commonplace. To determine each lattice spacing in a single crystal experiment the orientation of the crystal in relation to the incident beam must be changed. This type of experiment allows for both crystal structure and lattice constant determination. In a powder diffraction experiment the sample is ground sufficiently to allow for the incident beam to diffract from all orientations of the crystal in a single measurement. Lattice constant data can be acquired with this method, but due to problems such as preferred orientation and variation in the

incident X-ray flux the evaluation of intensity data for the structure determination is impossible. However, since all crystal orientations are represented in a single measurement, the experimental time is drastically reduced. For pressure measurements in a diamond anvil cell, powder X-ray diffraction is the favorable method. The design of the diamond anvil cell makes it impractical for single crystal experiments due to the difficulty of orienting a crystal in a DAC in a specific direction.

4.4.2.2 Energy and Angular Dispersive X-ray Diffraction

To ascertain information using equations 4.17 the incident energy and the diffraction angle must be known for each individual reflection. There are two different methods used to determine these values: angular dispersive and energy dispersive X-ray diffraction. Angular dispersive X-ray diffraction (ADXD) is a method in which a monochromatic beam of X-rays is incident on the sample. In most laboratories, the detector must sweep through 2θ, requiring many measurements to determine the full range of reflections. A more expensive, large area detector may also be used to collect over a large 2θ range at once. This technique is becoming more common and is being used at the high pressure beam lines of the new synchrotrons in the US and Europe. Energy dispersive X-ray diffraction (EDXD), on the other hand, involves a polychromatic energy source. The detector is fixed at a single 2θ and all energies are incident at once. Intense polychromatic sources (synchrotrons) are less common, but the multitude of measurements required for a single small area detector ADXD run is reduced to a single EDXD measurement. ADXD has a better overall accuracy and, using large area detectors, measurement time can be reduced significantly. However, EDXD is still used in many labs for high-pressure X-ray diffraction studies in a diamond anvil cell due to the fact that the design of the diamond anvil cell limits the 2θ range that

can be reached in ADXD.

4.4.2.3 Tube and Synchrotron Radiation [53, 54]

The two main sources for X-ray diffraction experiments are monochromatic beams from X-ray tubes and polychromatic beams due to synchrotron radiation. X-ray tubes accelerate electrons to energies of several hundred kilovolts. These electrons then strike a target made of a material such as copper. Due to the rapid deceleration of the electrons, a continuous spectrum of low intensity, bremsstrahlung radiation is produced with energies from a few keV to a maximum energy corresponding to that of the electron beam. In addition strong, discrete, X-ray energies corresponding to the K-shell emissions of the target material are produced. It is an intense K-shell emission line, such as copper K-α_1 ($\lambda = 1.5406$Å), which is used as a monochromatic X-ray source. This radiation is relatively easy to produce and is used widely for ADXD experiments, however the intensity is relatively low compared with the intensity of polychromatic synchrotron radiation. Due to the very small sample volumes used in a diamond anvil cell (<.005 mm^3), a single spectrum takes upwards of 24 hours to collect with an X-ray tube. Modern synchrotrons can generate radiation a trillion times more intense than that produced by current X-ray tubes and allow a spectrum to be observed in seconds.

Any accelerating charge emits radiation. As a charge moves it creates a radial EM field. This field becomes distorted as the charge is accelerated. This distortion, moving away from the charge at the speed of light, is seen as radiation emitted from the particle. This is synchrotron radiation and can occur in particles accelerating either linearly or circularly. The amount of radiation increases as the speed of the particle increases. Linear accelerators need a relatively long distance to accelerate the particles to near the speed of light. A

circular path, on the other hand, allows the charged particle to travel through the same accelerating components over and over, leading to a smaller needed overall area.

One type of circular accelerator is called a synchrotron. Every synchrotron facility is composed of three base elements [55]: an injection system, a main storage ring and experimental beamlines. The injection system is designed to generate electrons and accelerate them to the operating energy of the storage ring. The main purpose of the storage ring is to steer and focus the electrons for hours at constant energy. The storage ring may also consist of insertion devices used to provide radiation characteristics optimized for specific experimental requirements. Lastly, experimental beamlines are designed for individual researchers to access the radiation. All diffraction measurements reported on in this thesis are based upon research conducted at the Cornell High Energy Synchrotron Source (CHESS[2]).

The injection system is typically composed of an electron source, a linear accelerator and a booster synchrotron. At CHESS [54], a heated filament emits electrons which are linearly accelerated to 300 MeV and injected into the booster synchrotron which further accelerates the particles to 5 GeV. The booster synchrotron is composed of both bending magnets and an acceleration section. The bending magnets deflect the electron beam in a series of 192 arced 3-meter long sections. Interspersed between these sections are four, three meter long radio frequency (rf) cavities which create an electric field that supplies the accelerating force. At 5 GeV the particles are traveling at 99.9999995 % the speed of light. It takes about 0.01 seconds for one of these particles to travel around the 575 m ring four thousand times. After the desired 5 GeV energy is achieved, in about ten minutes, the electrons are transfered to the Cornell Electron-positron Storage Ring (CESR).

[2]This work is based upon research conducted at the Cornell High Energy Synchrotron Source (CHESS) which is supported by the National Science Foundation and the National Institutes of Health/National Institute of General Medical Sciences under award DMR 9713424.

The storage ring consists of several key components: bending magnets, focusing elements, acceleration cavities and insertion devices. The bending magnets serve the same purpose as in the booster synchrotron. Because the particles need to remain in the storage ring for several hours, the beam must be continually focused so as to avoid deviation from the circular path. This focusing is achieved through the use of quadrupole and sextupole magnets. The synchrotron radiation emitted from the particles traveling in the storage ring is the X-ray radiation used by researchers at CHESS. This synchrotron emission causes an energy loss to occur in the particle beam. The energy of the particle beam is maintained by placing rf cavities along the path of the beam. These cavities accelerate the particles in such a way as to exactly compensate for the energy loss due to synchrotron emission.

Improvements in synchrotron facilities over the last 55 years have occurred through the use of different insertion devices. These improvements have drastically increased beam brilliance and allowed researchers to optimize radiation characteristics. Two types of insertion devices available at CHESS are wiggler and undulator magnets. Wiggler magnets, consisting of equal dipole magnets with alternating magnetic field directions, produce more intense, broader radiation beams than the standard bending magnets. Undulator magnets, of similar construction to wigglers, produce narrow, nearly monochromatic radiation. The research reported herein was taken with an X-ray diffraction beam enhanced by bending magnets only. Further discussion of insertion devices will therefore be omitted.

The B1 station is part of the National High Pressure Facility at CHESS and is specially equipped for diamond anvil cell experiments and was used for all experiments discussed herein. Before entering the station, the incident X-ray beam is stopped down to about 3 mm and can be further decreased by the downstream apertures to the final beam size of 5 to 500 μm (see Figure 4.9). The incident X-ray beam was collimated to $250 \times 250\,\mu m^2$ for

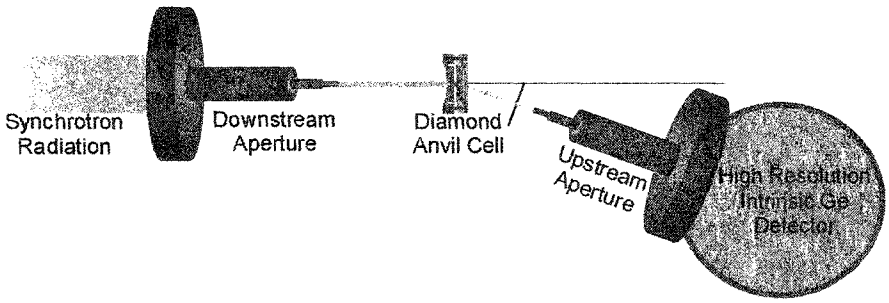

Figure 4.9: CHESS B1 Station.

experiments relevant to this work. The diffracted photons travel through the downstream aperture and are detected using a high resolution intrinsic germanium detector with resolution, $\frac{\Delta E}{E} = 128\,\text{eV}$. Detector calibration is achieved by using the emission lines of both a ^{133}Ba source and a ^{55}Fe source. The 2θ angle at which data were collected was calibrated using a gold foil.

4.4.2.4 Pressure Measurements

As discussed in detail in Chapter 2 the pressure sensor, which acts also as the pressure medium, was crushed together with the sample into a powder until individual crystal sizes are less than 1 μm. This mixture was then packed into the diamond anvil cell. Pressure was determined using the equation of state of NaCl or Au. The broad reflections of the pressure sensor, which in same cases even overlapped with reflections of the sample, resulted in a rather large error (± 0.2 to 1.0 GPa).

4.4.2.5 Data Analysis

As shown in Figure 4.10, diffraction spectra collected for this thesis are displayed as Intensity vs. Energy. Peak fitting and deconvolution was performed using *GRAMS* [41]. Each

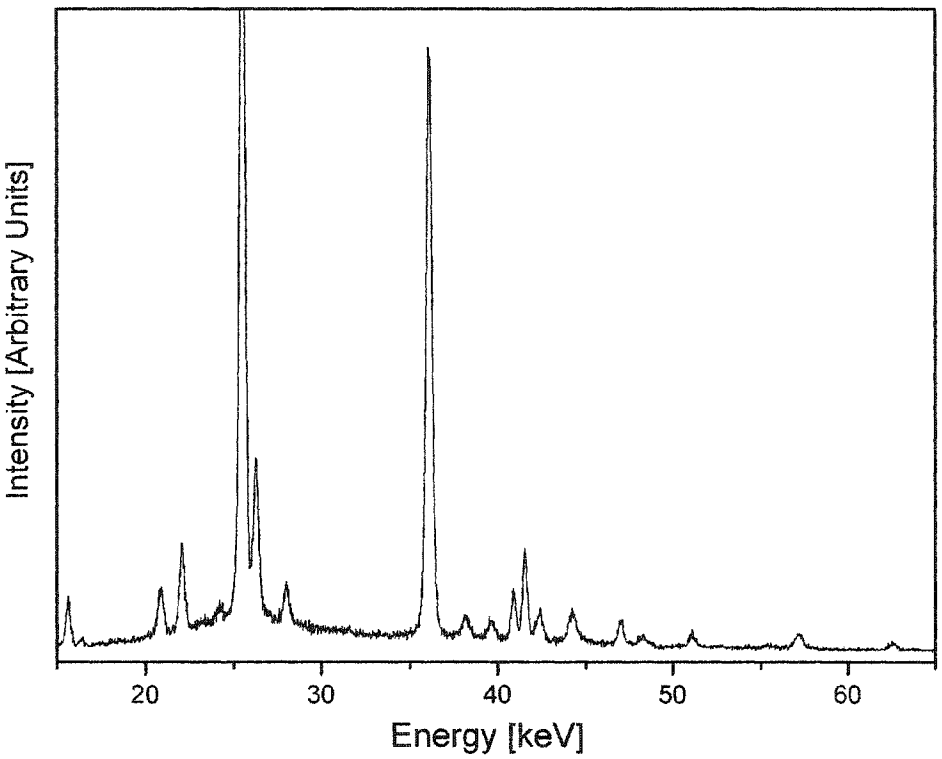

Figure 4.10: Typical energy dispersive x-ray diffraction pattern.

peak or set of overlapping peaks was fitted with a Gaussian function giving energy values for all reflections. Plugging the known detector angle and energy values into equation 4.17, d-spacings for all reflections can be calculated. The lattice constants can be refined using the interplanar spacing formula (equation 4.18) and all available values for d_{hkl} and the corresponding Miller indices, *hkl*. For work presented in this thesis a minimum of 10 reflections were used to refine the unit cell parameters. This refinement was performed using *U-FIT* [56]. As described in Chapter 6, once the lattice constants have been determined equations of state can be calculated.

Determining the appropriate corresponding *hkl* values for each reflection, called indexing the reflections, is difficult. Hundreds of different reflections can have a non-zero intensity as determined by equation **??**. If scattering intensity data were available these hundreds of choices could be narrowed down significantly. Unfortunately the inability to determine the scattering intensity of each reflection, as discussed in Section 4.4.2.1, leads to hundreds of indexing choices for the approximately 10 reflections used in the analysis.

4.4.2.6 Error in Analysis Procedure

This process requires a combination of several different analytical techniques. If care is not taken at each individual step, significant overall error can result. Fluctuations from measurement to measurement, in both sample and sensor peak intensity, and relative intensities between the two can cause problems in the peak fitting of the intensity verses energy data. These fluctuations arise from inhomogeneities of sample and sensor concentrations from spot to spot in the diamond anvil cell. These inhomogeneities can be minimized by spending adequate amounts of time preparing the powder mixture which is placed inside the diamond anvil cell. When more complex crystals are studied, sample peaks overlap with

one another and sample and sensor peaks may overlap. This leads to difficulty in consistent analysis from pressure to pressure and can result in error. The process taken to index the reflections also adds to the error as described in the previous subsection. Great pains must be taken in the data analysis process to accurately track, compare and fit individual peaks from pressure to pressure. In particular, error in pressure is very sensitive to error in energy. For example an energy value of 25.61 ± 0.10 keV translates to a pressure measurement of 5.74 ± 0.56 GPa.

Chapter 5

Additions and Improvements to Optical System and X-ray Analysis

5.1 Early Contributions by the Author

During the first several years of experiments, problems occurred with both X-ray diffraction measurements at Cornell and optical measurements at Colorado State University. The specific problems encountered led to improvements in X-ray data analysis and to the collection of more reliable optical data collection.

5.1.1 Problems Encountered

5.1.1.1 X-ray Data

A systematic approach to analysis of X-ray data had not been previously developed, creating inaccuracies in the determination of lattice constants. A systematic approach to the analysis was developed in order to obtain the level of reproducibility crucial for such small

parameter changes observed with high pressure X-ray diffraction. Improvements in X-ray analysis and CHESS system setup are discussed in the following subsections.

5.1.1.2 Optical Data

During the initial Raman experiments the main problems were data reproducibility. From one optical alignment to the next, for the same sample, drastic differences in peak intensities and vibrational mode energies were observed. Even more problematic was that with different excitation wavelengths, mode energy differences were recorded. It was concluded that the energy value fluctuations were a result of inadequate detector calibration procedures. The difference in intensity was established to be due to multiple problems with different components of the optical system. Correction of these problems led to the majority of the original system in the laboratory being improved, replaced, or newly designed. Changes include: improved alignment procedures that stabilized intensity readings; replacement of the focusing lens (see Figure 4.1) which must match precisely the numerical aperture of the detector to ensure maximum grating illumination; replacement of the beam splitter; addition of optics necessary to perform absorption measurements at low temperatures; the added ability to toggle between two different laser lines; and detailed documentation of system calculations and system alignment. As discussed in Section 5.3, final improvements to the optical system were made within the last year with the development of a more accurate calibration technique. Improvements to the optical system are discussed in the following subsection. Each improvement brought better reproducibility as well as enhanced intensity readings.

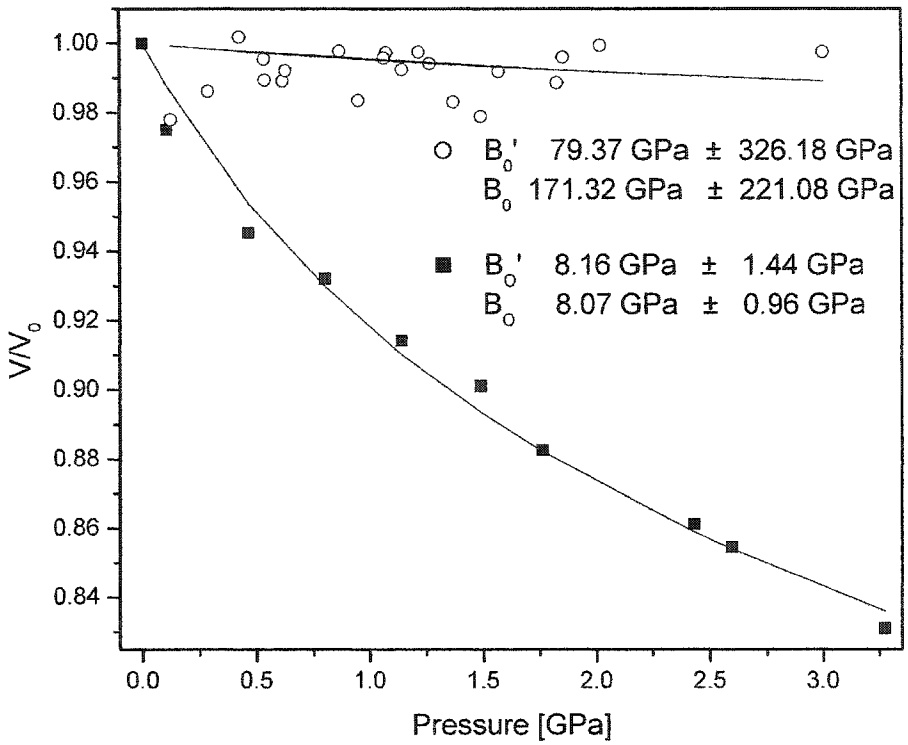

Figure 5.1: Equation of state data for $(NH_4)_2ZnCl_4$ displaying results from different analytical methods.

5.1.2 Improved Accuracy of X-ray Diffraction Measurements

As discussed in Section 4.4.2, analysis of X-ray diffraction data is a multi-step process with variations in sample peak intensity, number of sample peaks and possibly significant numbers of overlapping sample and/or sensor peaks. Previous analysis of X-ray diffraction data showed significant error in determination of the equation of state of $(NH_4)_2ZnCl_4$. Figure 5.1 shows the fit to the Murnaghan equation of state for two different X-ray diffraction analytical methods. The values for the determined bulk modulus and bulk modulus

derivative with their respective errors are also displayed. The data represented by open circles is an example of an analysis of the X-ray diffraction pattern performed by the author before development of this new analytical method. Not only is the data not smooth, but the resulting error in the values for the determined bulk modulus and bulk modulus derivative is obviously unacceptable. The data represented by squares in Figure 5.1 is an example of the smooth curve and reasonable bulk modulus values determined by the analytical method discussed above. This process by which fitting, tracking and comparing peaks from measurement to measurement as pressure is increased was developed. After repeated analysis of the data using this methodology, the standard deviation of the lattice constants was calculated to be $< 1\%$ of mean value. The standard deviation of the pressure was calculated to be $< 5\%$ of mean value.

5.1.3 Enhancements to Optical System

When research relevant to this thesis first began, there were several key elements with regard to alignment of the optical system which were incorrect or absent all together. These problems were corrected. As a result of the enhancements described in the next paragraphs, the recorded sample signal jumped by 350% from the original maximum obtained signal to the current average obtainable signal. This is illustrated in Figure 5.2.

The first adjustment to the optical system was accomplished by changing the height of the laser beam to match the height of the spectrometer. A new beam splitter stage was designed and installed which eliminated a previous hysteresis in the movement of the stage, allowing for better reproducibility. Furthermore, a calculation was performed (detailed in appendix A) to match the numerical aperture of the focusing lens to exactly match the numerical aperture of the spectrometer. If the numerical apertures of the two components

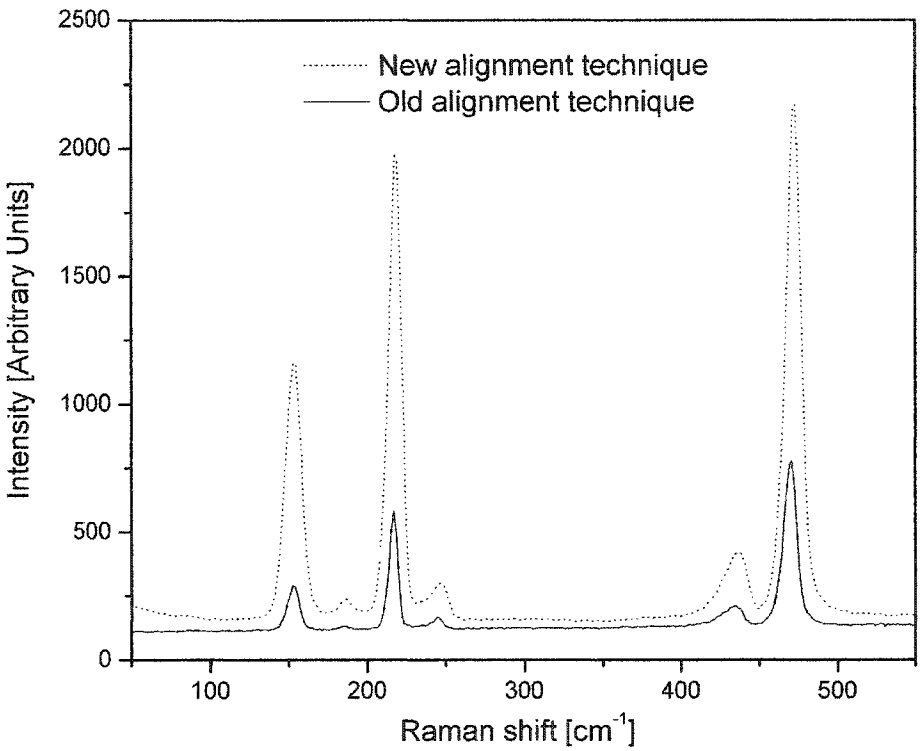

Figure 5.2: Sulfur spectrum before and after new alignment procedure.

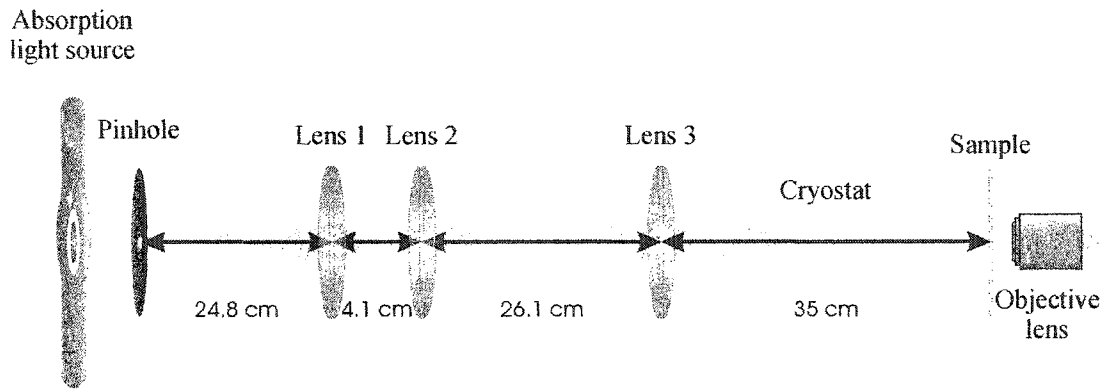

Figure 5.3: Absorption system.

do not exactly match then the diffraction grating is not completely illuminated resulting in a reduced resolution and loss of intensity.

5.2 Additions by the Author to the Optical System

Before research reported herein first began, an absorption setup existed to allow for high-pressure, room-temperature absorption measurements, but was unfortunately not compatible with the addition of a cryostat. A system was designed to perform high-pressure, low-temperature absorption measurements in addition to high-pressure, room-temperature absorption measurements.

Several requirements exist for low-temperature, high-pressure absorption measurements. Absorption measurements with a diamond anvil cell require the absorption lamp to be projected onto the sample to a very small spot size (~15 μm). In order to have room to position the cryostat for low-temperature measurements, there must be a large distance of 35 cm between the final focusing lens and the objective lens as shown in Figure 5.3. The combination of these two requirements and taking into account reasonable lens diameters and

focal lengths led to several calculations (detailed in appendix A). A 50 μm spot has been successfully projected through three lenses onto the sample. Due to the time consuming process of adjusting five separate optical components, each to within microns of the correct position, the desired projection of a spot size of 20 μm has not yet been achieved. This is discussed in more detail in Section 5.4.

Also added was the ability to toggle between the HeNe (632.8 nm) and the Ar (514.5 nm) lasers when previously a separate alignment for each laser had to be performed. This has resulted in a more efficient method of taking measurements with two different lasers. Detailed information of optical system alignment procedures, software uses and operation, data records for alignment to alignment comparison, and other laboratory information was documented for future laboratory students.

5.3 Calibration Improvements by the Author

The process of calibrating the optical system has been vastly improved over the original calibration procedure. When different laser lines were used to excite the sample, initial calibrations resulted in Raman spectra which were shifted in energy value. Figure 5.4 shows two such spectra recorded within seconds of one another, one with the argon laser and one with the HeNe laser.

Raman scattering measurements require the diffraction grating to be repositioned when the laser wavelength is changed. This must occur in order to insure that Rayleigh scattering is not in the range of the detector. It was determined that the difference in calibration was not due to the difference in laser wavelengths, but to the position of the signal relative to the diffraction grating. A detailed analysis of calibration curves for different wavelengths was performed. Three of these curves are shown in Figure 5.5. An ideal system would be

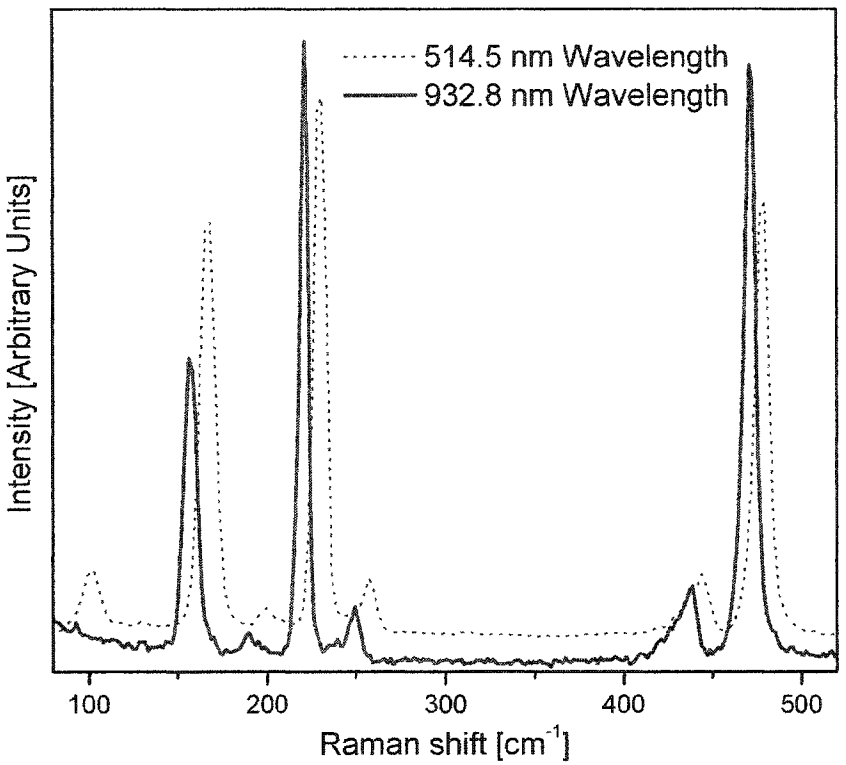

Figure 5.4: Spectra of sulfur excited by two different laser lines shows a bad calibration.

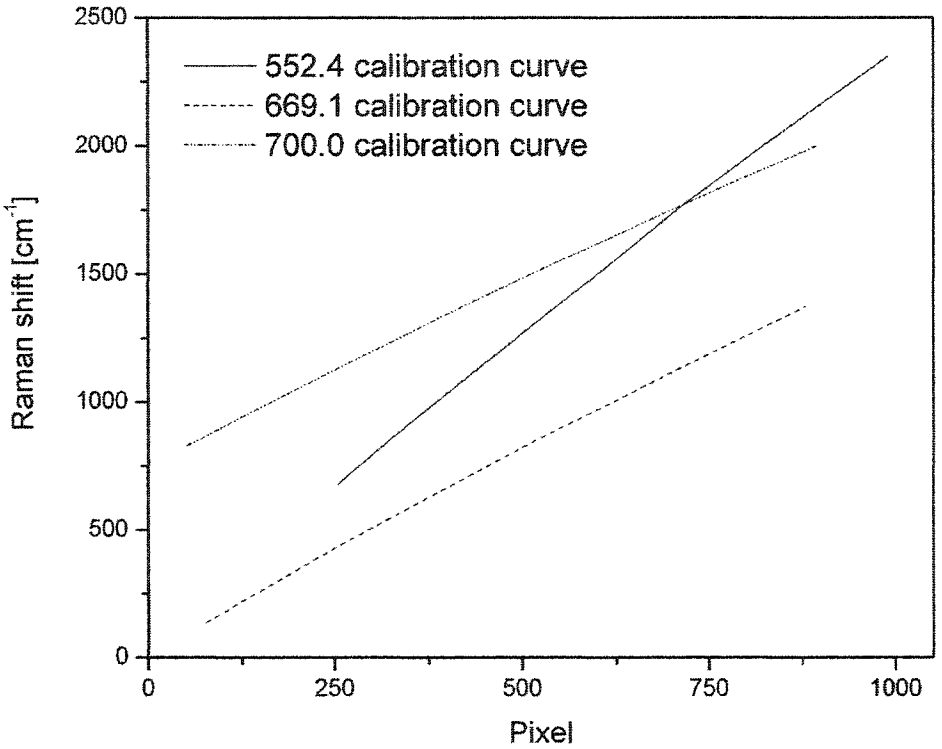

Figure 5.5: Calibration curves for 552.4 nm, 669.1 nm and 700 nm.

one in which the slopes of calibration curves at all wavelengths were equal. It is obvious from Figure 5.5 that this was not the case.

It was determined that this was a result of several different problems with the calibration technique. First, the spectrometer was at a fixed position relative to the rest of the optical alignment. This setup did not allow the spectrometer and detector to be aligned perpendicular to the rest of the optical system. Second, the lamp had been positioned directly in front of the detector (see Figure 4.1 for schematic). This allowed for the intensity of the calibration lamp to be maximum into the detector; however, it was impossible to align the lamp such that it was directed perpendicular to the detector. If the calibration lamp and sample signal are not incident perpendicular to the detector the scenario pictured in Figure 5.4 will arise due to the angular dependence of the wavelength to the diffraction grating.

In order to solve the problem, the previously fixed spectrometer was set to be adjustable. This now allows for the necessary perpendicular alignment. The calibration lamp was moved from directly in front of the detector and is now positioned at the focal point of the objective lens, the same place the sample is positioned so both the sample signal and calibration signal will enter the detector at the same angle. The result is a much more accurate and reproducible calibration as represented by the two spectra in Figure 5.6.

5.4 Future Direction

As mentioned in Section 5.2, the projection onto the sample of a 50 μm spot has been achieved; however, the desired projection of a spot size of 20 μm has not been. Each of the five optical components necessary for the measurement must be adjusted to within microns of the correct position. Due to the difficulty nature of this task better equipment, in particular additional stages, is needed to attain the goal of a 20 μm spot size.

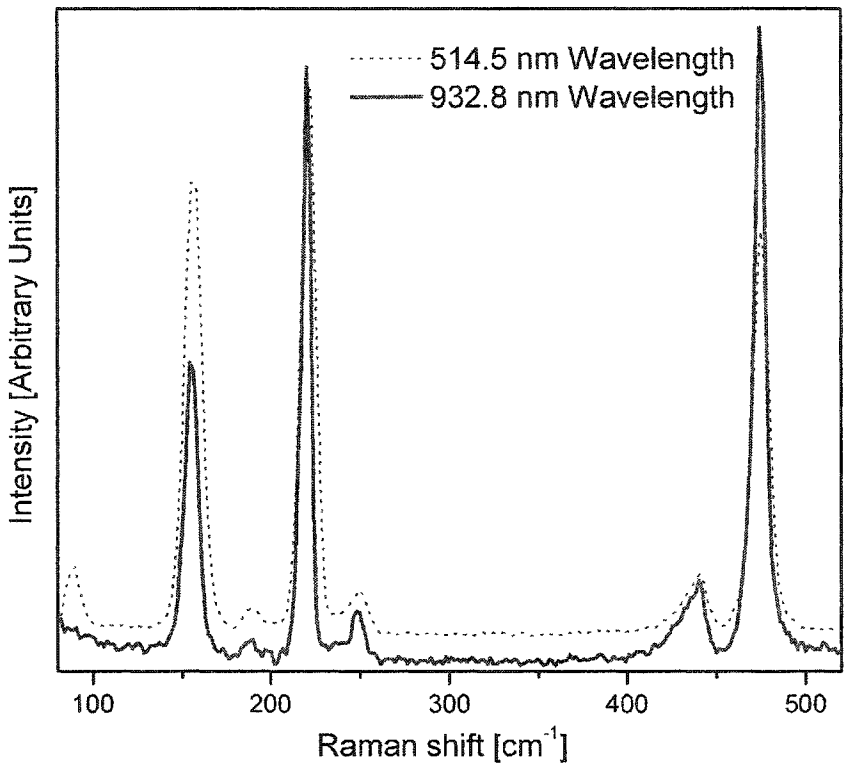

Figure 5.6: Spectra of sulfur excited by two different laser lines shows a good calibration.

One of the problems that remains is the loss of alignment every three to six weeks. The mirrors, are not as stable as are needed for a longer sustained alignment. Newer mounts would be a great help in correcting this problem. The current beam splitter in the system is a 50:50 beam splitter. This cuts the laser intensity to 50% at the sample and cuts the scattering intensity to 50% at the spectrometer. Now that the more powerful argon laser is aligned in the system there is more than enough laser intensity to produce the scattering necessary for the experiments. Because of this, a different beam splitter could be introduced which would cut the laser intensity at the sample but allow for a greater scattering intensity at the spectrometer.

Low temperature X-ray diffraction measurements would be of great interest. In order to successfully carry out these experiments, the compatibility of the cryostat and the experimental setup at CHESS will have to be analyzed. Upon zeroth approximation, the equipment at CHESS will most likely be incompatible with the cryostat and a new system will have to be designed. The distance between the downstream and upstream apertures (see Figure 4.9) may be too small for the cryostat to be inserted, especially when you add the tightening rods (see Figure B.2, Appendix B). If the cryostat fits without the tightening rods the time consuming process of removing parts of the setup to increase the pressure after every measurement must be taken into account. Assuming the cryostat can be inserted between the apertures, a detailed examination of the positions of the focal point of the apertures and the sample must be carried out to ensure they coincide. If the cryostat is incompatible, a massive, possibly impractical redesign of the system at CHESS will have to be undertaken.

Chapter 6

High Pressure Survey of $(NH_4)_2 ZnCl_4$

At ambient pressure, $(NH_4)_2 ZnCl_4$ (ammonium tetrachlorozincate) undergoes a series of structural phase transitions including a transition to an incommensurate phase. The phase transition series has been studied extensively at ambient pressure, but the equation of state has not been reported in the literature. This lack of data led to energy dispersive x-ray diffraction measurements reported in this thesis.

6.1 Incommensurate Materials

The topic of incommensurate materials is well reviewed by Cummins [57]. In general, a crystal is considered to be incommensurate if two or more properties of the crystal exist that have mutually incompatible translational symmetries. More specifically, incommensurate crystals possess three dimensional long range order, but there exists some local property of the crystal with a spatially periodic modulation of wavelength b that is incommensurate with the underlying lattice spacing a, i.e. the ratio b/a is irrational.

Materials with incommensurate phases have attracted considerable interest for several

reasons: due to the incommensurate modulation, the translational symmetry of the crystal is destroyed and the crystal is technically not in a true crystalline state; the modulation wave exhibits kinks called discommensurations or phase solitons; the soft-mode-driven lattice instability concept, previously applied to high-symmetry points in the Brillouin zone, is extended to arbitrary points; and the lattice dynamics of incommensurate phases differs substantially from that of ordinary crystalline phases. At the incommensurate transition temperature, T_i, the degenerate soft optic modes near $\pm\overline{q}_{ic}$ transform into two nondegenerate branches of modes. These are the amplitudon, a totally symmetric soft mode, and the phason, a unique gapless Goldstone mode with an approximately linear acoustic-type dispersion curve. These modes can couple to the acoustical modes and at the phase transitions cause anomalies in some of the elastic constants .

6.1.1 $(NH_4)_2ZnCl_4$

$(NH_4)_2ZnCl_4$, herein after AZC, belongs to the A_2BX_4 crystal family. This family is the largest group of structurally incommensurate crystals. The structure is shown in Figure 6.1. Like many A_2BX_4 compounds AZC undergoes a sequence of phase transitions, including transitions from a normal (N) phase to an incommensurate (IC) phase to a commensurate (C) phase. The N-IC and IC-C transition temperatures at ambient pressure are $T_{IC} = 133^{o}C$ and $T_C = 91^{o}C$ respectively. Some other properties of AZC are summarized in table 6.1. There exists a local polarization that is modulated. This gives rise to a polarization wave incommensurate to the rest of the crystal. That is, it has a wave vector, q_{ic}, that is not a rational fraction of the reciprocal lattice vector and can be expressed as

$$\overline{q}_{ic} = (1-\sigma)\,\overline{q}_c \tag{6.1}$$

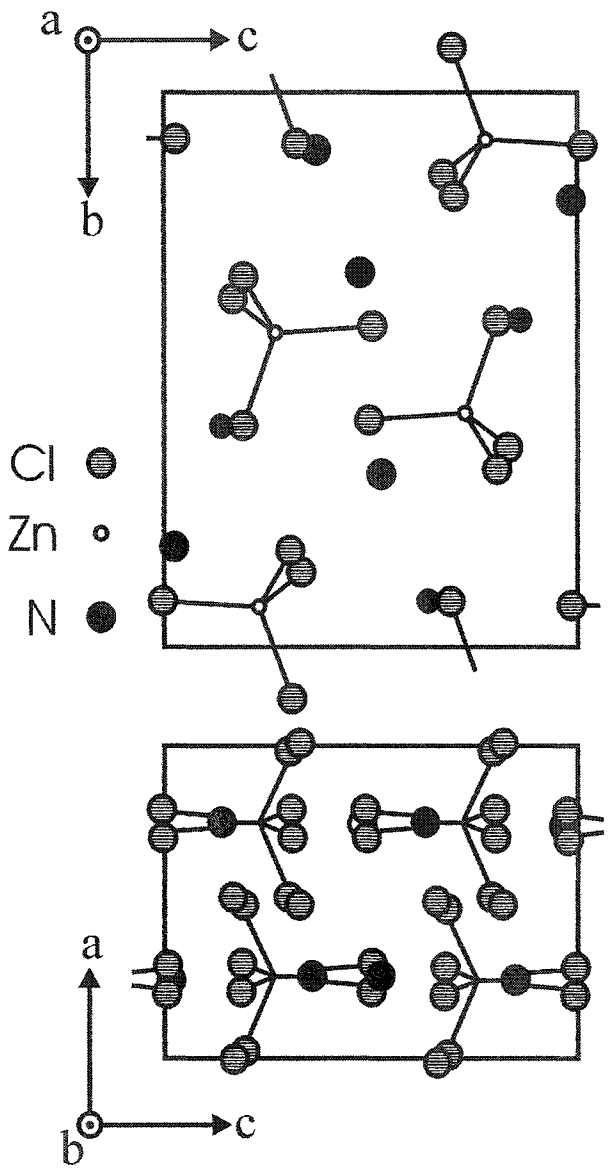

Figure 6.1: Structure of $(NH_4)_2 ZnCl_4$[61]

Phase I [58, 59]	Phase II [60]	Phase III [60, 61]	Phase IV	Phase V [62, 60]	Phase VI [61, 62]
above 133°C	91°C to 133°C	46°C to 91°C	3°C [60, 63] to 46°C	−5°C to 3°C	below −5°C
orthorhombic		orthorhombic	pseudo-orthorhombic, monoclinic [64]	coexistence of several commensurate modulated phases	orthorhombic
D_{2h}^{16} $(Pnma)$		C_{2v}^{9} $(Pn2_1a)$	C_s^2 (Pa) [61, 64]		C_{2v}^{9} $(Pn2_1a)$
normal	incommensurate	paraelectric	antiferroelectric [59]	weak ferroelectric	ferroelectric
$a_0 = 9.295$ $b_0 = 12.745$ $c_0 = 7.275$ at 145°C		$a = 37.116 \approx 4a_0$ $b = 12.661 \approx b_0$ $c = 7.236 \approx c_0$ at 60°C	$a = 37.096 \approx 4a_0$ $b = 12.620 \approx b_0$ $c = 7.211 \approx c_0$ $\gamma = 90.0^o$ at room temperature [61, 64, 62, 65]	$a = 4a_0, 3.5a_0$ $b = b_0$ $c = c_0$	$a = 27.837 \approx 3a_0$ $b = 12568 \approx b_0$ $c = 7.184 \approx c_0$ at −50°C

Table 6.1: Properties of $(NH_4)_2\,ZnCl_4$ at ambient pressure

with $\sigma \approx 0.008$ in the incommensurate phase [66] and $\sigma = 0$ in the commensurate phase; $\overline{q}_c = \overline{a}^*/4$ where $\overline{a}^*$ is the reciprocal lattice vector.

AZC shows anomalous elastic constants at ambient pressure at the N-IC and IC-C phase transitions, but discrepancies exist in the literature as to the nature of these anomalies [58, 67, 68, 66]. These discrepancies motivated a Brillouin scattering study of the effect of hydrostatic pressure on the elastic constant anomalies [69]. The elastic constants calculated from Brillouin scattering data depend directly on the density and indirectly on the density via the index of refraction. To allow for density corrections to the elastic constants, an energy dispersive x-ray diffraction study was performed in order to determine the equation of state of AZC. This study is discussed later in this chapter. Also discussed are calculations of the adiabatic bulk modulus, B_S, for AZC and for other materials of the A_2BX_4 family.

6.2 Determination of the Isothermal Equation of State

The isothermal equation of state of AZC has not been reported in the literature. In order to determine the equation of state, energy dispersive x-ray diffraction measurements were performed.

6.2.1 Experimental Details

Colorless crystals were obtained by seed growth from aqueous solution by slow cooling. High-pressure energy dispersive x-ray diffraction measurements of AZC were conducted at the Cornell High Energy Synchrotron Source as detailed in Chapter 4. NaCl was used as both the pressure transmitting medium as well as the pressure sensor as discussed in Chapter 2. The furnace used to reach temperatures up to 150^{o}C is described in Appendix B. A typical energy dispersive x-ray diffraction spectrum is shown in Figure 6.2.

At ambient pressure, two phase transitions occur above 46^{o}C as detailed in Table 6.1.

6.2.2 Lattice Constant Determination

Lattice parameters were determined, described in Chapter 4, for 80^{o}C, 100^{o}C and 150^{o}C up to about 4 GPa and are plotted in Figure 6.3. These temperatures were chosen in order to determine the equations of state within the normal orthorhombic phase, the incommensurate phase, and the commensurate orthorhombic phase.

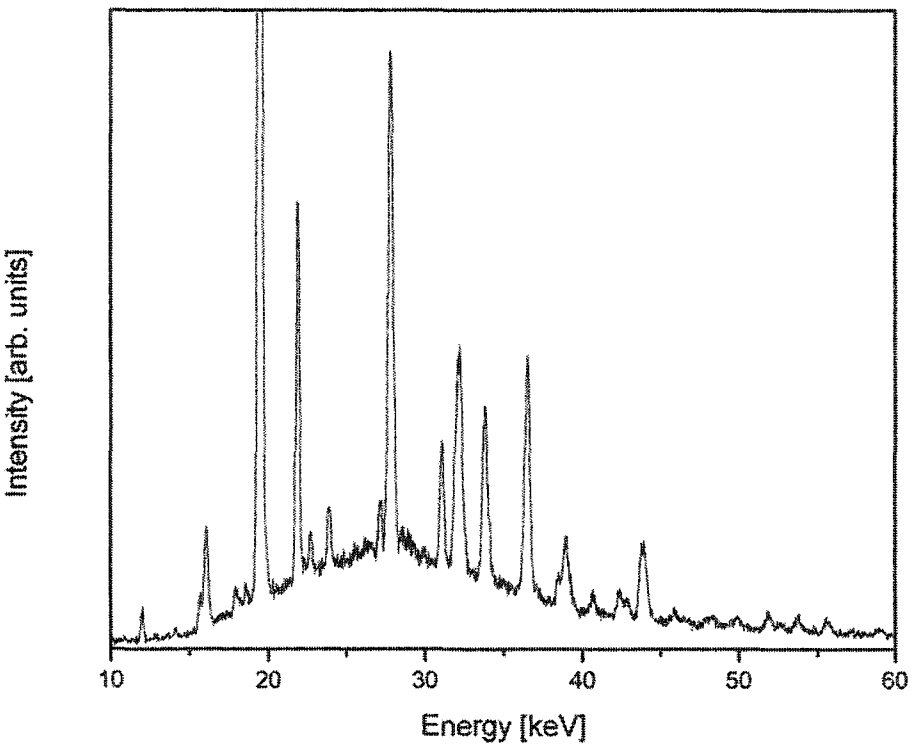

Figure 6.2: Typical EDXD graph of $(NH_4)_2 ZnCl_4$

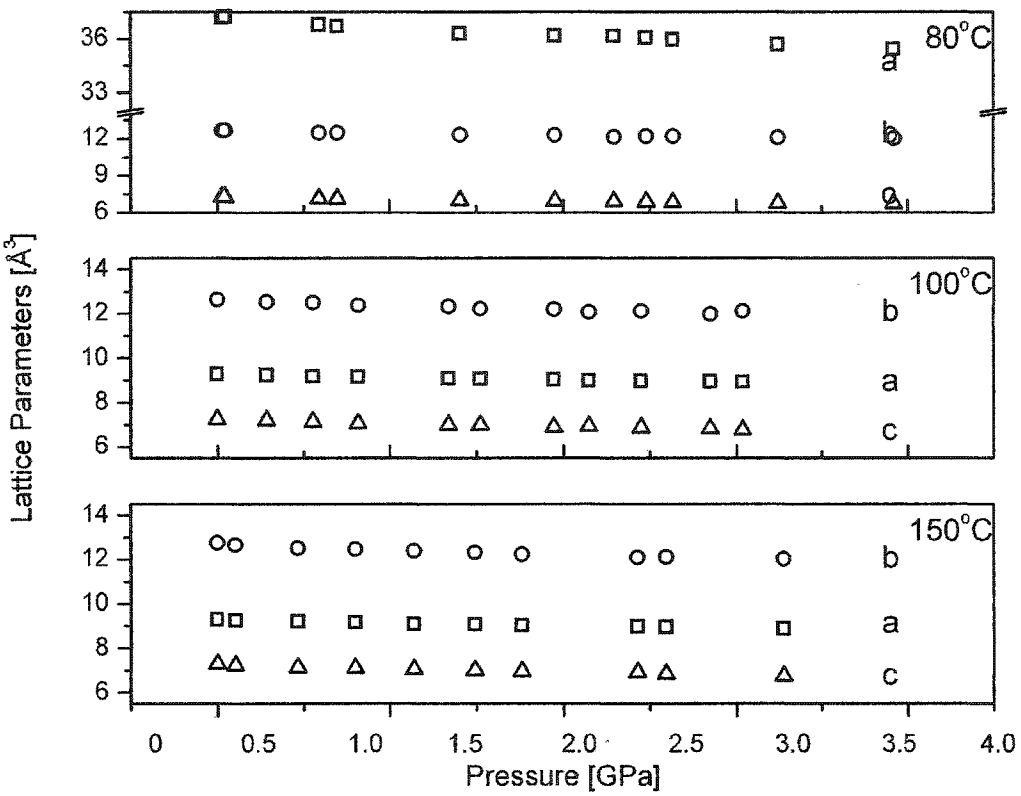

Figure 6.3: Lattice constants

Temperature (°C)	B_T (GPa)	B'_T
80	12.1 ± 0.8	6.2 ± 0.8
100	11.0 ± 0.4	6.6 ± 0.5
150	8.1 ± 1.0	8.2 ± 1.5

Table 6.2: Isothermal bulk modulus of $(NH_4)_2\,ZnCl_4$ and its derivative.

6.2.3 Murnaghan Equation of State

For each of the three temperatures, the pressure dependence of the unit cell volume was determined by fitting the data to the Murnaghan [70] equation of state

$$\frac{V}{V_0} = \left(1 + \frac{B'_T}{B_T}P\right)^{\frac{-1}{B'_T}} \tag{6.2}$$

The fit was performed using ORIGIN [71] and both the original data and the fit are shown in Figure 6.4. The values for the isothermal bulk modulus,

$$B_T = -\left(V\frac{dp}{dV}\right)_{p=0} \tag{6.3}$$

and its derivative

$$B'_T = -\frac{d}{dp}\left(V\frac{dp}{dV}\right)_{p=0} \tag{6.4}$$

were determined and are listed in Table 6.2.

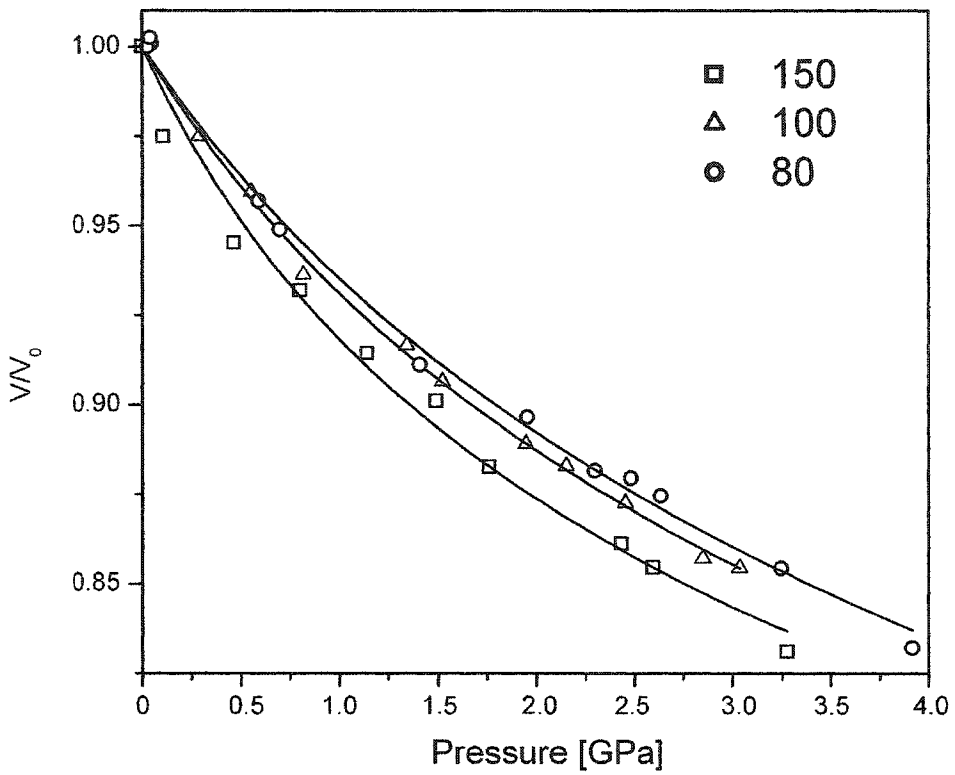

Figure 6.4: V/V_0 versus Pressure of$(NH_4)_2 ZnCl_4$.

6.2.4 Pressure Dependence of Density and Index of Refraction

The elastic constants calculated from Brillouin scattering data depends directly on the density and indirectly on the index of refraction. The density changes as

$$\frac{\Delta\rho}{\rho} = \left(1 + \frac{B'_T}{B_T}P\right)^{\frac{-1}{B'_T}} - 1 \tag{6.5}$$

and the index of refraction changes as

$$\frac{\Delta n}{n} = \frac{\Delta\rho}{\rho}\frac{(n^2-1)(n^2+2)}{6n^2} \tag{6.6}$$

The Brillouin study reached pressures of about 0.7 GPa [69]. Within this pressure range, the density and index of refraction change by about 5% and 4% respectively. The density is plotted in this pressure range in Figure 6.5 and for the entire pressure range to 4 GPa in Figure 6.6 .

6.3 Calculations of Adiabatic Bulk Moduli

The calculated adiabatic bulk modulus (B_S) of AZC had not been reported in the literature. Using previously published [58, 68, 67] experimental values of the elastic constants, values of B_S have been calculated.

6.3.1 Elastic Constant Data

Values of elastic constants published in the literature are compiled in Table 6.3. Values of all elastic constants except C_{12} have been extrapolated directly from data plots in the literature [58, 67] using UN-SCAN-IT [72]. Values of C_{12} were calculated using data

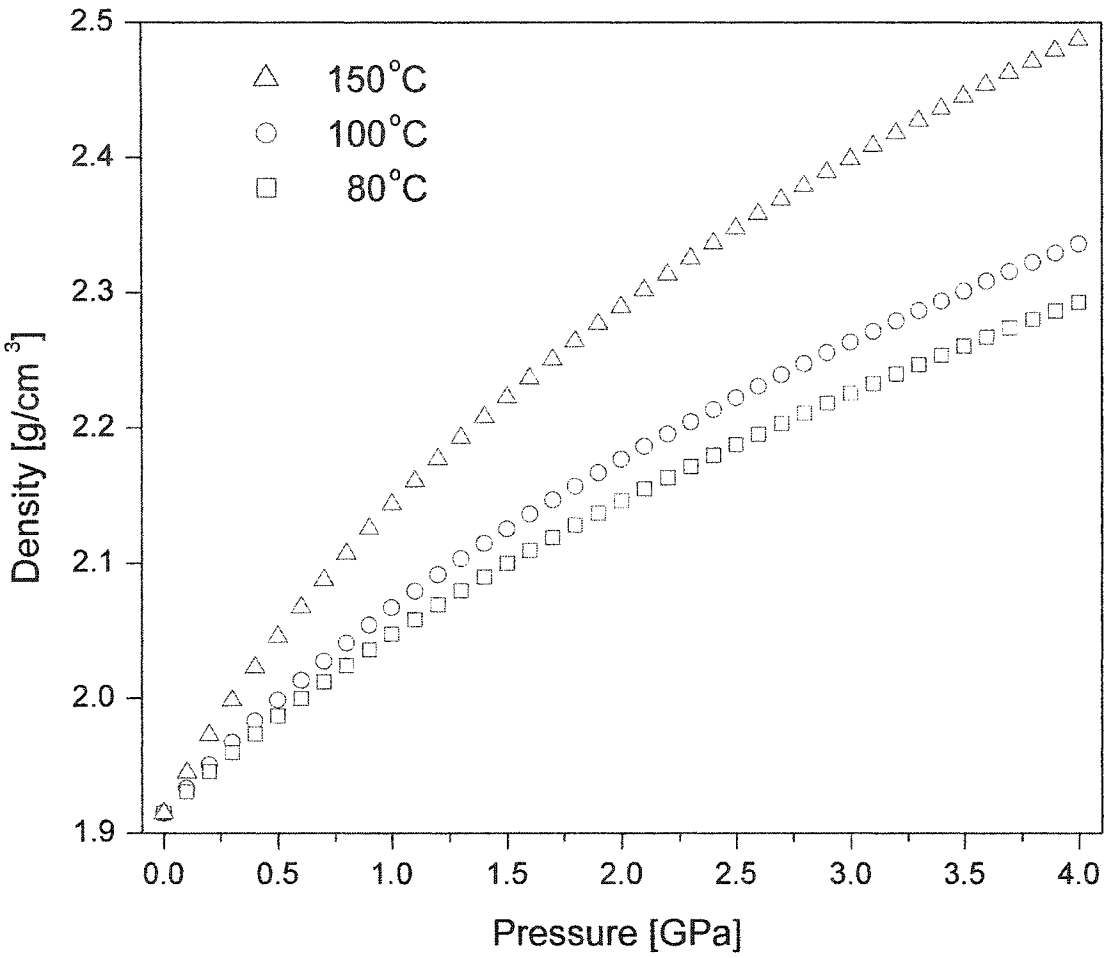

Figure 6.5: Dependence of index of refraction on pressure of$(NH_4)_2\,ZnCl_4$ up tp about 4 GPa.

Temperature	C_{11}^*	C_{22}^*	C_{33}^*	C_{44}^*	C_{55}^*	C_{66} [67]	C_{12} [68]	C_{13} [58]	C_{23} [58]
(^{o}C)	(GPa)	(GPa)	(GPa)	(GPa)	(GPa)	(GPa)	(GPa)	(GPa)	(GPa)
80	21.4	19.6	17.4	3.4	5.0	4.9	10.2	8.9	8.4
100	21.0	19.5	17.4	3.2	5.0	4.9	9.9	8.7	8.2
150	20.4	18.3	17.5	3.0	2.8	2.9	9.4	8.4	7.6

Table 6.3: Previously published values of the elastic constants of $(NH_4)_2\,ZnCl_4$
* average values [58] and [67]

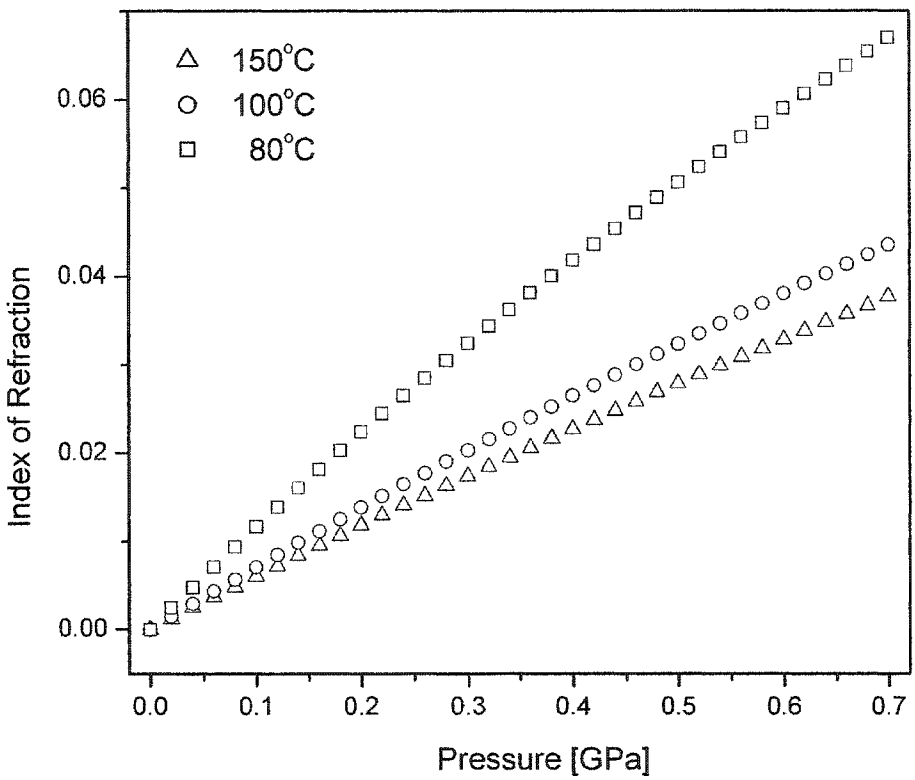

Figure 6.6: Density dependence on pressure of $(NH_4)_2 ZnCl_4$ up to about 0.7 GPa.

extrapolated from a plot [68] of

$$\left(C_{11}+C_{22}+2C_{66}\right)/4+\left[\left(C_{11}-C_{22}\right)^{2}+4\left(C_{12}+C_{66}\right)^{2}\right]^{1/2}/4 \tag{6.7}$$

and other elastic constants listed in Table 6.3

6.3.2 Calculation Details

For the orthorhombic structure, B_S is related to the adiabatic compressibility, K_s, by

$$B_S = 1/K_S \tag{6.8}$$

where K_S is related to the elastic compliance constants, S_{ij}, by

$$K_S = S_{11}+S_{22}+S_{33}+2\left(S_{12}+S_{23}+S_{31}\right) \tag{6.9}$$

and

$$\begin{pmatrix} S_{11} & S_{12} & S_{31} & 0 & 0 & 0 \\ S_{12} & S_{22} & S_{23} & 0 & 0 & 0 \\ S_{31} & S_{23} & S_{33} & 0 & 0 & 0 \\ 0 & 0 & 0 & S_{44} & 0 & 0 \\ 0 & 0 & 0 & 0 & S_{55} & 0 \\ 0 & 0 & 0 & 0 & 0 & S_{66} \end{pmatrix} \begin{pmatrix} C_{11} & C_{12} & C_{31} & 0 & 0 & 0 \\ C_{12} & C_{22} & C_{23} & 0 & 0 & 0 \\ C_{31} & C_{23} & C_{33} & 0 & 0 & 0 \\ 0 & 0 & 0 & C_{44} & 0 & 0 \\ 0 & 0 & 0 & 0 & C_{55} & 0 \\ 0 & 0 & 0 & 0 & 0 & C_{66} \end{pmatrix} = \bar{I} \tag{6.10}$$

We obtain the following relation for the adiabatic bulk modulus and the elastic constants:

$$B_S = \frac{C_{11}C_{22}C_{33} + 2C_{12}C_{23}C_{13} - C_{13}^2C_{22} - C_{23}^2C_{11} - C_{12}^2C_{33}}{C_{11}C_{22} + C_{22}C_{33} + C_{11}C_{33} - C_{12}^2 - C_{23}^2 - C_{13}^2 + A} \tag{6.11}$$

with

$$A = 2\left(C_{12}C_{13} + C_{12}C_{23} + C_{13}C_{23} - C_{11}C_{23} - C_{22}C_{13} + C_{33}C_{12}\right) \tag{6.12}$$

6.4 Discussion

B_T was determined as described in Section 6.2. B_S was calculated from the elastic constants listed in Table 6.3.

B_S and B_T are related by [73]

$$B_S = B_T\left(1 + \Delta\right) \tag{6.13}$$

with

$$\Delta = \frac{9\alpha^2 T B_S}{\rho c_p} \tag{6.14}$$

where α is the linear thermal expansion coefficient and c_p the specific heat at constant pressure.

As Δ is positive we would expect $B_T < B_S$. At 80°C our experimentally determined values for B_T and B_S are equal within errors as seen in Table 6.5. This may reflect a large error in the calculated values for B_S, due to error propagation of the elastic constants used to calculate B_S. Unfortunately the error was not reported for the majority of the elastic constants in Table 6.3. A 2% error was reported [67] for C_{11}, C_{22}, and C_{33}. Using these available errors a minimum error of about 10% can be calculated for B_S for each of the

	Temperature	C_{11}	C_{22}	C_{33}	C_{44}	C_{55}	C_{66}	C_{12}	C_{13}	C_{23}
	(°C)	(GPa)	(GPa)	(GPa)	(GPa)	(GPa)	(GPa)	(GPa)	(GPa)	(GPa)
Rb_2ZnBr_4	27 [74]	22.6	17.5	17.1	4.7	5.1	3.4	7.9	8.7	8.3
Rb_2ZnCl_4	27[74]	28.2	21.0	19.3	6.1	6.2	3.7	8.5	9.2	9.4
	27 [75]	28.4	21	19.3	6.2	6.3	3.6	9.6	10.1	9.7
$(NH_4)_2BeF_4$	17 [76]	33.3	23.8	31.8	8.6	6.7	8.7	13.2	16.0	12.3
	-91[76]	39.6	22.5	33.9	10.0	5.5	10.0	13.8	17.1	11.2

Table 6.4: Elastic constants for various A_2BX_4 family materials.

	Temperature	B_S	B_T
	(°C)	(GPa)	(GPa)
$(NH_4)_2ZnCl_4$	80 [69]	12.4	12.1 ± 0.8
	100 [69]	12.3	11.0 ± 0.4
	150 [69]	11.8	8.1 ± 1.0
Rb_2ZnBr_4	27 [74]	11.7	
Rb_2ZnCl_4	27[74]	13.8	
	27 [75]	13.4	
	40 [77]		20.8 ± 0.5
	-95 [77]		17.9 ± 0.5
$(NH_4)_2BeF_4$	25 [78]		20.9 ± 0.9
	17 [76]	18.4	
	-91[76]	18.2	

Table 6.5: Isothermal and adiabatic bulk moduli for various A_2BX_4 family materials.

three temperatures. However a more accurate determination of the error is impossible due to unreported error in the other elastic constants. There seems to be reasonable agreement in the magnitude of these values and it is reasonable to assume that $B_T < B_S$.

Values of the elastic constants (Table 6.4) and values of B_S and B_T (Table 6.5) are compiled for various materials of the A_2BX_4 family, including Rb_2ZnCl_4, Rb_2ZnBr_4, and $(NH_4)_2BeF_4$.

Chapter 7

High-Pressure Survey of Cs_2MoS_4

Dicaesium tetrathimolybdate, Cs_2MoS_4, has been successfully synthesized [79]. Previous room-temperature high-pressure measurements on the material revealed a series of structural phase transitions and a possible direct to indirect band crossing [8, 9]. The scope of this chapter will be to concentrate on low-temperature high-pressure Raman measurements.

7.1 Transition Metal Chalcogenides

Transition metal chalcogenides have many interesting properties and industrial applications. Many metal dichalcogenides are layered compounds with highly anisotropic properties [80]. Other interesting properties include charge density wave transitions and superconductivity.

Chalcogenides

A chalcogenide is any compound with anions belonging to the chalcogens. Chalcogens consist of elements from group seven of the periodic table including oxygen, sulfur, se-

lenium and tellurium. Chalcogenide glasses are of interest for technological applications such as infrared transmission (Ge-S), switching circuits (As_2Te_3), sonic glasses (Ge-As-S), and optical memory (Ge-Te) [6, 5].

Transition Metals

A transition metal (*d*-block element) is any element in groups three to 12 of the periodic table. The *d*-block elements have several unique properties of interest to materials science. Because their valence electrons occupy more than one shell, they have a variety of oxidation states allowing for many different complexes. Transition metals are also used in redox reactions since than can both give and receive an electron. As with the *f*-block elements, the transition metals can form organometallic compounds and have the ability to participate in catalysis and biochemical processes.

Molybdenum Sulfides

Transition-metal sulfides have been used for almost 80 years in industrial hydrosulfurization, the removal of sulfur from petroleum-based feedstocks [2]. In particular the unusual redox chemistry of Cr, Mo, and W, sulfides aid in the ability of these materials as a catalyst. Of particular interest here are the molybdenum sulfides.

Molybdenum sulfides encompass a wide range of interests and applications [81, 82, 83, 84, 85, 86, 87, 88]. More molybdenum sulfide compounds exist than any other transition-metal sulfide [85]. Chevrel-phase compounds are a relatively large group of superconductors with the general chemical formula $M_xMo_6S_8$ [89].

Molybdenum disulfide, MoS_2, is a semiconductor with interesting industrial, optical, and electronic applications [90]. It is used as a lubricant additive, acts as a cathode in

lithium nonaqueous batteries, and is used in hydrodesulfurization [2]. MoS_2 forms several polytypes, a variety of oxidation states, and can form complexes and organometallic compounds [91].

Studies on divalent molybdates show pressure induced phase transition in $SrMoO_4$ [92], $CaMoO_4$ [93], and $CdMoO_4$[94]. Pressure induced amorphization has been reported in the trimolybdate compounds $Tb_2(MoO_4)_3$ [95] and $Gd_2(MoO_4)_3$ [96] at moderate pressures of ~6 GPa. A pressure induced electronic transition in $KTb(MoO_4)_2$ [97] has been observed. This material is discussed in more detail in Chapter 8 as it relates to the pressure induced electronic transition observed in $KTbP_2Se_6$[10, 11, 12].

7.1.1 Cs_2MoS_4

Cesium is an *s*-block alkali metal with a characteristic +1 oxidation state. Like AZC, discussed in the Chapter 6, Cs_2MoS_4 belongs to the A_2BX_4 family of compounds which are isostructural with $\beta - K_2SO_4$ [98]. Previous room temperature studies of Cs_2MoS_4 indicate an orthorhombic low pressure phase I [79] at ambient pressure.

Also reported are two high pressure phases with a very small transition region; phase II from 8.0 to 9.7 GPa is monoclinic and phase III above 9.7 GPa is orthorhombic. Some of the room temperature properties of this material are summarized in table 8.1.

At ambient conditions Cs_2MoS_4 is a semiconductor with a direct band gap. Some properties of semiconductors are discussed in Chapter 4.2. A possible direct to indirect bandcrossing exists with increasing pressure, and excitonic levels exist within the band gap [8, 9].

Phase I [79]	Phase II [9, 8]	Phase III [9, 8]
below 8 GPa	8 to 9.7 GPa	above 9.7 GPa
orthorhombic	monoclinic	orthorhombic
$Pnma$ (D_{2h}^{16}; No. 62)	$P2_1/c$ (C_{2h}^{5}; No. 14) suggested; based on descent in symmetry	not reported
$a = 10.048$ $b = 7.246$ $c = 12.783$ at ambient pressure	$a = 14.061$ $b = 11.552$ $c = 9.852$ $\beta = 97.14^{\mathrm{O}}$ at 7.8 ± 0.5 GPa	$a = 12.085$ $b = 15.707$ $c = 11.828$ at 12.5 ± 0.5 GPa

Table 7.1: Room temperature properties of Cs_2MoS_4.

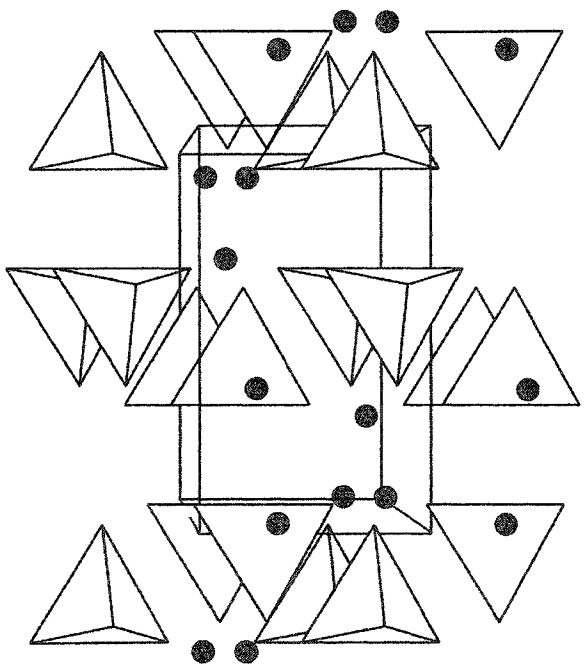

Figure 7.1: Bravais Cell of Cs_2MoS_4. View is along the x axis of the orthorhombic cell. [9].

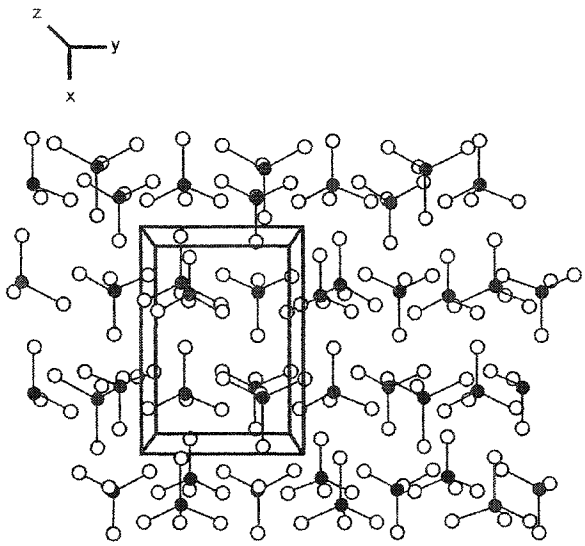

Figure 7.2: Top view of the *x*-*y* plane in the low-pressure orthorhombic phase I of Cs_2MoS_4 [9] Cs-ions are not shown for clarity.

7.1.1.1 Structure [79, 9]

At ambient temperature the low pressure phase I (see Figure 7.1) is built up by $[MoS_4]^{2-}$ tetrahedral clusters and Cs^+ ions forming an orthorhombic lattice with four formula units in the Bravais cell. The $[MoS_4]^{2-}$ ions have T_d symmetry and the Cs have C_s site symmetry. Cs_2MoS_4 belongs to the D_{2h}^{16} (*Pnma*) space group.

During the transition from phase I to phase II, the *x* and *z* axis (See Figure 7.2) become the *z*' and *y*' axis respectively and the *y* axis doubles and becomes the *x*' axis (See Figure 7.3). Phase II is layered in the *y*'-*z*' plane as seen in Figure 7.4. This layering is due to a denser packing at higher pressure accompanied by a change in the coordination number from four to six.

Phase II is monoclinic. Lorenz et al. suggested the space group $P2_1/c$ based on descent in symmetry [9]. This suggestion is inferred from data of other A_2BX_4 compounds with monoclinic high-pressure phases. In particular, $BaWO_4$ has a monoclinic high-pressure

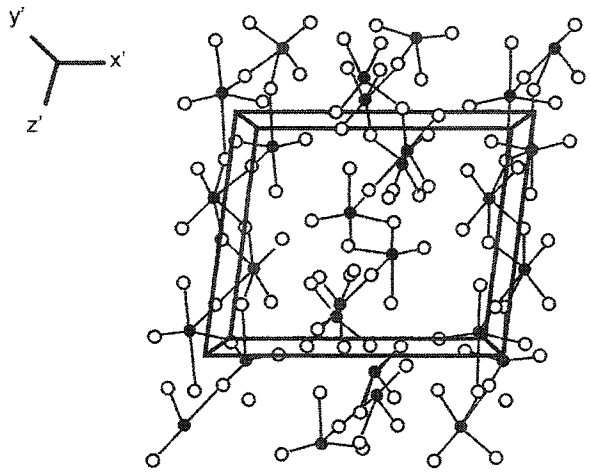

Figure 7.3: Top view of the x'-z' plane in the monoclinic high-pressure phase II of Cs_2MoS_4 [9] Cs-ions are not shown for clarity.

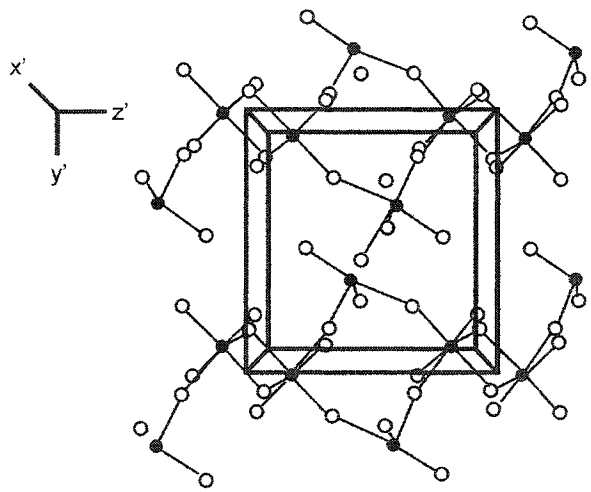

Figure 7.4: Layered structure in the y'-z' plane of the monoclinic high-pressure phase II of Cs_2MoS_4 [9]. Cs-ions are not shown for clarity.

phase with space group $P2_1/n$, a nonstandard setting of $P2_1/c$ [99]. Phase III is orthorhombic however the space group is not reported in the literature.

7.1.1.2 Vibrational Properties at Room Temperature

Room temperature Raman studies of Cs_2MoS_4 reveal well separated internal modes of the strongly bonded $(MoS_4)^{2-}$ molecule as well as external lattice vibrations below $100\,cm^{-1}$ [8]. The internal modes include up to five lines in a band around $472\,cm^{-1}$ and up to four lines in a band around $180\,cm^{-1}$.

7.1.1.3 Phase Transitions

At room temperature, the transition from phase I to phase II at 8 GPa is driven by a soft phonon mode [8, 9]. This is evident because of the decrease in frequency with increasing pressure of the $MoO_4^{2-} - MoO_4^{2-}$ external stretching mode that vanishes at the phase transition. The transition from phase II to phase III is indicated by the appearance of a low frequency, strongly pressure-dependent mode and by the splitting of other low frequency phonons. This splitting is evidence of a lower symmetry structure in phase III. Both phase transitions occur with no measurable hysteresis which may indicate second-order phase transitions. However a first-order phase transition with small transition enthalpy is also possible. At high temperatures to 250^oC the phase diagram has been determined and is plotted in Figure 7.6.

7.1.1.4 Electronic Properties at Room Temperature

Absorption and luminescence data at room temperature indicate that a band crossing may occur with increasing pressure [9]. Absorption data is plotted in Figure 7.7. At ambient

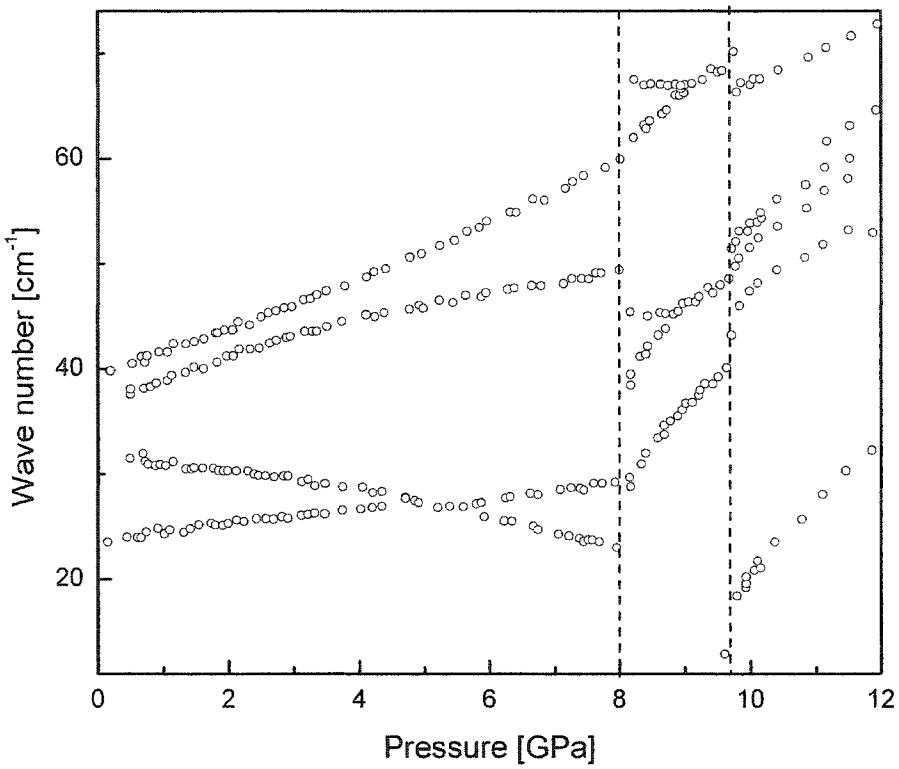

Figure 7.5: Pressure dependence of the low frequency external modes of Cs_2MoS_4. The two phase transition pressures are indicated by dotted lines [8].

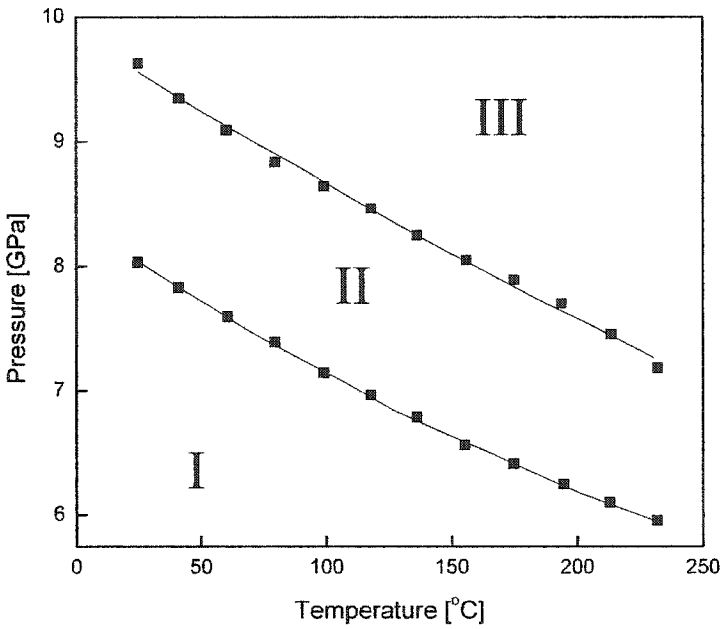

Figure 7.6: Phase diagram of Cs_2MoS_4 [9].

pressure the absorption edge is about $2.1eV$. As pressure is increased the absorption edge energy increases until about 3.5 GPa. At this pressure the edge energy begins to decrease with increasing pressure. The edge energy in phase I can be described by the quadratic equation

$$E(\text{eV}) = a_0 + a_1 P + a_2 P^2 \tag{7.1}$$

where P is in GPa with $a_0 = 2.132(1)$ eV, $a_1 = 0.0155(7)$ eV/GPa, and $a_2 = -0.0021(1)$ eV/GPa^2. The change of sign of dE/dP indicates a possible band crossing. A jump in edge energy occurs at both phase transitions. At the transition from phase I to phase II, the edge energy jumps from about 2.12 meV to 2.07 meV, a difference of about 50 meV. In phase II the absorption edge decreases linearly with pressure. At the transition from phase II to phase III another discontinuity in the absorption edge occurs as shown in Figure 7.7.

Luminescence measurements also support a band crossing. At ambient conditions the luminescence peak maximum is at 2.46 eV, 0.3 eV higher than the absorption edge, indicating an excitonic state below the conduction band. Up to about 3 GPa, the luminescence maximum shifts about 30 meV to higher energy with increasing pressure. This is indicative of an opening of the direct band gap at the Γ point of the Brillouin zone. Also of interest is the luminescence intensity which decreases with increasing pressure up to 3 GPa. This decrease suggests a direct to indirect crossing.

Lorenz et al. have proposed a qualitative scheme to explain the effect of pressure on the electronic excitation spectrum. This description is represented schematically in Figure 7.8. At ambient pressure, an excitonic level exists at about 0.3 eV below the conduction band at the Γ point of the Brillouin zone. At least one more local minimum exists, forming an indirect gap most likely at the Brillouin zone boundary. As pressure increases the direct gap broadens and the indirect gap narrows causing the crossing.

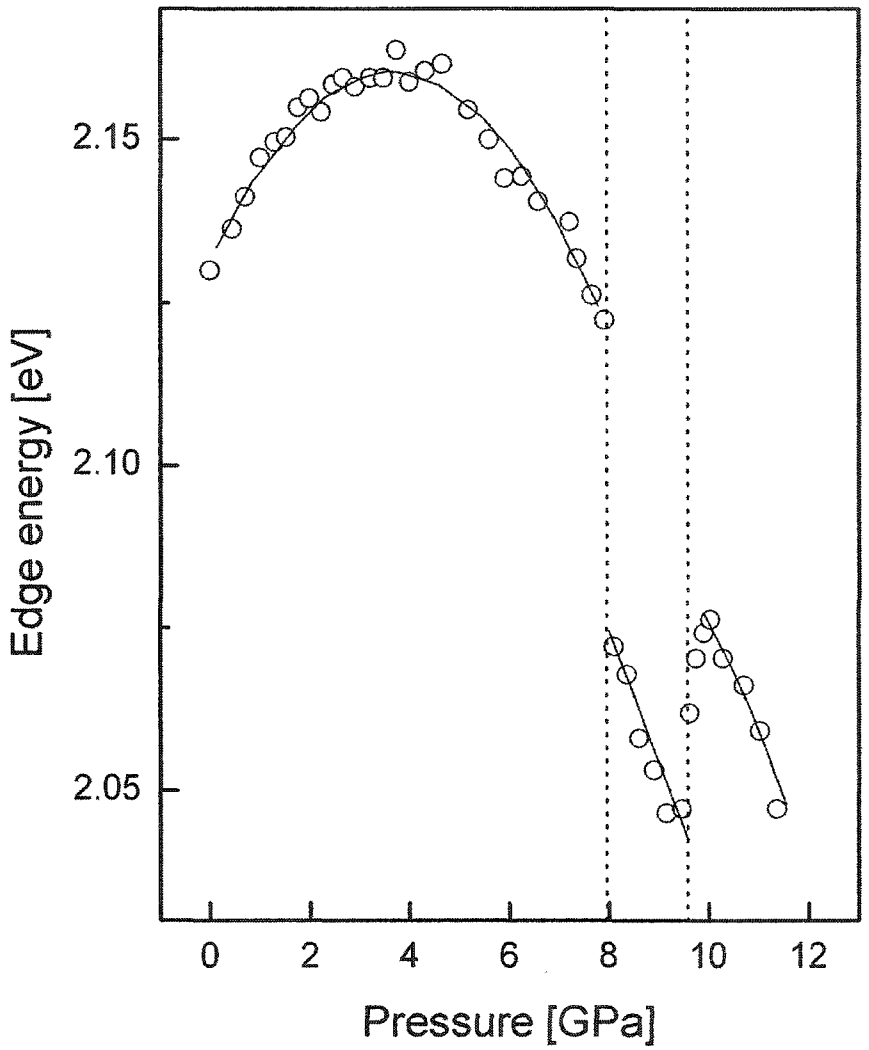

Figure 7.7: Pressure dependence of the absorption edge of Cs_2MoS_4[9].

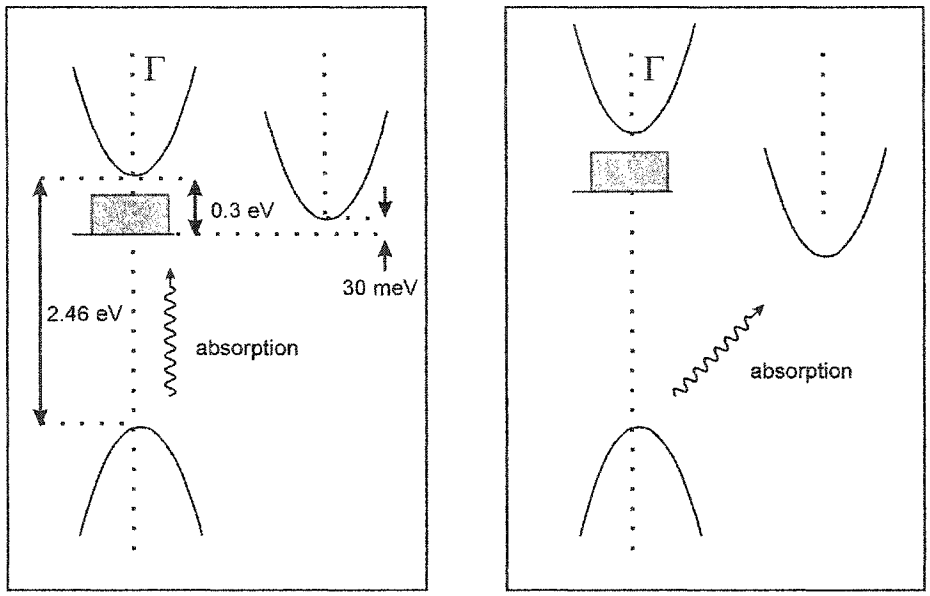

Figure 7.8: Schematic band structure diagram compiling the results of the absorption and luminescence measurements of Cs_2MoS_4 [9].

7.2 Room Temperature Raman Measurements

Room temperature Raman scattering measurements have been reported by Lorenz et al. [9]. New room temperature Raman measurements are reported in this thesis for comparison to previously published data. Measurements reported herein match well with previously reported data, although data reported previously was taken with a triple spectrometer allowing for better resolution as can be seen in Figures 7.9 and 7.10.

7.3 Low Temperature Measurements

No low temperature measurements have been reported in the literature. In order to determine the phase transitions at low temperature, high-pressure Raman measurements were performed.

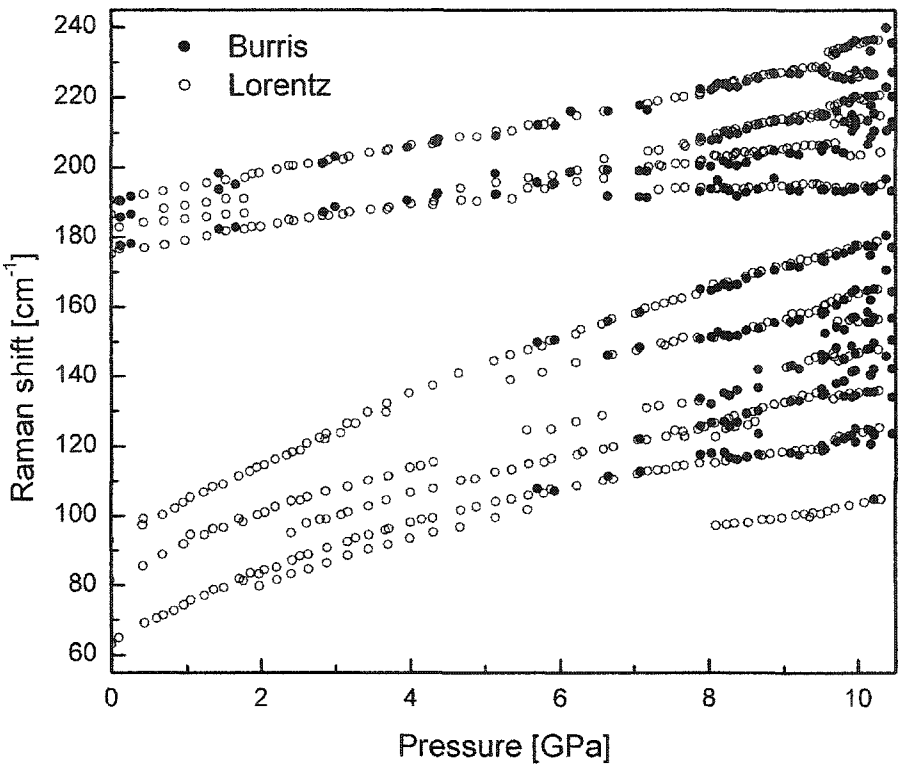

Figure 7.9: New and previously published [9] room temperature Raman measurements at low frequencies of Cs_2MoS_4.

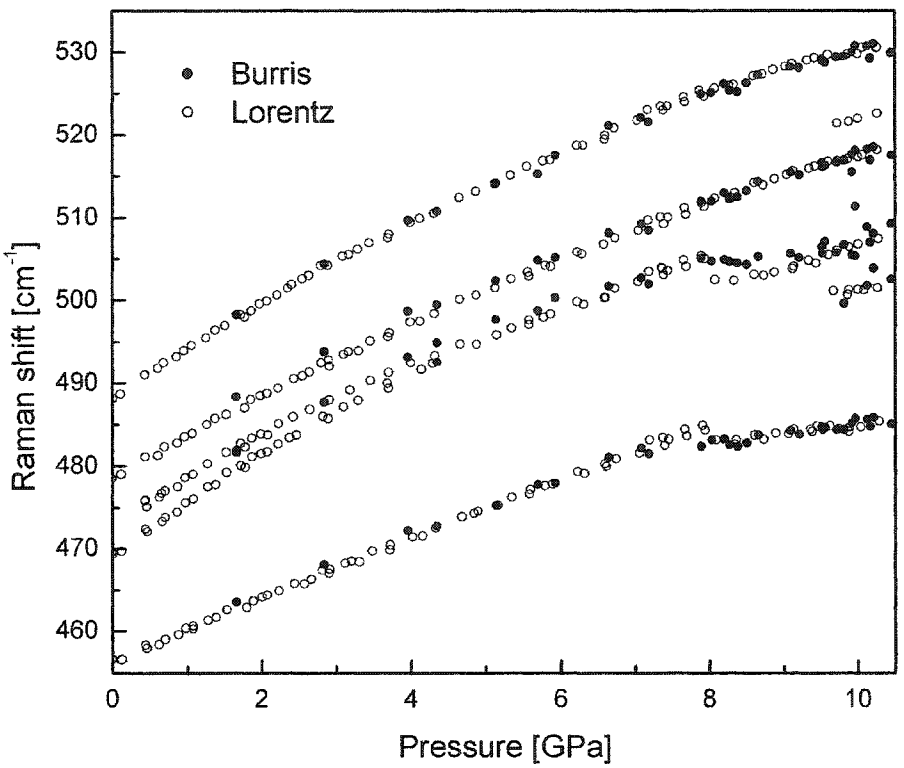

Figure 7.10: New and previously published [9] room temperature Raman measurements at higher frequencies of Cs_2MoS_4.

7.3.1 Experimental Details

Orange crystalline needles of Cs_2MoS_4 were provided by the Dorhout inorganic chemistry group at Colorado State University. The crystals were prepared by a hydrothermal reaction of molybdenum powder with K_2S_6 and K_2Se_4 (a sacrificial oxidant) in 50 μL of a 1.0 M cesium acetate solution [79]. High-pressure optical and energy dispersive x-ray diffraction measurements were performed as described in Chapter 4. As detailed in Chapter 2, argon or a methanol ethanol mixture was used as the pressure transmitting medium for optical measurements while ruby was the pressure sensor. NaCl was used as both the pressure transmitting medium and the pressure sensor for x-ray measurements and is discussed in Chapter 2. The low temperature apparatus is described in appendix B.

7.3.2 Raman and Luminescence

Raman measurements at 77 K show the occurrence of two phase transitions at 8.1 GPa and 9.1 GPa as can be seen in Figures 7.11 and 7.12.

At room temperatures luminescence intensity decreases drastically with increasing pressure, disappearing altogether at about 3 GPa [9]. At low temperatures no luminescence intensity was observed at any pressure.

7.4 Discussion and Future Work

Low temperature Raman measurements were performed on Cs_2MoS_4. These measurements reveal two phase transitions at 8.1 GPa and 9.1 GPa. Low temperature luminescence measurements revealed no luminescence intensity.

It may be possible to perform low temperature luminescence measurements with a di-

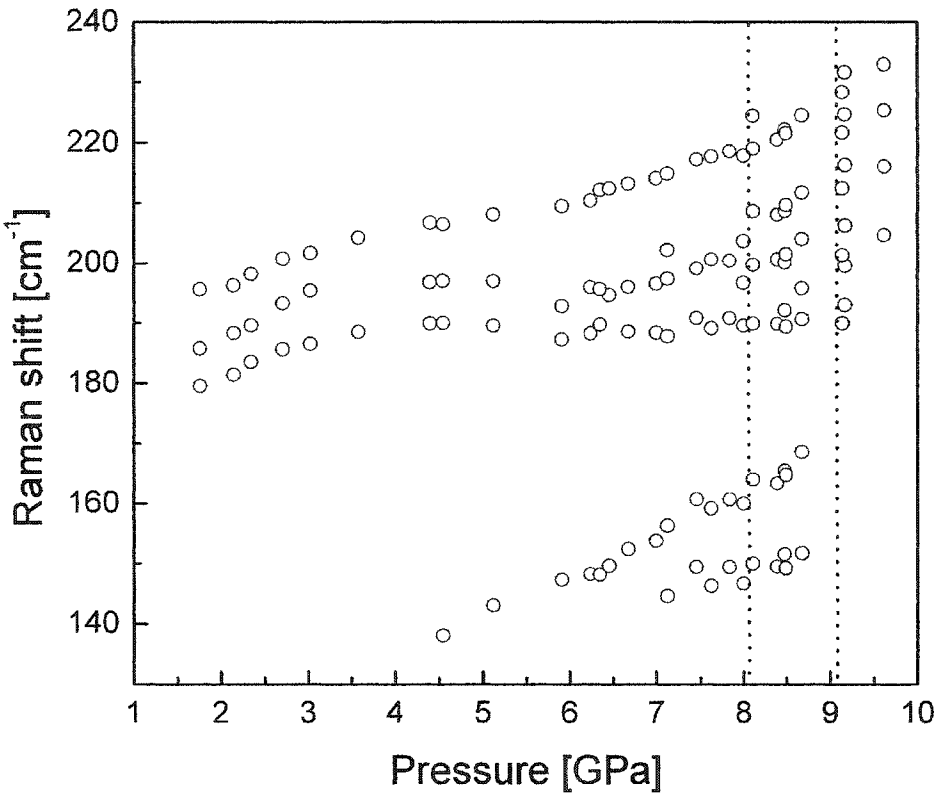

Figure 7.11: Raman measurements at low frequencies at 77 K of Cs_2MoS_4.

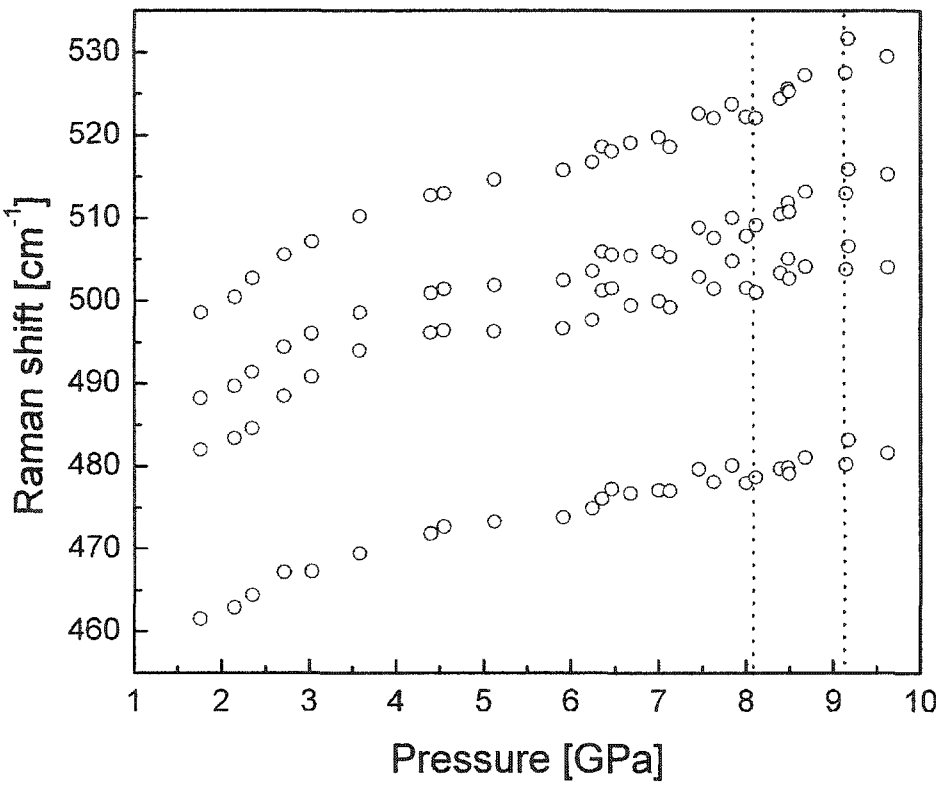

Figure 7.12: Raman measurements at higher frequencies at 77 K of Cs_2MoS_4.

amond anvil cell equipped with 1mm tip diamond anvils. Larger tipped diamond anvils are necessary to take quality measurements in the lower pressure range from 0 to 3 GPa. The 1mm tip diamond anvils require a thinner diamond anvil to allow for sapphire backing plates necessary for diamond stability. The design of the diamond anvil cell discussed in Chapter 2 does not allow for larger tip diamonds to be used due to the narrow width of the cell design. With implementation of a new objective lens, with a longer working distance, another diamond anvil cell can be made with the exact design of the cell discussed in Chapter 2 save for a greater width. Low temperature absorption measurements would also be of interest for this material and will be possible with perfection of the absorption system as described in Chapter 2.

Chapter 8

High-Pressure Survey of $KTbP_2Se_6$

Potassium terbium selenodiphosphate, $KTbP_2Se_6$, is one of several lanthanide selenodiphosphates that have been successfully synthesized [100, 10]. Previous room-temperature high-pressure measurements on the material revealed a pressure induced electronic transition caused by a $4f$-$5d$ charge transfer model [10, 11, 12]. The scope of this chapter will be to present low-temperature high-pressure Raman measurements.

8.1 Rare-Earth Metal Chalcogenides

Rare-earth metal chalcogenides have many interesting properties and are an emerging class of new optical materials [10, and references therein]. Any compound with oxygen, sulfur, selenium, or tellurium anions is classified as a chalcogenide. The importance of chalcogenides are discussed in Chapter 7.

Rare-Earth Metals

Elements of period six, the Lanthanide series, are also called rare-earth elements. Their oxides (earths) were once thought to be rare, but the rarest is more abundant than silver [91]. The first appearance of the f orbitals in the ground state configuration occur in these elements. The lanthanides are unique in that their chemical properties are highly uniform because that they all have three valence electrons. Rare-earth elements are important for fluorescent lamps, solid-state lighting, medical imaging, as phosphor elements, and are also essential in separation chemistry [101].

KTb $(MoO_4)_2$

Pressure-induced phase transitions have been observed in divalent molybdates [92, 93, 94]. Jayaraman et al. have reported pressure-induced amorphization in Tb and Gd trimolybdates at a moderate pressure of 6 GPa [95, 96]. They have also found a pressure induced electronic transition in KTb $(MoO_4)_2$ near 2.7 GPa that was accompanied by a change in color from colorless to yellow and a contraction in the a-axis direction [97]. Structural transitions are common in the layered-type potassium rare-earth molybdate, KRE $(MoO_4)_2$, systems but the electronic transition is unique to KTb $(MoO_4)_2$. This interesting transition in KTb $(MoO_4)_2$ led to a study of potassium terbium hexaseleneodiphosphate, $KTbP_2Se_6$.

8.1.1 $KTbP_2Se_6$

Previous room temperature studies of $KTbP_2Se_6$ indicate an orthorhombic low pressure phase I below 9.2 GPa and an orthorhombic high pressure phase II above 9.2 GPa [10]. Some of the room temperature properties of this material are summarized in table 8.1.

At ambient conditions $KTbP_2Se_6$ is a semiconductor with a band gap of 2.68 eV. A

Phase I	Phase II
below 9.2 GPa	above 9.2 GPa
orthorhombic	orthorhombic
$P2_12_12_1$ (D_2^4; No. 19)	
$a = 6.741$ $b = 7.450$ $c = 21.578$ at ambient pressure	$a = 6.486$ $b = 14.137$ $c = 19.600$ at $9.2 \pm GPa$

Table 8.1: Room temperature properties of $KTbP_2Se_6$ [10].

pressure induced electronic transition occurs in conjunction with the structural phase transition. This electronic transition includes a 0.5 eV discontinuity of the absorption edge into the red causing an immediate change in color from light yellow to red.

8.1.1.1 Structure

At ambient pressure, the low pressure phase I is a layered structure built up of selenodiphosphate (IV), $(P_2Se_6)^{4-}$, units. All Se atoms except one are bound to a Tb atom. The remaining Se atom from each unit is bound only to a P and sticks out into the interlayer spacing of the crystal. Each of the Se atoms not bound to a Tb is coordinated to four K cations [100].

X-ray diffraction experiments reveal a contraction in both the a and c axes at the phase transition; however, the b-axis doubles. This doubling occurs due to newly formed Se-Se bonds connecting two of the selenodiphosphate (IV) units across the layer. The Se-Se bonding is between two of the Se atoms which were sticking into the interlayer spacing in phase I. The building blocks of the crystal, previously $\left\{\left(P^{4+}\right)_2\left(Se^{2-}\right)_6\right\}^{4-}$ are now $\left(\left\{\left(P^{3+}\right)_2\left(Se^{2-}\right)_4\left(Se_2\right)^{2-}\right\}^{4-}\right)_2$ [10]. The structure changes from a 2-D layered material into a 3-D material.

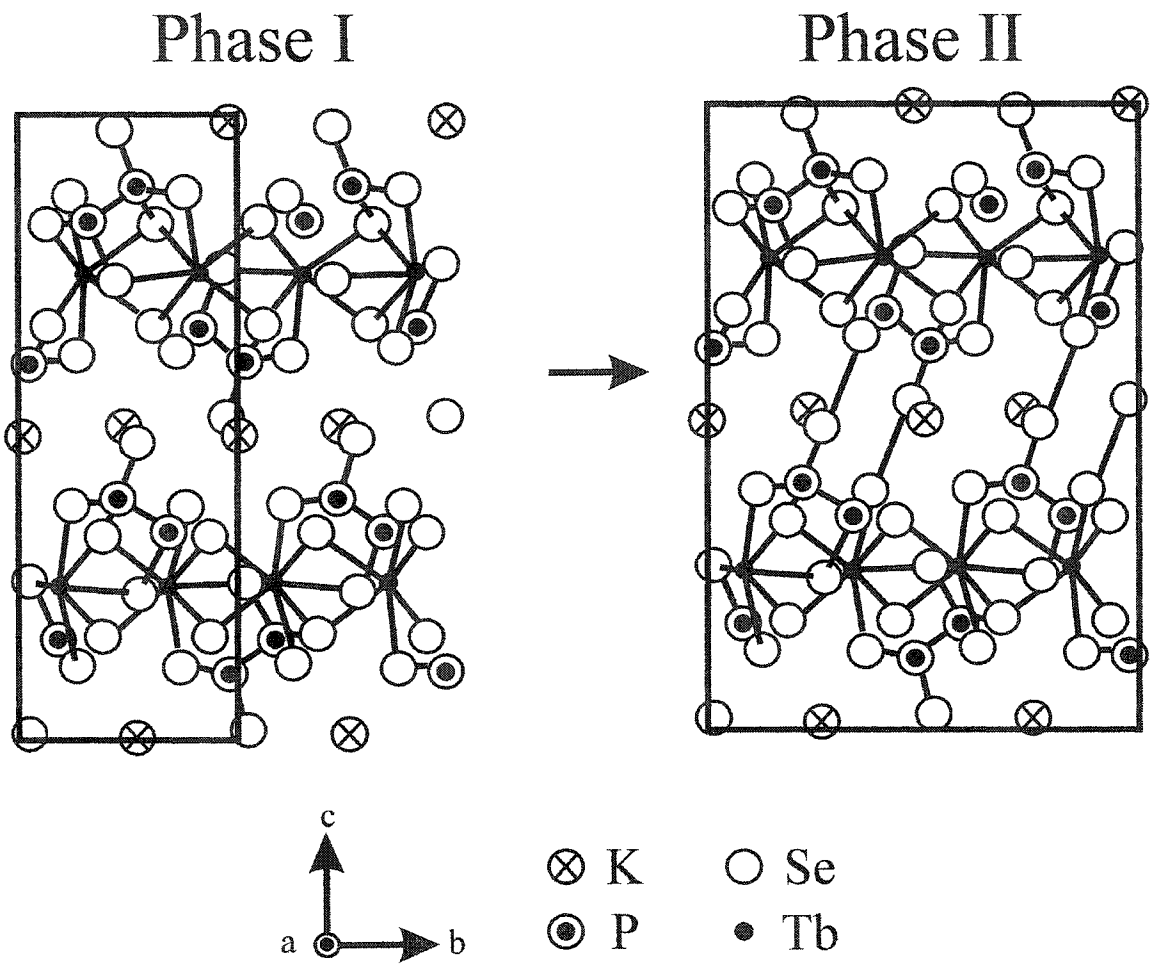

Figure 8.1: Structure of Phase I and II of $KTbP_2Se_6$ [10].

8.1.1.2 Phase Transitions [10]

Visual observations of the phase transition are reported by Orgzall et al. A phase line can be seen moving through the crystal as the light yellow color of the crystal in phase I changes to the dark red color of phase II. The complete transition takes from 5 to 10 seconds for a crystal of about 100 μm. A decrease in both pressure and volume is observed and is the probable reason for the slight hysteresis of 4 kbar also observed at the phase transition.

8.1.1.3 Electronic Properties at Room Temperature

A $4f$-$5d$ charge transfer model has been proposed to explain the color change observed at the phase transition. The color change is due to a $4f$-$5d$ charge transfer from the selenium to the phosphorus accompanied by the formation of a Se-Se bond [10]. This charge transfer mechanism is in contrast to that for $KTb(MoO_4)_2$ in which the color change is due to a $4f$-$5d$ charge transfer in Tb ($Tb^{3+}Mo^{6+} \rightarrow Tb^{4+}Mo^{5+}$) [97]. The equivalent charge mechanism in $KTbP_2Se_6$ would occur by way of a charge transfer in terbium ($Tb^{3+}P^{4+} \rightarrow Tb^{4+}P^{3+}$), but this is not the case. Luminescence studies of $KTbP_2Se_6$ clearly indicate the terbium atom remains in the +3 oxidation state at high pressures as opposed to the luminescence studies of $KTb(MoO_4)_2$ which show a change in the oxidation state of Tb at high pressures[11, 12].

8.1.1.4 Vibrational Properties at Room Temperature

Room temperature Raman studies of $KTbP_2Se_6$ reveal a large number of Raman active modes due to the low symmetry of the crystal and large number of atoms in the unit cell. Below 160 cm^{-1} the peaks are strongly overlapping as can be seen in Figure 8.2. With increasing pressure some of these modes begin to separate and some other modes cross one

another. Several modes exist at higher frequencies as well and, with increasing pressure, even more modes appear due to the doubling of the unit cell at the phase transition.

The strong ambient pressure mode at 225 cm^{-1} is of particular interest as it supports the occurrence of the Se-Se bond at the phase transition. This is the P-P stretch mode and decreases in frequency as the phase transition. Concurrently a new mode appears at a slightly smaller frequency. This new mode is associated with the bonding of selenium atoms across the decrease in frequency of the P-P mode represents the weakening of that bond due to the charge transfer from the Se to the P. reddish

8.2 Room Temperature Raman Measurements

High-pressure Raman scattering measurements performed at room temperature have been reported by Orgzall et al. [10]. New room temperature Raman measurements are reported in this thesis for comparison to previously published data. Data reported by Orgzall was taken with a triple spectrometer allowing for better resolution than measurements reported herein. A comparison of these data can be seen in Figure 8.2.

8.3 Low Temperature Measurements

No low temperature measurements have been reported in the literature. In order to determine the phase transitions at low temperature, high-pressure Raman measurements were performed.

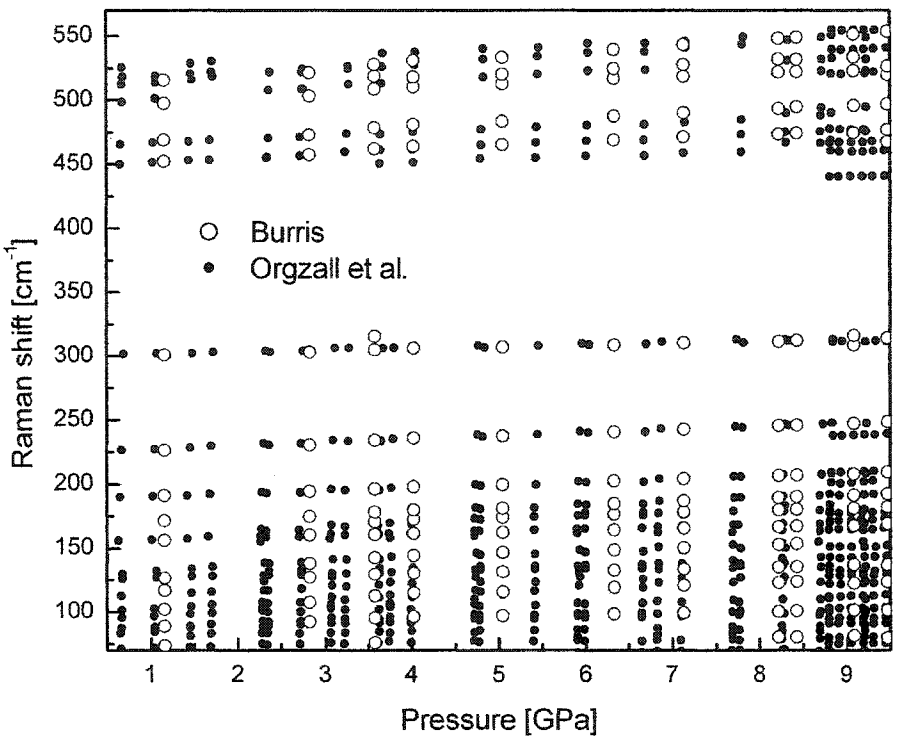

Figure 8.2: New and previously published [10] room temperature Raman measurements of $KTbP_2Se_6$.

8.3.1 Experimental Details

Single reddish-brown crystals of the $KTbP_2Se_6$ were prepared by the Dorhout inorganic chemistry group at Colorado State University. The crystals were prepared by reacting terbium, elemental phosphorus, selenium metal, and K_2Se_4 together [100]. High-pressure optical and energy dispersive x-ray diffraction measurements were performed as described in Chapter 4. As detailed in Chapter 2, argon or a methanol ethanol mixture was used as the pressure transmitting medium for optical measurements while ruby was the pressure sensor. NaCl was used as both the pressure transmitting medium and the pressure sensor for x-ray measurements. The low temperature apparatus is described in appendix B.

8.3.2 Raman

Raman measurements at 77 K show the occurrence of a phase transition at 7.6 GPa as can be seen in Figure 8.3.

8.4 Discussion

Low temperature Raman measurements were performed on $KTbP_2Se_6$. These measurements reveal a phase transitions at 7.6 GPa. Low temperature absorption measurements would also be of interest for this material and will be possible with perfection of the absorption system as described in Chapter 4.

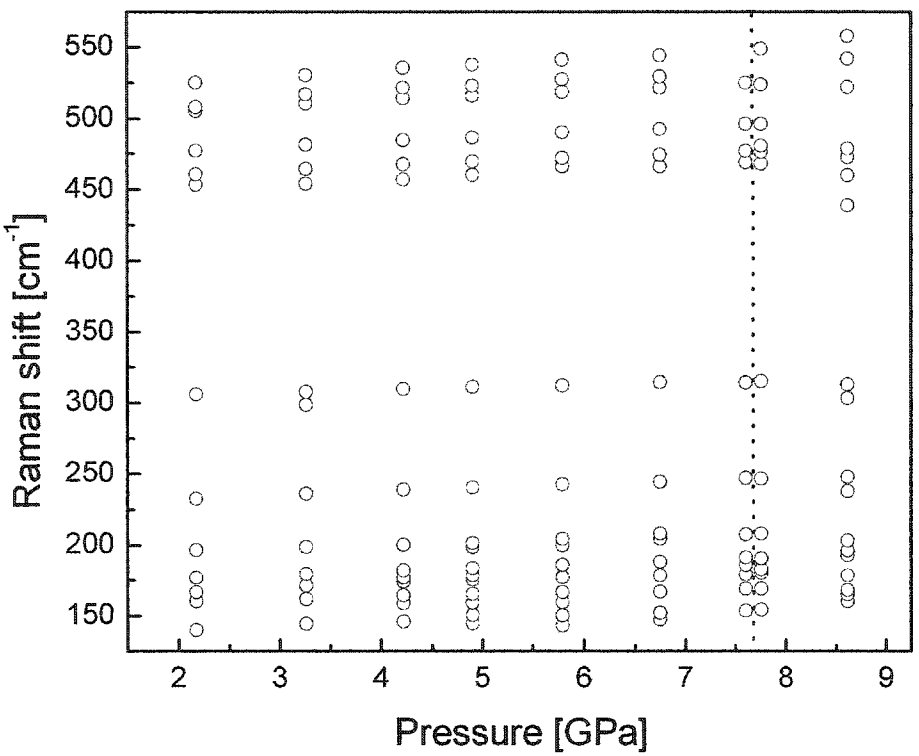

Figure 8.3: Raman measurements of $KTbP_2Se_6$ at 77 K.

Chapter 9

Summary

This thesis has detailed the experiments performed on three seperate materials $(NH_4)_2ZnCl_4$, Cs_2MoS_4, and $KTbP_2Se_6$ as well as the design of an absorption system capable of performing high-pressure, low-temperature measurements in a diamond anvil cell and modification of the diamond anvil cell for use at low-temperatures.

Materials

Energy dispersive x-ray diffraction was used to probe the change in volume with increasing pressure at constant temperatures. The isothermal equation of state of $(NH_4)_2\,ZnCl_4$ was ascertained and the lattice parameters and bulk modulus of the material were determined. Optical properties of Cs_2MoS_4 were investigated under high-pressure and low-temperature. Two phase transitions at 8.1 GPa and 9.1 GPa are reported. Low-temperature, high-pressure studies of $KTbP_2Se_6$ reveal a phase transition at 7.6 GPa.

Apparatus

An optical system was designed to focus an absorption lamp down to 20 μm, required for the small volume of the diamond anvil cell. The ability to focus this spot, along with the size and distance constraints of the system are the key characteristics of the arrangement. In particular, the small diameter of the optical window of the cryostat had to be taken into account in order to assure success. Taking into account all requirements produced the need for a three lens plus two pinhole optical system. Detailed calculations were performed to determine the optimal arrangement for the system.

The diamond anvil cell was modified in order to allow for added stabilization when used in low-temperature measurements. At ambient temperatures, the original diamond anvil cell is easily monitored to ensure even force application and experiments were all successful. When the original diamond anvil cell was placed in the cryostat, the higher experimental pressures were regularly unattainable due to the inability to closely monitor the force application to the diamond anvil cell. The diamond anvil cell was modified to include extra support to prevent uneven force application to the diamond anvil cell and a new gasket was designed to help attain the higher pressures necessary for the desired experiments.

Appendix A

Absorption System Calculations

As mentioned in Chapter 4, a multi-lens system was designed to facilitate high-pressure, low-temperature optical absorption measurements. The goal was to project a focused spot of light onto a sample in a diamond anvil cell positioned in a cryostat. Several calculations were necessary to determine the lenses and distances needed to achieve this goal. Possible configurations of the system are limited by several factors.

One group of restrictions placed on the system originates from the design of the high-pressure and low-temperature apparatus. First, the size of the sample in the diamond anvil cell is such that the light used to illuminate the sample must be projected to a very small spot size (~15 μm). In order to have space for the cryostat there must be a minimum distance of 35 cm between the final focusing lens and the sample. Third, the optical window of the cryostat measures 0.8 cm in diameter and the cone of light projected from the final system lens to the sample must clear this window.

Other constraints include the following. Lens diameters must be large enough to capture all of the projected light. Lens diameters and focal lengths must be available for purchase. Also, there is a limited space of 90 cm in which to set up the system.

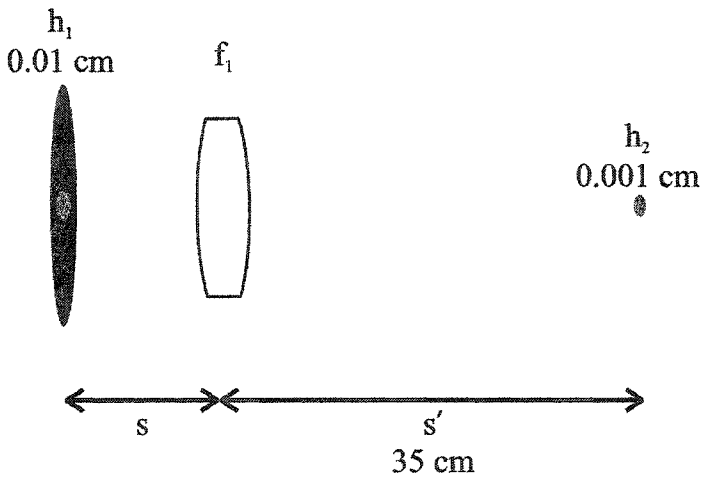

Figure A.1: One lens system.

The final major consideration involves the competing goals of a crisp focused 15 μm spot with a reasonable intensity at the sample. In order to image the spot at the sample, a pinhole was placed in front of the light source. The light at the sample is thus a projection of this pinhole. The size of the pinhole was chosen to achieve both adequate intensity at the sample and to allow for the appropriate decrease in image size within the space available for the optical system. A 100μm pinhole was found to be a reasonable compromise between these competing constraints.

A.1 Single Lens

The simplest experiment is one in which the smallest number of lenses is used to project the pinhole onto the sample. Figure A.1 shows a single lens absorption system. The thin lens equations for the system are

$$\frac{1}{f_1} = \frac{1}{s} + \frac{1}{s'} \tag{A.1}$$

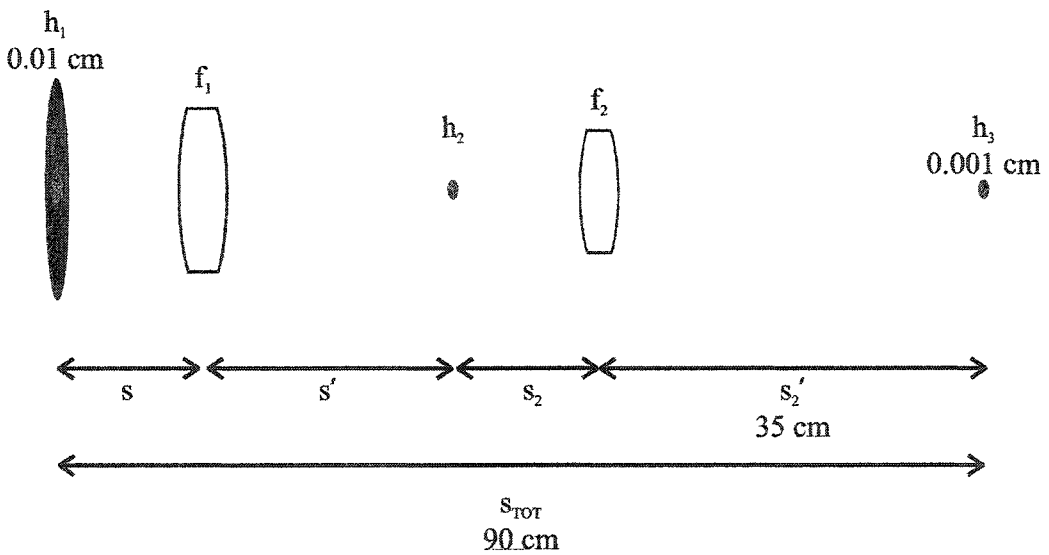

Figure A.2: Two lens system.

and

$$\frac{h_1}{s} = \frac{h_2}{s'} \tag{A.2}$$

where f_1 is the focal length of the lens, s and s' are defined in Figure A.1, h_1 is the height of the pinhole and h_2 is the height of the projection onto the sample.

As discussed in the previous paragraphs, the known variables of the system are $s' = 35$ cm, $h_1 = 0.01$ cm, and $h_2 = 0.001$ cm. By solving equations A.1 and A.2, values of 350 cm and 31.82 cm are determined for the unknown variables s and f_1 respectively. The value of 350 cm for s gives an unreasonable total distance of 385 cm for all components. This is far greater than the space available and thus a one lens system is impossible.

A.2 Two Lenses

A two lens system is shown schematically in Figure A.2. The four available lens equations are equations A.1 and A.2 along with

$$\frac{1}{f_2} = \frac{1}{s_2} + \frac{1}{s_2'} \tag{A.3}$$

and

$$\frac{h_2}{s_2} = \frac{h_3}{s_2'} \tag{A.4}$$

The known variables of the system are $s_2' = 35$ cm, $h_1 = 0.01$ cm, and $h_3 = 0.001$ cm. The unknown variables are s, s', s_2, f_1, f_2, and h_2. All variables are labeled in Figure A.2. This gives a system of four equations with six unknowns. Two of the variables must be set in order to calculate the other variables. By fixing the total distance to be

$$s_{TOT} = s + s' + s_2 + s_2' = 90\,\text{cm} \tag{A.5}$$

the system is simplified to five equations with six unknowns. By choosing a reasonable value for f_1 the system of equations is solvable.

The next criteria that must be met is that of reasonable lens diameters. Some minimum lens diameter exists which will allow for all the light to be collected from the pinhole and projected onto the sample. Using the system shown in Figure A.3 we can define the minimum lens diameters, d_1 and d_2 of the two lenses. These diameters can be determined by knowing the height of the light source, measured to be 0.1 cm, and by fixing the distance from the pinhole to the light source, s_F. By following the ray diagram in Figure A.3 it can

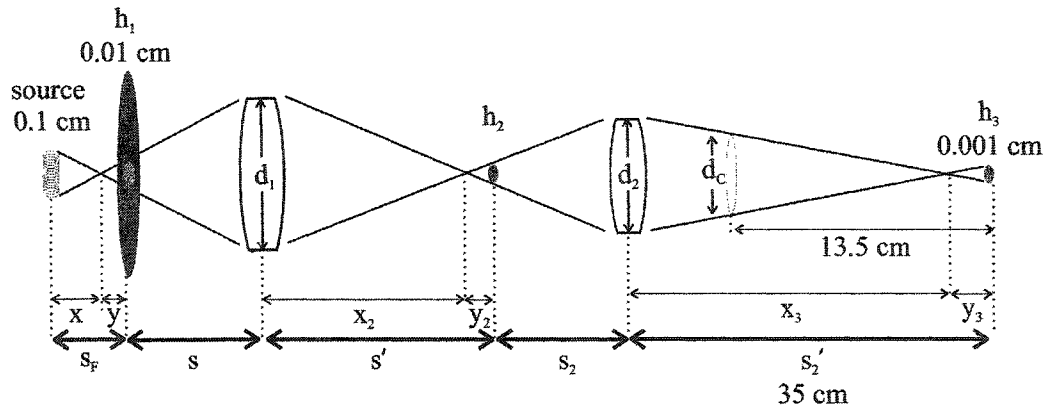

Figure A.3: Diagram of two lens system for lens diameter determination.

be seen that

$$d_1 = \frac{0.1\,(s + s_F)}{x} - 0.1 \tag{A.6}$$

where $x = s_F\,(h_1/0.1\,\mathrm{cm} + 1)^{-1}$ and

$$d_2 = \frac{d_1\,(s_2 + s')}{x_2} - d_1 \tag{A.7}$$

where $x_2 = s'\,(h_2/d_1 + 1)^{-1}$. There exist several reasonable values of d_1 and d_2 corresponding to some of the values of f_1 determined previously.

A final criteria must be met for the system. As mentioned in the previous section the optical window of the cryostat is 0.8 cm. It must be determined if the calculated values of d_1 and d_2 are such that all the projected light passes through the 0.8 cm optical window. The distance from the optical window to the sample is measured to be 13.5 cm. Using this fact, and referring back to the system shown in Figure A.3, it can be shown that the

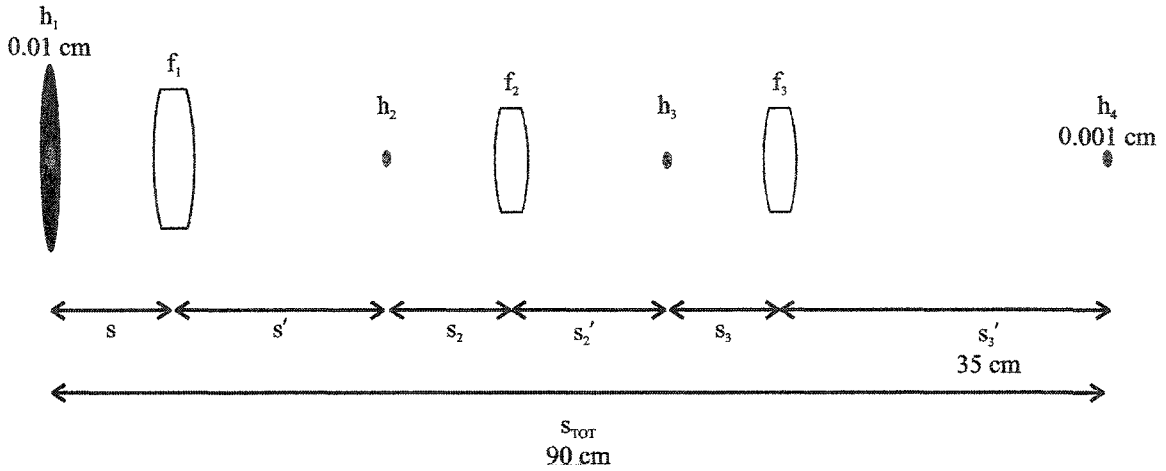

Figure A.4: Three lens system.

diameter of cryostat's optical window, d_c, must be larger than

$$d_c = h_3 \left(\frac{13.5\,\text{cm}}{x_3} - 1 \right)$$

where $x_4 = s_2' \left(d_2/h_3 + 1 \right)^{-1}$. Unfortunately the calculated values for d_c that correspond to the aforementioned reasonable values of f_1, d_1, and d_2 are all greater than 0.8 cm. The two lens system is thus impossible.

A.3 Three Lenses

Figure A.4 shows a three lens system. The six available lens equations are equations A.1, A.2, A.3, and A.4 along with

$$\frac{1}{f_3} = \frac{1}{s_3} + \frac{1}{s_3'} \tag{A.8}$$

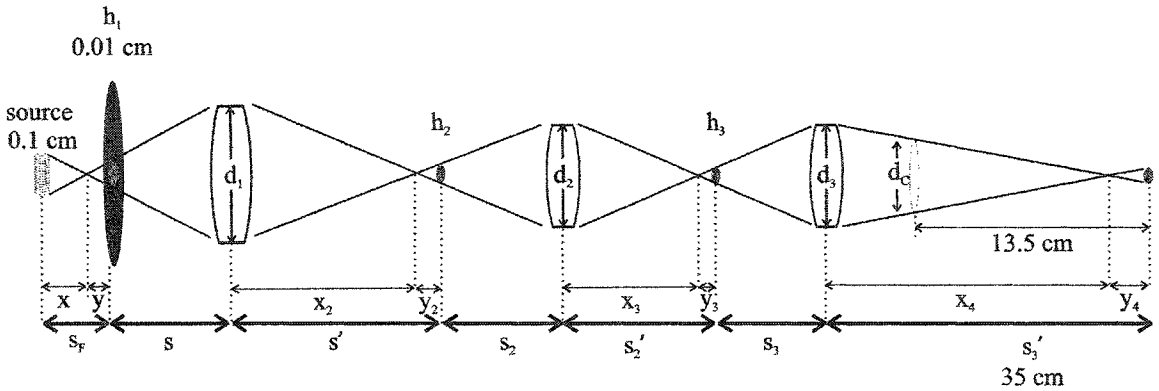

Figure A.5: Diagram of three lens system for lens diameter determination.

and

$$\frac{h_3}{s_3} = \frac{h_4}{s_3'} \tag{A.9}$$

The known variables of the system are $s_3' = 35$ cm, $h_1 = 0.01$ cm, and $h_4 = 0.001$ cm. The unknown variables are s, s', s_2, s_2', s_3, f_1, f_2, f_3, h_2 and h_3. This gives a system of six equations with ten unknowns. Four of the variables must be fixed. By fixing the total distance to be 90 cm, as in equation A.5, the system is simplified to seven equations with ten unknowns. By choosing reasonable values for f_1, f_2, and f_3, the system of equations is solvable. Several reasonable values of f_1, f_2, and f_3 are solutions to this system.

As with the two lens system it must be determined if reasonable lens diameters exist for the system described in the previous paragraph. Using the system shown in Figure A.5, we can define the minimum lens diameters (d_1, d_2 and d_3) of the three lenses. The values of d_1 and d_2 are determined from equations A.6 and A.7 respectively. It can be shown that

$$d_3 = \frac{d_2\,(s_3 + s_2')}{x_3} - d_2$$

where $x_3 = s_2'\,(h_3/d_2 + 1)^{-1}$. There exist several reasonable values of d_1, d_2 and d_3 for

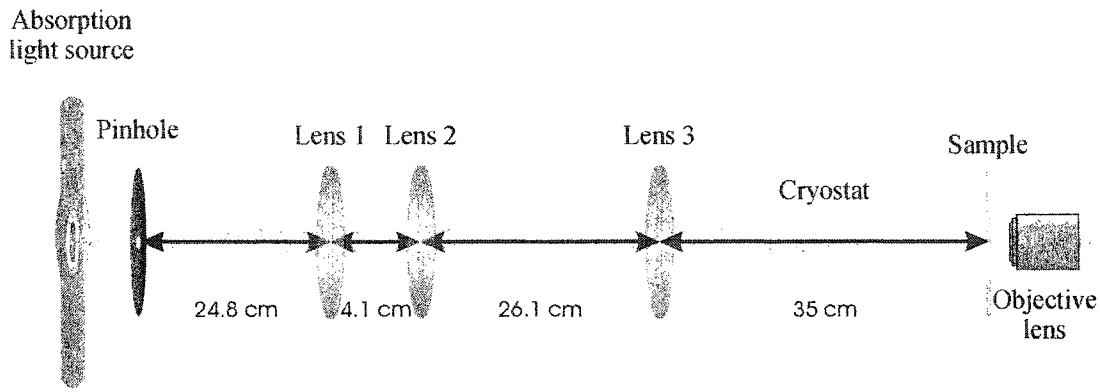

Figure A.6: Absorption system labeled with distances between optical components.

the system described in the previous paragraph.

As with the two lens system, it must be determined if the calculated values d_1, d_2 and d_3 are such that all the projected light passes through the 0.8 cm optical window. Referring back to the system shown in Figure A.5, it can be shown that the diameter of the cryostat's optical window, d_c, must be larger than

$$d_c = h_4 \left(\frac{13.5\,\text{cm}}{x_4} - 1 \right)$$

where $x_4 = s_3' \left(d_3/h_4 + 1 \right)^{-1}$. Fortunately there exists a solution to the three lens calculation which gives a value of $d_c < 0.8$ cm. The three lens system is possible.

A.4 Experimental Setup

The actual experimental system is shown in Figure A.6. Three lenses were chosen with focal lengths $f_1 = 1.4$ cm, $f_2 = 1.6$ cm, and $f_3 = 13.5$ cm. These choices, together with the known variables of the system ($s_3' = 35$ cm, $h_1 = 0.01$ cm, $h_4 = 0.001$ cm,

and $s_{TOT} = 90$ cm), allow for the determination of the following variables: $s = 24.8$ cm, $s' = 1.5$ cm, s_2 =2.6 cm, $s_2' = 4.1$ cm, $s_3 = 22$ cm, $h_2 = 6 \times 10^{-4}$ cm, and $h_3 = 9 \times 10^{-4}$ cm. All lenses have an appropriate diameter as discussed in the previous section and the optical window of the cryostat fits well in the system.

Appendix B

Variable-Temperature Equipment

For high-pressure measurements taken at non-ambient temperatures, special equipment must be designed to facilitate the cooling or heating of the sample. The design must allow not only for temperature variation but also for access to the diamond anvil cell.

B.1 High-Temperature Apparatus

A device used to perform high-pressure measurements at moderately high temperatures (up to 150^{o}C) is shown in Figure B.1. This device was specifically designed for use in x-ray diffraction experiments but could be easily altered for optical experiments. The temperature is regulated by a model CN 76000 temperature controller from Omega Engineering Corporation. The temperature is controlled to within $\leq 0.5^{o}$C

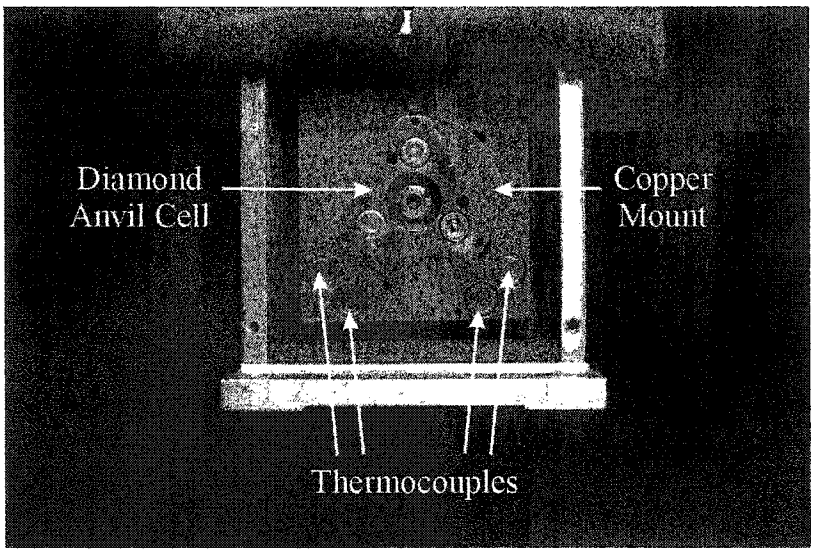

Figure B.1: DAC Heater.

B.2 Low-Temperature Apparatus

The cryostat used for low-temperature, high-pressure optical measurements was built by CRYO Industries of America, Incorporated. A model RC102 continuous flow cryostat was modified to hold a diamond anvil cell (DAC) and to allow for pressure adjustment during a temperature run.

B.2.1 Cryostat

A schematic of the cryostat is shown in Figure B.2 and a external picture is shown in Figure B.3. Key features of the cryostat include two optical windows at opposite sides of the cryostat, DAC mount, and tightening rods for the DAC. The main modification made to the original, model RC102, CRYO Industries cryostat allows for outside access to the three force application screws of the DAC via the three tightening rods. This modification is essential to perform high-pressure, low-temperature experiments in a reasonable time

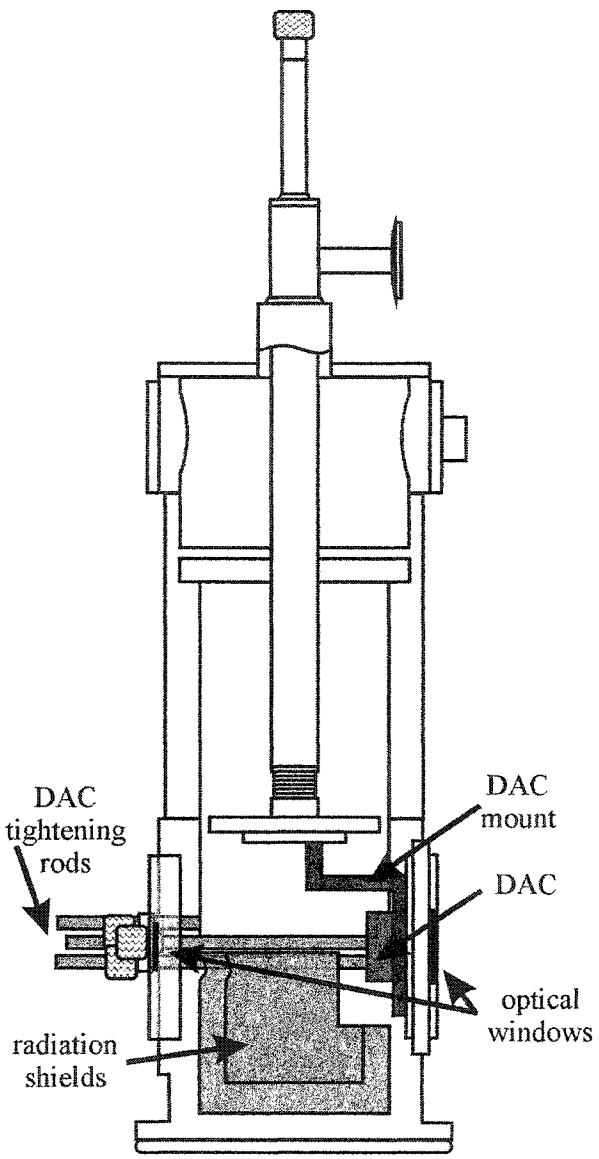

Figure B.2: Schematic of Cryostat.

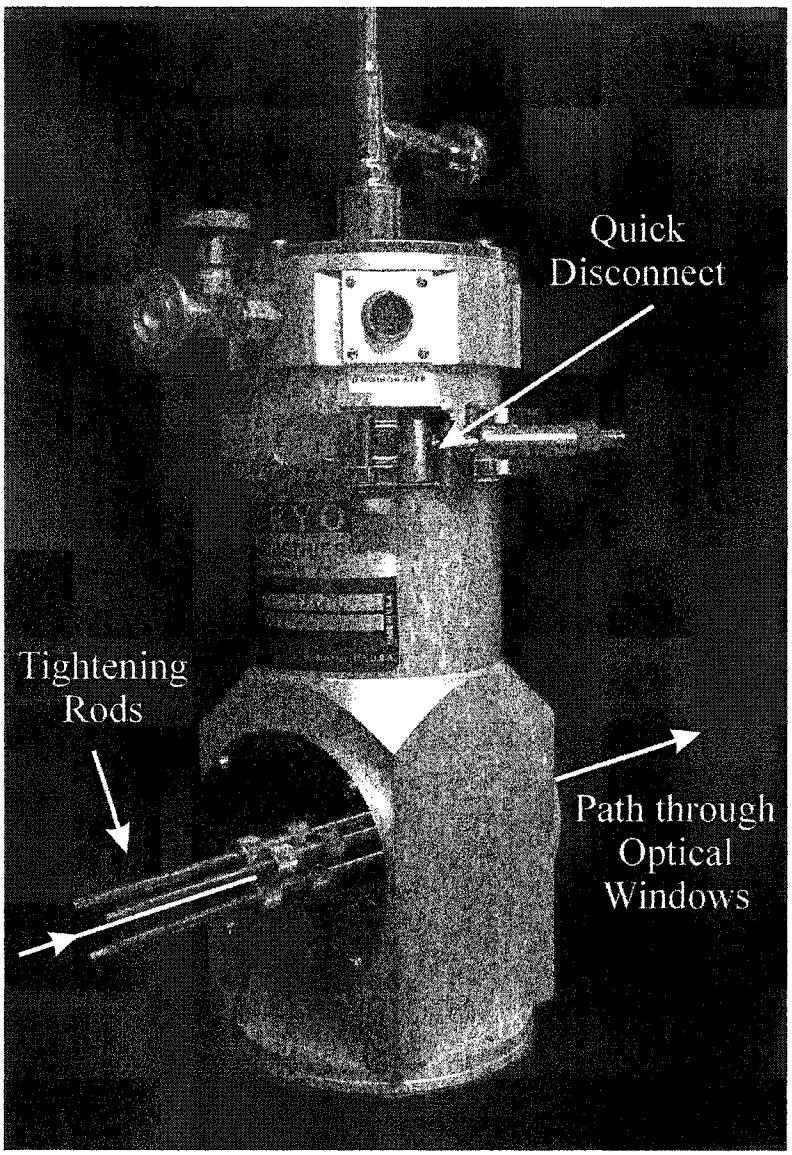

Figure B.3: Cryostat.

period. Without this adaptation the cryostat would have to be brought to room temperature and then cooled down again for every pressure increase. This would cause an increase in experiment time from about 20 minutes for a data point to about three hours. Another, more simple modification was the addition of a mount for the DAC.

The model RC102 cryostat was designed to allow quick access through the top of the cryostat. With the modifications mentioned above this access is no longer possible. Instead, the DAC must be placed into the cryostat from the bottom. In order to access the DAC mount, the bottom plate of the cryostat and the two radiation shields must be removed. Care must be taken to position the DAC into the mount so that it is as close to the edge of the cryostat as possible without actually touching the edge. If the DAC is too far from the edge of the cryostat the 1.4 cm focal length objective lens used in the system will not be able to focus on the sample. If the DAC is touching the edge of the cryostat, conduction between the DAC and the cryostat will occur causing temperature stabilization problems and will also cause the optical window to ice up. These two requirements restrict the position of the DAC to within ~1 mm. Before cooling down can proceed, the cryostat must be evacuated overnight to about 10^{-5} Torr. The temperature is regulated by a model LTC-11 temperature controller from Neocera. The temperature is stable to within $\leq 0.5^{o}$C.

B.3 Future

One of the desirable features of the model RC102 cryostat is a quick disconnect for easy sample access. This feature allows for the sample to be removed from the top of the cryostat avoiding the bottom loading procedure mentioned in the previous section. The sample holder for the diamond anvil cell is shaped such that the quick disconnect is no longer functional. With slight modification of this sample holder, the quick disconnect will again

be functional and much time will be saved in the entire process of placing the diamond anvil cell into the cryostat.

Measurements at helium temperatures are also possible with this cryostat. Unlike liquid nitrogen, liquid helium requires constant shielding from outside temperatures in order maintain a liquid state. A transfer line must therefore be used to achieve a continuous flow of liquid helium from the storage dewar to the cryostat. Since movement of greater than 20 μm can result in significant error for diamond anvil cell experiments, a system must be designed to better isolate the cryostat from unwanted motion when this transfer line is used.

Bibliography

[1] H. Poulet and R. Pick, J. Phys. C **14**, 2675 (1981).

[2] R. R. Chianelli, Catal. Rev.-Sci. Eng. **26**, 361 (1984).

[3] D. Coucouvanis, Acc. Chem. Res. **14**, 201 (1981).

[4] T. Suzuki, Physica B **188**, 347 (1993).

[5] P. N. Kumta and S. H. Risbud, J. Mater. Sci. **29**, 1135 (1994).

[6] P. N. Kumta and S. H. Risbud, Am. Ceram. Soc. Bull. **69**, 1977 (1990).

[7] R. Mauricot, J. DexpertGhys, and M. Evain, J. Luminesc. **69**, 41 (1996).

[8] B. Lorenz, I. Orgzall, P. Dorhout, C. Raymond, and H. Hochheimer, Sol. Stat. Comm. **97**, 535 (1996).

[9] B. Lorenz et al., Phys. Rev. B **55**, 2800 (1997).

[10] I. Orgzall et al., J. Phys. Chem. Solids **61**, 123 (2000).

[11] J. Burris, I. Orgzall, C. Evenson, P. Dorhout, and H. Hochheimer, J. Phys. Chem. Solids **63**, 597 (2002).

[12] H. Hochheimer, J. Burris, I. Orgzall, C. Evenson, and P. Dorhout, High Pressure Res **22**, 237 (2002).

[13] R. M. Hazen, *The Diamond Makers*, Cambridge University Press, New York, 1999.

[14] J. Jamieson, A. Lawson, and N. Nachtrieb, Rev. Sci. Instrum. **30**, 1016 (1959).

[15] C. E. Weir, E. R. Lippincott, A. V. Valkenburg, and E. N. Bunting, J. Res. Natl. Bur. Stand. **63A**, 55 (1959).

[16] J. Xu, H. Mao, and P. Bell, Science **232**, 1404 (1986).

[17] R. Hemley, M. Eremets, and H. Mao, Progress in experimental studies of insulator-metal transitions at multimegabar pressures, in *Frontiers of High Pressure Research II: Applications of High Pressure to Low-Dimensional Novel Electronic Materials*, edited by P. D. H.D. Hochheimer, B. Kuchta and J. Yarger, volume 48 of *NATO Science Series II Mathematics, Physics and Chemistry*, pages 201–216, Kluwer Academic Publishers, 2001.

[18] E. Choi, H. Kang, Y. Jo, and W. Kang, Rev. Sci. Instrum. **73**, 2999 (2002).

[19] A. Eichler and W. Gey, Rev. Sci. Instrum. **50**, 1445 (1979).

[20] L. Merrill and W. Bassett, Rev. Sci. Instrum. **45**, 290 (1974).

[21] D. Dunstan, Experimental techniques in the diamond anvil-cell, in *High Pressure Molecular Science*, edited by R. Winter and J. Jonas, volume 358 of *NATO Science Series E: Applied Sciences*, pages 87–101, Kluwer Academic Publishers, 1998.

[22] S. Block and G. Piermarini, Phys. Today **29**, 44 (1976).

[23] A. V. Valkenburg, Rev. Sci. Instrum. **33**, 1462 (1962).

[24] D. Dunstan, Rev. Sci. Instrum. **60**, 3789 (1989).

[25] A. Jayaraman, Rev. Mod. Phys. **55**, 65 (1983).

[26] P. Bell and H. Mao, Carnegie Institute Yearbook **80**, 404 (1981).

[27] G. Piermarini, S. Block, and J. Barnett, J. Appl. Phys. **44**, 5377 (1973).

[28] W. Sherman and A. Stadtmuller, *Experimental Techniques in High-Pressure Research*, John Wiley and Sons Ltd., 1987.

[29] D. Decker, J. Appl. Phys. **36**, 157 (1965).

[30] D. Decker, J. Appl. Phys. **37**, 5012 (1966).

[31] L. Ming et al., J. Appl. Phys. **54**, 4390 (1983).

[32] R. Forman, G. Piermarini, J. Barnett, and S. Block, Science **176**, 284 (1972).

[33] G. Piermarini, S. Block, J. Barnett, and R. Forman, J. Appl. Phys. **46**, 2774 (1975).

[34] H. Mao, P. Bell, J. Shaner, and D. Steinberg, J. Appl. Phys. **49**, 3276 (1978).

[35] D. Ragan, R. Gustavsen, and D. Schiferl, J. Appl. Phys. **72**, 5539 (1992).

[36] B. Lorenz, Y. Shen, and W. Holzapfel, High Press. Res. **12**, 91 (1994).

[37] H. Arashi and M. Ishigame, Japanese J. Appl. Phys. **22**, 1647 (1982).

[38] Y. Zhao et al., J. Appl. Phys. **84**, 4049 (1998).

[39] J. Xu and H. Mao, Science **290**, 783 (2000).

[40] J. Yarger, Personal communication, Gratitude is due Jeff Yarger at the University of Wyoming for many enlightening discussions.

[41] ThermoGalactic Industries Corp., *GRAMS/32 Version 4.11 and GRAMS/AI Version 7.00*, 1991 and 2001.

[42] S. McGlynn, T. Azumi, and M. Kinoshita, *Molecular spectroscopy of the triplet state*, Prentice-Hall Inc., Englewood N.J., 1969.

[43] B. J. Berne and R. Pecora, *Dynamic Light Scattering with Applications to Chemistry, Biology and Physics*, Dover Publications, Inc., 2000.

[44] J. R. Ferraro, K. Nakamoto, and C. W. Brown, *Introductory Raman Spectroscopy*, Academic Press, second edition, 2003.

[45] N. Ashcroft and N. D. Mermin, *Solid State Physics*, Saunders College Publishing, 1976.

[46] E. Wilson, J. Decius, and P. Cross, *Molecular Vibrations: The theory of Infrared and Raman Vibrational Apectra*, McGraw-Hill Book Company, Inc., 1955.

[47] U. Sakalle, P. Jha, and S. Sanyal, Bull. Mater. Sci. **23**, 233 (2000).

[48] D. A. Long, *The Raman Effect: A unified treatment of the theory of Raman scattering by molecules*, John Wiley and Sons, Inc., 2002.

[49] B. Dippel, Energy level diagram, http://www.raman.de.

[50] X-ray data booklet, Center for X-ray Optics and Advanced Light Source, Lawrence Berkeley National Laboratory, 2001.

[51] W. L. Bragg and W. H. Bragg, *X-rays and Crystal Structure*, G. Bell, 1st edition, 1915.

[52] L. Meitner, J. Zeitschrift fur Physik (1923), Reference from http://www.wikipedia.org.

[53] Australian synchrotron research program, http://www.ansto.gov.au.

[54] Cornell high energy synchrotron source (chess), http://www.CHESS.cornell.edu.

[55] H. Wiedemann, *Synchrotron Radiation*, Springer, 2003.

[56] M. Evain, *U-FIT: A cell parameter refinement program*, I.M.N., Nantes, France, 1992.

[57] H. Cummins, Phys. Rep. **185**, 211 (1990).

[58] G. Smolensky, I. Siny, S. Prokhorova, E. Kuzminov, and V. Mikvabia, Ferroelectrics **36**, 351 (1981).

[59] H. Matsunaga and E. Nakamura, J. Phys. Soc. Japan **50**, 2789 (1981).

[60] T. Sato, T. Osaka, and Y. Makita, J. Phys. Soc. Japan **53**, 1907 (1984).

[61] H. Matsunaga, Phys. Soc. Japan **51**, 864 (1982).

[62] I. Belobrova, A. Moskalev, N. Bizukina, S. Milul, and I. Alexsandrova, Solid State Commun. **33**, 1101 (1980).

[63] D. Kucharczyk, J. Warczewski, and H. Broda, Acta Cryst **A37**, C (1981).

[64] H. V. Konigsveld, Acta Cryst. C **39**, 15 (1983).

[65] I. Mikhail, Acta Cryst. **B36**, 2126 (1980).

[66] A. Kityk, Phys. Stat. Sol. (b) **181**, 345 (1994).

[67] A. Gillet, Y. Luspin, and G. Hauret, Solid State Commun. **64**, 797 (1987).

[68] Y. Luspin and G. Hauret, Solid State Commun. **69**, 1187 (1989).

[69] J. Burris et al., J. Phys. Chem. Solids **61**, 719 (2000).

[70] F. Murnaghan, Proc. Natl. Acad. Sci. USA **30**, 244 (1944).

[71] Microcal Software, Inc., *ORIGIN*, 6.0 edition.

[72] S. S. Corporation, Un-scan-it, Data extrapolation software.

[73] C. Whitfield and E. Brody, Rev. Sci. Instrum. **47**, 942 (1976).

[74] J. Horikx, A. Arts, J. Dijkhuis, and H. de Wijn, Phys. Rev. B **39**, 5726 (1989).

[75] Y. Luspin, M. Chabin, G. Hauret, and F. Gilletta, J. Phys. C: Solid State Phys. **15**, 1581 (1982).

[76] K. Alexandrov et al., Sov. Phys. Crystallogr. **21**, 296 (1976).

[77] K. Weishaupt, J. T. Held, and H. Hochheimer, Taken from unpublished data.

[78] K. Weishaupt, J. T. Held, S. Kohn, A. Onodera, and H. Hochheimer, J. Phys. Chem. Solids **58**, 1603 (1997).

[79] C. Raymond, P. Dorhout, and S. Miller, Z. Krist. **210**, 775 (1995).

[80] R. Gordon, D. Yang, E. Crozier, D. Jiang, and R. Frindt, Phys. Rev. B **65**, 125407 (2002).

[81] A. Müller and E. Diemann, Adv. Inorg. Chem. **31**, 89 (1987).

[82] A. Müller et al., Monatsh. Chem. **116**, 711 (1985).

[83] A. Müller, R. Jostes, and F. A. Cotton, Angew. Chem., Int. Ed. Engl. **19**, 875 (1980).

[84] A. Müller, S. Sarkar, R. Bhattacharyya, S. Pohl, and M. Dartmann, Angew. Chem., Int. Ed. Engl. **17**, 535 (1978).

[85] A. Müller, Polyhedron **5**, 323 (1986).

[86] A. Müller et al., Appl. Catal. **62**, L13 (1990).

[87] A. Müller, W. O. Nolte, and B. Krebs, Angew. Chem. **90**, 286 (1978).

[88] V. P. Fedin et al., Inorg. Chim. Acta **223**, 5 (1994).

[89] B. Wolf, J. Molter, G. Bruls, B. Lüthi, and L. Jansen, Phys. Rev. B **54**, 348 (1996).

[90] J. Wilson and A. Yoffe, Adv. Phys. **18**, 193 (1969).

[91] D. Shriver, P. Atkins, and C. Langford, *Inorganic Chemistry*, W.H. Freeman and Company, New York, second edition, 1994.

[92] A. Jayaraman, S. Wang, S. Shieh, S. Sharma, and L. Ming, J. Raman Spectr. **26**, 451 (1995).

[93] D. Christofilos, G. A. Kourouklis, and S. Ves, J. Phys. Chem. Solids **56**, 1125 (1995).

[94] A. Jayaraman, S. Y. Wang, and S. K. Sharma, Phys. Rev. B **52**, 9886 (1995).

[95] A. Jayaraman et al., J. Phys. Chem. Solids **54**, 827 (1993).

[96] A. Jayaraman, S. K. Sharma, and S. Y. Wang, Pramana - J. Phys. **40**, 357 (1993).

[97] A. Jayaraman, S. Y. Wang, S. K. Sharma, and S.-W. Cheong, Curr. Sci. **7**, 232 (1996).

[98] M. Robinson, J. Phys. Chem. **62**, 925 (1958).

[99] I. Kawada, K. Kato, and T. Fujita, Acta Crystallogr. B **30**, 2069 (1974).

[100] J. Chen, P. Dorhout, and J. Ostenson, Inorg. Chem. **35**, 5627 (1996).

[101] C. Thiel, Y. Sun, and R. Cone, J. Mod. Optics **49**, 2399 (2002).